Development Of A Turbulent Iron Burner For Use As A Clean Energy Carrier

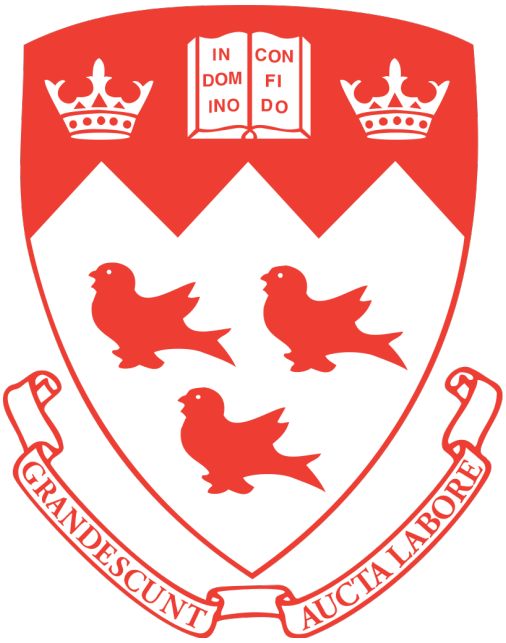

Samson Bowen-Bronet

Department of Mechanical Engineering

McGill University

Montreal, Quebec

November 4, 2021

This thesis is submitted to McGill University in partial fulfillment of the requirements for the degree of Master of Engineering

Abstract

With the growing energy and climate crisis there is a clear need to shift towards clean renewable energies like solar, wind and hydro. However, a major problem with these intermittent sources is how to store excess energy for periods of high demand or low production (e.g. at night, on cloudy days, etc.). A second issue is how to transport the energy generated to regions that need it across the globe. Metals such as iron and aluminum have been proposed as potential carbon free energy carriers that could fill this role since they have similar energy densities to traditional hydrocarbon fuels, are abundant in the earth's crust and are safe to transport and store. A first step towards this goal is made with the design and fabrication of a turbulent iron burner. The design draws upon previous work in metal combustion as well as the turbulent combustion of solids in pulverised coal burners. Extensive testing of the burner yielded the first ever self-sustained pure iron flame; stabilizing flames for long durations of over twenty minutes. The burner operated at the lab scale with a thermal power of roughly 10 kW and a cyclonic collection system is connected to the outlet of the flame to capture the burnt iron oxide particles. The stability of the iron flame and the effectiveness of the cyclonic collection system permitted several experiments and diagnostics to be performed. Heat extraction experiments demonstrated the potential of iron flames to generate power through boilers or heat engines, or supply heat for industrial processes such as hot air generators. The combustion efficiency was determined to be a minimum of 96% using information from thermogravimetric analysis and X-ray diffraction. Magnetite is the main product formed from the combustion process, with small amounts of wüstite and hematite present as well. The presence of wüstite in the products implies rapid cooling post combustion since it is unstable at temperatures below 570 °C. Evidence from the particle burning temperature and the particle size distribution before and after combustion indicate that the iron particles burn in a diffusion limited heterogeneous combustion mode that produces micron size oxide products as theorized in previous works.

Abrégé

Face à la crise croissante de l'énergie et du climat, il est évident qu'il faut se tourner vers des énergies renouvelables propres comme le solaire, l'éolien et l'hydroélectrique. Cependant, un problème majeur avec ces sources intermittentes est de savoir comment stocker l'énergie excédentaire pour les périodes de forte demande ou de faible production (par exemple, la nuit, par temps nuageux, etc.). Un deuxième problème est de savoir comment transporter l'énergie produite vers les régions qui en ont besoin à travers le monde. Des métaux tels que le fer et l'aluminium ont été proposés comme vecteurs potentiels d'énergie sans carbone qui pourraient atteindre cet objectif, car ils ont des densités d'énergie similaires à celles des combustibles hydrocarbonés traditionnels, sont abondants dans la croûte terrestre et peuvent être transportés et stockés en toute sécurité. Un premier pas vers ce but est réalisé avec la conception et la fabrication d'un brûleur à fer turbulent. La conception fait appel aux travaux antérieurs sur la combustion des métaux ainsi que sur la combustion turbulente des solides dans les brûleurs à charbon pulvérisé. Des tests approfondis du brûleur ont permis d'obtenir la toute première flamme de fer pur auto-entretenue, stabilisant les flammes pendant de longues durées de plus de vingt minutes. Le brûleur opère à l'échelle du laboratoire avec une puissance thermique d'environ 10 kW et un système de captage cyclonique est connecté à la sortie de la flamme pour récupérer les particules d'oxyde de fer brûlées. La stabilité de la flamme de fer et l'efficacité du système de captage cyclonique ont permis de réaliser plusieurs expériences et diagnostics. Les expériences d'extraction de chaleur ont démontré le potentiel des flammes de fer pour créer de l'énergie par le biais de chaudières ou de moteurs thermiques, ou pour fournir de la chaleur à des processus industriels tels que les générateurs d'air chaud. L'efficacité de la combustion a été déterminée comme étant d'un minimum de 96% en utilisant les informations de l'analyse thermogravimétrique et de la diffraction des rayons X. La magnétite est le principal produit formé par le processus de combustion, avec de petites quantités de wüstite et d'hématite également présentes. La présence de wüstite dans les produits implique un refroidissement rapide après la combustion car elle est instable à des températures inférieures à 570°C. La température de combustion des particules et la distribution de la taille des particules avant et après la combustion indiquent que les particules de fer brûlent dans un mode de combustion hétérogène à diffusion limitée qui produit des produits d'oxyde de taille micrométrique, comme cela a été théorisé dans des travaux précédents.

Acknowledgements

I would like to begin by thanking my supervisor Professor Jeffrey Bergthorson for his guidance, support and constructive criticism throughout the course of my studies. His endless positivity and energy encouraged me to work harder and strive for more out of my work. His attitude instills a camaraderie that inspires everyone to do their best and helps others in the lab.

I was also fortunate to work with many excellent graduate students in the AFL. I would like to express gratitude to my fellow researchers Martin Aralov, Frederic Blais, Jan Palecka, Keena Trowell, Santino Salvo, Antoine Durocher, Kartik Mangalvedhe, Marie Meulemans and senior research scientist Sam Goroshin who provided valuable insights, showed me how the lab operated and made for lively conversations in and out of the office. And to my girlfriend Icoquih who pushed me to begin writing when I was putting it off and is always the first to proudly bring up my work with anyone we meet. In addition, I would like to acknowledge the Natural Sciences and Engineering Research Council of Canada and Tata Steel Ltd. for partnering on a Strategic Partnership Grant that helped fund my research.

Lastly, I would like to thank my family, Susie, Moish and Zohar for their continual love, support and encouragement throughout my entire life. I would not be who I am, or where I am today without you. To my father, who always pushed me to be my best, I am sorry you didn't get to see my thesis, but I am glad you got to see my work.

Contents

List of Figures

List of Tables

1 Introduction

1.1 Background

The world currently runs on fossil fuels. Out of the total 583 EJ of energy produced in 2016, 32% came from oil, 26% from coal, 22% from natural gas and only 5% from renewables, which mainly consists of hydroelectricity [1]. Within that, only 18% was used for electricity generation, while the rest was used as fuels for industry, transport and heat. In Quebec, we are fortunate that we are able to produce nearly all our electricity from hydroelectricity, and even have excess that is sold to other provinces and the United States [2]. However, despite the abundance in Quebec, hydroelectricity still only accounts for less than 35% of the total *energy* demand, the rest being made up of industrial consumption, transport and heating, which are supplied mostly by petroleum, natural gas and some biofuels [2]. Dominant as they may be, the time of fossil fuels is coming to an end. There are two issues facing the use of fossil fuels. The first is the simple fact that they are a limited resource. According to several researchers we are either passing or have passed Peak Oil [3, 4], the point beyond which the rate of oil extraction will begin to decrease permanently. We may soon be nearing Peak Coal and Peak Natural Gas [4], despite recent technological advances that are pushing back the peak of natural gas. There remains perhaps significant reserves of quote unconventional oil, fossil resources that are in difficult (i.e. not commercially viable) locations to extract. However they have low energy returns on investment and therefore low economic returns [5]. The second issue is anthropogenic climate change; the increase in global atmospheric carbon dioxide levels and other climate forcing molecules by human actions [6]. According to the Intergovernmental Panel on Climate Change, global CO_2 emissions must be brought down to net zero by 2050 to avoid global warming above 1.5 °C [7]. Keeping global temperature increases below this threshold is essential in maintaining ecosystems, biodiversity, food security and diminishing the intensity and frequency of extreme weather events [8].

It is clear that to solve this problem there is a need for carbon free renewable energy systems. According to several different studies, there is enough solar, wind and hydro to meet the world's energy need many times over [9, 10, 11]. However, a key problem that remains unsolved is how to store all this energy for periods when the renewables cannot generate electricity, for example during the night or on windless days. In addition to storing the energy, a solution is also needed to be able to trade this renewable electricity like a commodity, so that regions without renewable resources

can have access to power, similar to how countries currently import oil or other fossil fuels. A solution to this problem was proposed in 2015 by Bergthorson et al [12]. They suggest using metals as carbon-free, recyclable energy carriers. Metals have high energy densities comparable to typical hydrocarbon fuels such as gasoline and coal, and are far superior from an energetic point of view than lithium ion batteries or compressed hydrogen as seen in Figure 1.

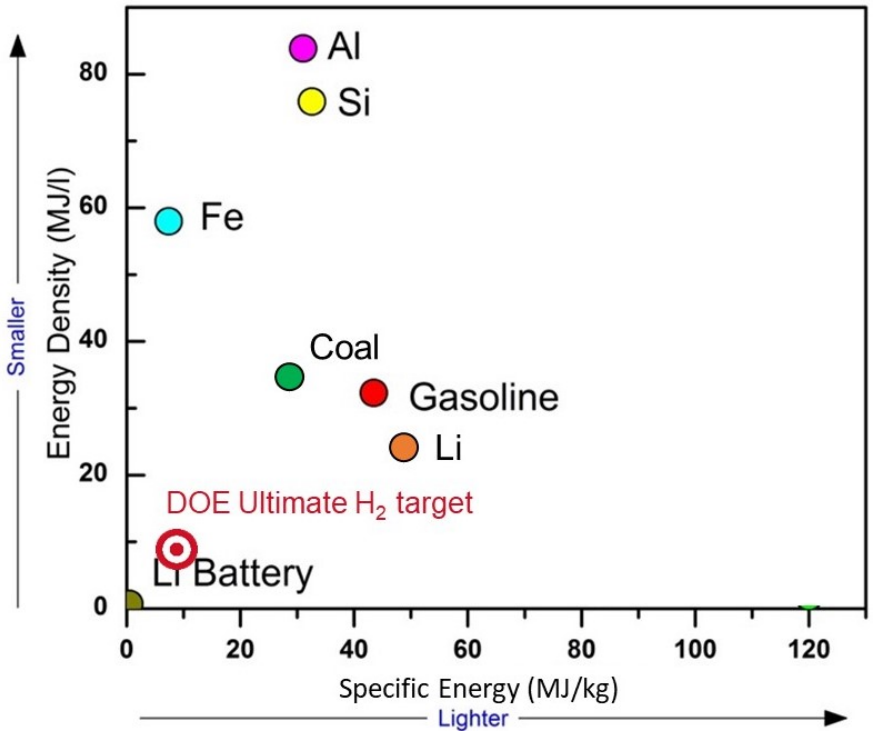

Figure 1: Energetic content of various hydrocarbon fuels and metals

Some metals such as iron and aluminum even have greater energy densities than gasoline and coal. The concept of metals as clean energy carriers forming a circular economy is shown in Figure 2. Metals can be burned in air or reacted in water to produce heat, which can then be captured and used to generate electricity or power industrial processes like hot air generators. The products of those reactions are solid metal oxides which are collected after combustion, and subsequently can be reduced (recycled) using clean renewable energy, thereby acting as an energy storage system. One of the main advantages of this idea is that excess renewable energy is stored in the chemical bonds of the metals and not simply as potential, like in pumped hydroelectricity or compressed gas systems.

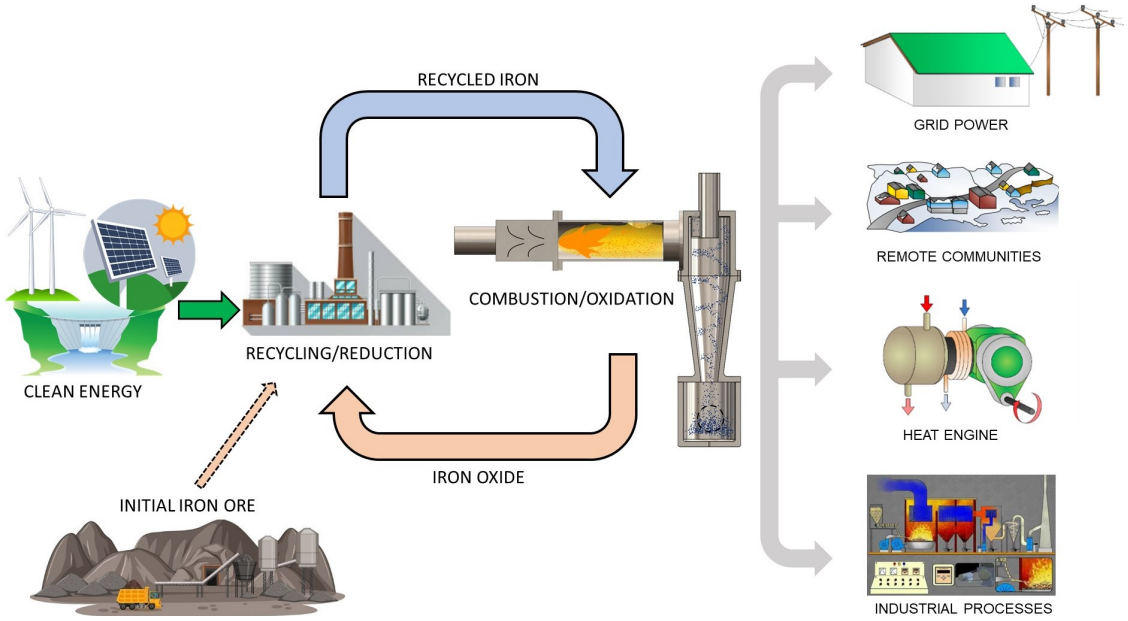

Figure 2: Sustainable Metal Fuel Cycle

Many metals, such as iron, can safely be stored for extended periods of time and are already traded globally as a commodity [13]. Metal powder can be shipped to the point of use, reacted, and then the metal oxide sent back to location of renewable energy where the recycling takes place. Figure 3 shows the quantity in gigatonnes of various metals that would be required to power the world for a year, as well as their respective reserves. From this point of view, iron is a promising candidate for use as an energy carrier because of its abundance. Moreover, since the process is recyclable, there is room for increases in energy demand in the future.

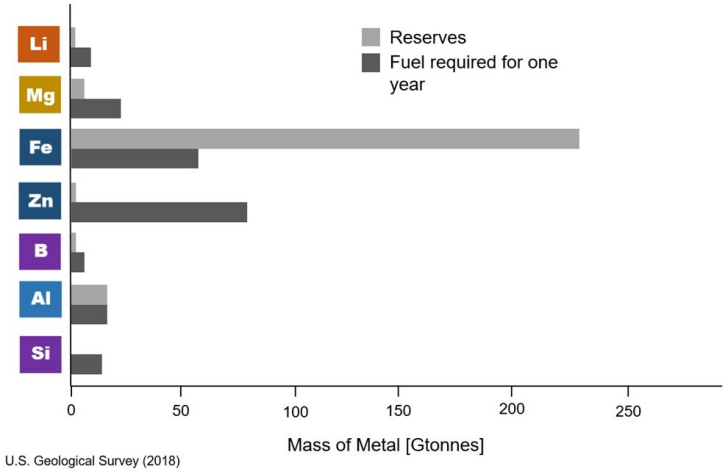

Figure 3: Reserves and quantities required of various metals to power the world for a year.

1.2 Fundamentals of metal combustion

The study of the combustion of metals has generally been limited to accidental industrial explosions [14, 15] and metalized solid rocket propellant [16]. Magnesium and aluminum were of special interest because of their relatively light weight and high energy content. They are commonly used in modern solid rocket propellant [17]. As the need for better performance of propulsion and explosive systems became apparent, the field grew and different frameworks such as chemical kinetics were applied to metals.

The combustion of solid particles in a two phase flow is governed by two competing processes: the chemical reaction rate with the fuel particle and the diffusion of oxidizer to the particle surface [18, 19]. The rates can vary, and if one is slower than the other it becomes the rate limiting step, which then determines the combustion regime, either kinetically limited or diffusion limited. Each combustion regime has different specific characteristics, which are shown in Figure 4. In the diffusion limited regime, the reaction occurs faster than the oxidizer can be transported to the particle surface and forms a gradient in oxidizer concentration, as seen in the third pane of the figure. The reaction also releases heat faster than it can be transported away, such that the temperature at the particle surface is greater than the bulk gas temperature, as seen in the second pane. In the kinetically limited regime, there are no gradients in temperature or oxidizer between the particle and the bulk gas as seen in the first pane.

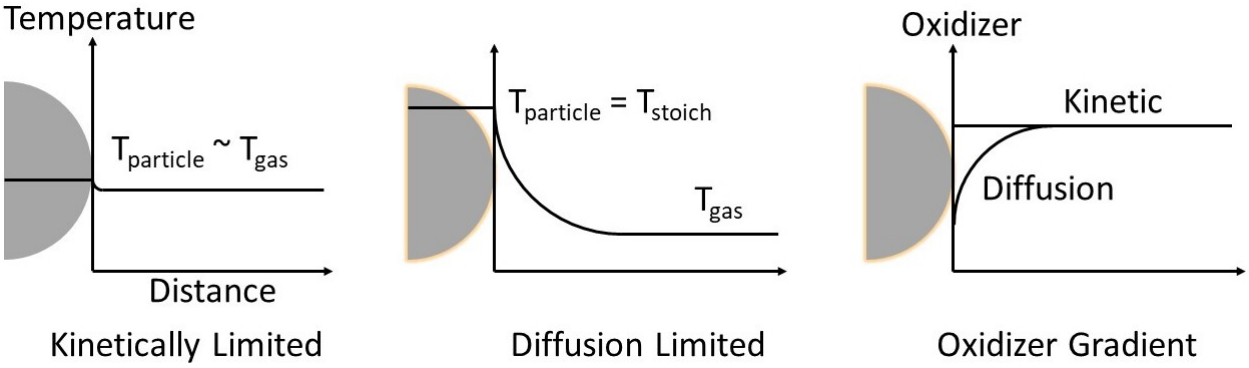

Figure 4: Temperature profile in the kinetically limited and diffusion limited regime.

Initially, particles begin reacting in the kinetically limited regime and release energy in the form of heat. If the heat generated from the reaction becomes greater than the diffusion of heat away from the particle surface, the particle then transitions to the diffusion limited regime. This transition is referred to as particle ignition, and is accompanied by a significant increase in temperature. In the

diffusion limited regime, a micro diffusion flame is formed around the particle and it burns at its flame temperature, independent of the surrounding gas temperature. In a suspension of particles in an oxidizing medium, the reaction rate can be increased by a feedback mechanism termed the collective effect [20]. Heat released by the reacting particles is transferred to the gas, which causes an increase in temperature. This rise in temperature then increases the reaction rate, increasing the heat release rate at each particle's surface. This positive feedback loop occurs until the reaction suddenly proceeds to completion, because of the exponential dependency on temperature of the Arrhenius kinetics. This process is termed reaction onset to distinguish it from particle ignition, since the individual particles may or may not undergo ignition [21]. This is a unique feature of heterogeneous combustion of solids, whereby the mixture can burn with particles either completely in the diffusion limited or with some in the kinetically limited regime as well.

Solid combustion materials can either burn heterogeneously, i.e. in a distinct two phase flow, or in a vapor phase [22]. Coal is an example of the latter, being made up of carbon, moisture, ash generating minerals and a variety of hydrocarbons. During combustion, the hydrocarbon content quickly volatilizes and reacts, leaving the carbonaceous char to burn heterogeneously [23]. The varying levels of the coal constituents determine how much char is produced and the maximum efficiency of combustion. Metals on the other hand, can either burn heterogeneously or in a vapor phase, depending on the flame temperature and the boiling temperature of the metal. If the flame temperature is greater than the boiling temperature, the metal will vaporize and the reaction will take place in the vapor phase. If the flame temperature is less than the boiling temperature, the metal will burn heterogeneously on the particle surface. This is known as the Glassman Criterion [24]. This criterion is applied to several different metals shown in Figure 5, where the flame and boiling temperature were calculated with the Thermo thermodynamic software for each metal. Several metals including iron are shown to burn heterogeneously, while a handful like aluminum and magnesium are expected to burn in the vapor phase. The y-axis of the plot shows the partial pressures of the oxides, which plays a role in the formation of the reaction products. Figure 6 shows the possible oxides that are formed in metal combustion, depending on the burning mode and partial pressures. For a metal droplet reacting in the vapor phase, burning mode A, the reaction takes place between the metal vapor and the oxidizer away from the particle surface. This results in the formation of nanometric oxides. For a particle undergoing heterogeneous combustion there are two possibilities. The metal can burn in mode B, where the partial pressure of the oxides is such that the products formed are gaseous suboxides which results again in nanometric oxides. Alternatively,

the metal can burn in mode C, where the reaction at the particle surface creates a porous solid metal oxide shell that grows around the particle, creating micron sized oxides, depending on the initial particle size. The shell would be porous enough not to impede the rate of oxygen diffusion to the particle surface. For this to occur, the partial pressure of the oxides must be below 10^{-4} bar [12]. However, it has been shown that metals can burn with a liquid molten oxide shell as well [25]. In this instance, oxygen dissolves into a molten iron oxide layer that does not have a defined stoichiometric ratio.

Clearly, to have an efficient particle collection system to enable recycling of the metal oxides, larger oxide products are favorable. It is extremely difficult to collect nanoparticles and often requires fine filters that would make it impractical to separate the particles from afterwards. They also represent a respiratory health hazard. Forming larger oxide products permits various different particle collections systems to be implemented, making it easier achieve complete collection. Based on the data from Figure 5, only iron is expected to burn in mode C with air at stoichiometric conditions, creating larger oxides than the initial particle size. This makes iron an ideal candidate for use as an energy carrier in a combustion and collection system.

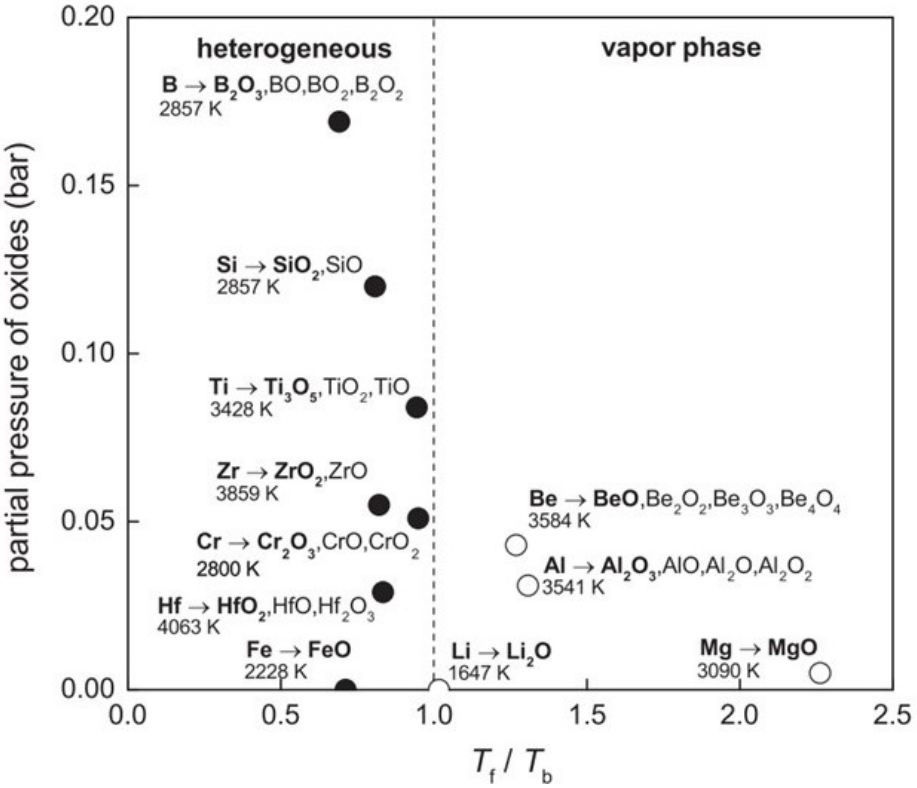

Figure 5: Classification of metal particle combustion mode based on thermodynamic calculations. Source: Reprinted from [12].

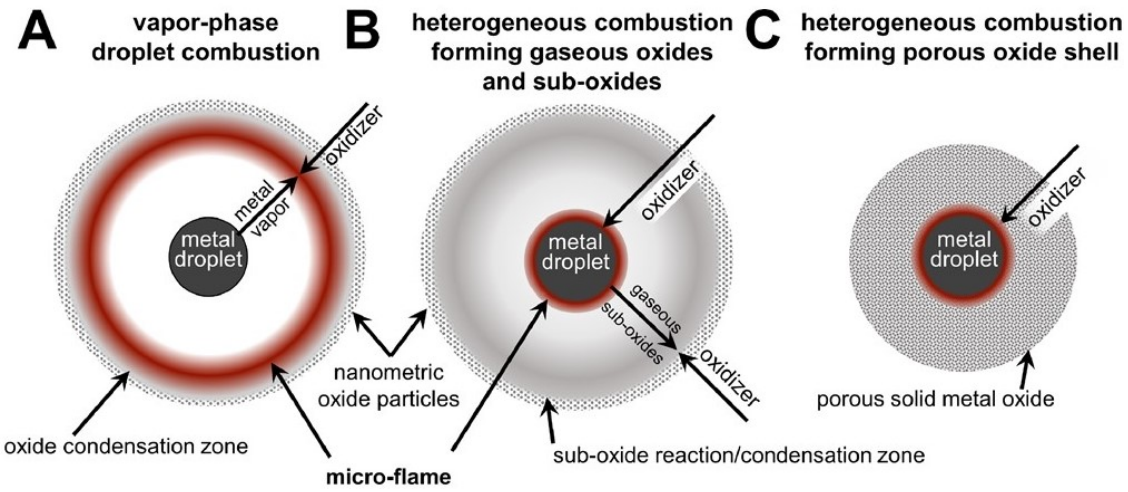

Figure 6: Modes of particle combustion in the small Biot number regime. Source: Reprinted from [12].

1.3 Metals in flames

Much of the recent scientific work on the combustion of metals has focused on single particle experiments and laminar flames. Single particle experiments on aluminum [26, 27, 28], magnesium [29], boron [30] and iron [31] have been carried out to determine the burn time of the individual particles. The burn time of particles roughly follows the d^2 law, with larger particles burning for proportionally longer times. An interesting phenomena is encountered with iron particles where the burning terminates with a micro-explosion rather than a slow fading of the luminosity. This is thought to be due to dissolved gasses that are present in the metal that expand as they are heated and eventually explode out of the particle. Carbon is a likely element found in iron, since the smelting of iron ore often uses a carbon based reduction process with coke as the heat source and reductant. As the particle oxidizes, the carbon also oxidizes forming gaseous CO_2 which cracks the particle. However, work is being done on reducing iron ore with hydrogen as the reducing agent [32] and many companies are shifting towards this technology. A second possibility, is that the expanding gas is actually dissolved oxygen in the molten iron oxide that is outgassed during cooling. This phenomenon has been seen in pure iron-oxygen environments [33, 34] and from the iron-oxygen phase diagram is only expected to occur when there is liquid iron oxide with an oxygen content greater than 28.5 w% [35].

The burning velocity is a fundamental parameter of gas flames that is independent of flame geometry and is defined as the speed at which an adiabatic, un-stretched, one-dimensional laminar

flame propagates through a quiescent mixture of unburnt reactants. Work has been done on particulate fuel suspensions to determine if the concept of a burning velocity can be applied to metal flames. Different laminar flames have been studied because their simpler geometry allows for the burning velocity to be more easily calculated. A range of flame/burner configurations have been used, such as Bunsen burners [36], freely propagating flames in tubes in both normal [37] and microgravity environments [38], spherically expanding transparent balloons [39], freely propagating flames in dust clouds [40, 41] and counterflow burners [42]. A study of flame speed measurements in aluminum suspensions on a counterflow burner [42] compared the results of the different flame configurations that used the same batch of powder and concluded that the concept of a laminar burning velocity could be applied to flames propagating through dust suspensions. Most recently this counterflow configuration was applied to iron [43], with the one dimensional flame allowing particle imaging velocimetry and the measurement of the iron burning velocity for the first time. However, despite this vast body of work on particulate combustion, to date no work has been done on turbulent iron flames. The construction of a stabilized turbulent iron burner will open a new avenue of study for metal combustion, allowing turbulent burning velocities to be measured, combustion products to be examined and measurement of NO_x formation among other things.

1.4 Turbulent combustion of solid fuels

Most of the work on turbulent combustion of solids has been in coal burners since they have been ubiquitous for the last century. Many comprehensive works have been written on the functioning, design and operation of the different types of coal burners [23, 44, 45, 46], with pulverised coal burners of the greatest interest because of the comparable particle sizes to metal powders previously studied. Special interest is paid to swirl burners with air staging that permit low NO_x emission coal combustion [47, 48]. Swirl burners have been used for both gas and coal combustion to increase flame stability for many decades, but it wasn't until the late 1960s that progress was made in understanding these swirling flows [49, 50]. With continued pressure on the coal and gas industry to reduce its harmful emissions (SO_x, NO_x, CO_2), there has been renewed interest in swirling flows and a focus on numerical modeling [51, 52, 53, 54].

1.5 Objectives

In broad terms, the goal of this masters project is to take the first step in making metal fuels as carbon free energy carriers a reality. In order to do so, the following specific objectives are established:

1. Design, build and test an iron powder burner that can create a self-sustained pure iron flame
2. Assess the heat transfer capabilities of the flame for power generation purposes
3. Determine the combustion efficiency through examination of combustion product composition and morphology

1.6 Overview

The thesis is comprised of two major sections. The first addresses the design, manufacturing and testing of the burner and related systems. The design envelope, sources of inspiration and the rationale of the choices made is explained. Material selection and machining techniques are briefly discussed. This is followed by the process of testing the individual components, the system as whole, and the ensuing results of that work. Lastly, a short section on the performance of the burner is presented. The second section assesses the two latter objectives, heat extraction from the flame and combustion efficiency. It contains methodology, results and discussion sections on the tests performed on the burner. It begins with a brief background on the need for heat transfer, heat transfer mechanisms and the related difficulties with metal flames as well as the need to evaluate the combustion efficiency. This is followed by the methodology and equipment used to carry out experiments. Then, the results of these experiments and analysis is presented. It concludes with a discussion of the findings and their importance. Lastly, an overall conclusion for the work carried out during the thesis is given.

2 Burner Design

2.1 Design Parameters

All designs must begin with input parameters or requirements that allow the creation of a design envelope. The fewer criteria that need to be met, the larger the design envelope and the more choices that are left up to the designer and various solutions may be acceptable. Conversely, the more requirements there are, the more the design space is constrained and the quicker ideas can be eliminated and solutions arrived upon. For this project, the design parameters were as follows:

- Roughly 10 kW thermal energy flame
- Create self-sustained iron flame
- Turbulent flame for improved mixing and heat generation
- Compatible with larger particle sizes
- Integrated ignition system
- Avoid using premixed methane-air for safety
- Machinable at McGill University

Though fairly broad, these criteria form the design envelope and impose some critical constraints. The power requirement of the flame, roughly 10 kW of thermal energy, i.e. the amount of energy stored in the particles that can be released as heat, sets the scale of the burner system. Since the power of the flame is directly linked to the amount of iron powder dispersed to the burner, the 10 kW criteria determines the iron flow rate. The need for turbulent mixing and creation of a self-sustained flame guides the design towards current combustion techniques used in the gas and coal combustion industry, as will be discussed shortly. The ability to use larger particle sizes necessitates good turbulent mixing as well as the need for faster flow velocities. Pilot flames are commonly used to ignite and sometimes aid stability in combustion systems, but it is important to keep in mind the goal of the project is to create carbon free power. Therefore, the goal is to minimize the amount of fossil fuel used, which means a small portion of the energy being devoted to the ignition flame and it being extinguished once the iron is ignited. With the addition of a gas flame comes the safety concerns of mixing oxidizers and combustible gas, which can lead to

explosions if not carefully designed. Lastly, the need to be able to manufacture the apparatus at McGill means that conventional machining techniques and materials must be used. This helps rule out certain potential designs that cannot be manufactured at small scale effectively.

2.2 Flame Stabilisation

As discussed in the literature review, pulverized fuel (PF) coal burners are a good place to begin when considering the design of an iron powder burner. PF burners use solid fuel particles and so have to deal with particle conveying, establishing good mixing and creating a strong turbulent region to ensure particles don't exit the flame prematurely. However, as mentioned, the key difference is that though solid, coal is highly volatile with up to 44% percent evaporating [55], and the rest turning to char and fly ash. A standard state of the art PF burner generally consists of a central pipe housing an oil or gas pilot flame, an annular region carrying the pulverized coal and then two annular regions which direct air to create a turbulent zone and ensure complete combustion [23, 45]. An important feature of these burners is the use of turbulence to create a central recirculation zone, which allows flames to be stabilized more easily and also allows higher velocity flow rates to be used. The general principle is to create a turbulent region where the velocity field breaks down and the axial velocity of the incoming flow is actually reversed. A diagram of this phenomenon can be seen in Figure 7. The diagram depicts a flow that is exiting a nozzle with a velocity towards the right and that a portion of the flow gets directed along streamlines towards the outside, while a central section directly in front of the nozzle is actually flowing in the opposite direction.

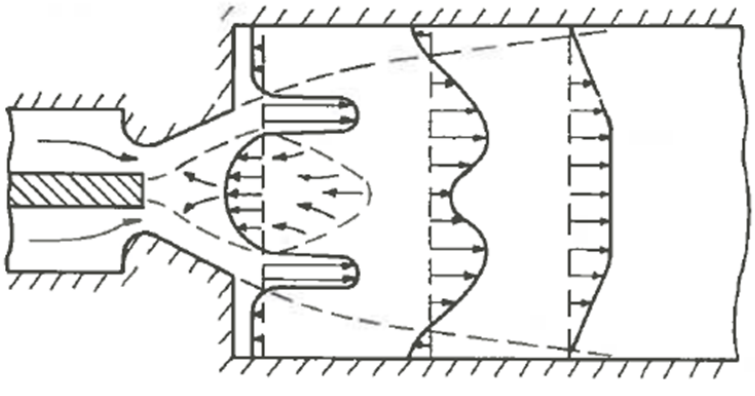

Figure 7: Central recirculation zone. Source: Reprinted from [49]

This flow reversal is what allows high flow rates of fuel to stabilized and ensures good mixing of the incoming reactants with the hot combustion products. The recirculation zone is created

with the use of mechanical devices or designs which direct the air flow in a swirling pattern. There are two main types of stabilization devices: bluff bodies and so-called "swirlers". Bluff bodies are simply objects, such as discs or cones, that are placed in the way of the flow and create a recirculation region behind them in their wake. A common example of this found in nature are eddies caused by protruding rocks in a river. An example of this is shown in Figure 8, where a central recirculation zone is clearly seen directly behind the rock.

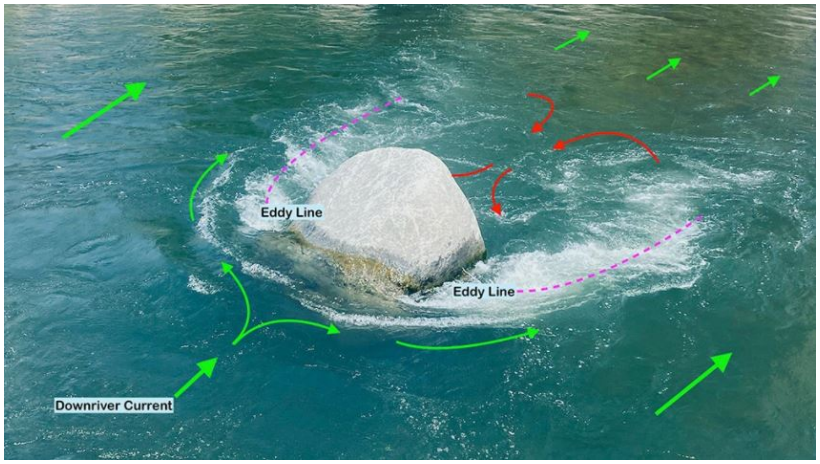

Figure 8: Eddies in a river - An example of central recirculation zones in nature. Source: https://www.calipaddler.com/blogs/paddle-articles/understanding-eddy-currents-in-rivers

This flame stabilization technique is used in the gas combustion industry, however when dealing with solid fuels it leads to several complications. First of all, there is the likelihood of particle sintering and buildup on the bluff body. As the goal of the burner is to operate for as long as possible with minimal maintenance, having to extinguish the flame and shutdown the burner to frequently clean or replace the buff body is not a good option. Secondly, there is a risk that the particles, because of their inertia, will not be able to follow the flow into the eddy behind the bluff body. Lastly, there is the difficulty of designing a suspended bluff body such that the supports do not interfere with the flow or get corroded. For these reasons, the bluff body stabilization technique is ruled out.

Swirlers are mechanical devices that rotate flow tangentially so as to create varying degrees of recirculation downstream. Their ability to do so is called swirl and is characterized by the swirl number, which is a non-dimensional characteristic of rotating flow. The swirl number, as defined by Beer and Chigier [49], is

$$S_0 = \frac{G_\theta}{RG_x} \tag{2.1}$$

where S_0 is the swirl, G_θ is the axial flux of angular momentum, R is the outer radius of the annulus and G_x is the axial flux of the axial momentum. These two axial fluxes can be expressed by the following equations

$$G_\theta = \int_0^R (Wr)\rho U 2\pi r \, dr \tag{2.2}$$

$$G_x = \int_0^R U\rho U 2\pi r \, dr + \int_0^R 2p\pi r \, dr \tag{2.3}$$

where U and W are the axial and azimuthal velocity components and p is the static pressure.

However, in practice it is difficult to estimate the pressure integral term because the static pressure is strongly dependent on the geometry of the swirler. According to the authors as well as Martin [56] G_x can be well approximated by eliminating the pressure term completely if the input velocity at the swirler is used instead of the jet distribution. With this change, the modified swirl number S becomes

$$S = \frac{\int_0^R UWr^2 \, dr}{R\int_0^R U^2 r \, dr} \tag{2.4}$$

The swirl number is used to characterize the amount of recirculation, with higher swirl numbers indicating more strongly swirling flows. There exists however a cutoff, below which there will be no central recirculation zone. Swirl is therefore broken into two categories, weakly swirled flows and strongly swirled flows. The generally accepted value of the onset of strong swirl is 0.6 [49]. Below this value, the flow will have increased turbulence and entrainment, which will lower the velocity, but there will be no defined central recirculation zone. This can be used to create a low-swirl flame as is the case in low NOx low swirled burners [57]. For the case of strong swirl, eventually the adverse pressure gradient along the axis of flow becomes too large for the incoming flow and a recirculation zone in the form of a torroidal vortex is formed. As mentioned, this is desirable because it forms a well mixed zone and heat storage area near the burner nozzle that incoming chemical species can react with, thereby helping stabilize the flame.

There are three general methods of swirl generation, which are depicted in Figure 9. The first method is the simplest and consists of having tangential entry of the fluid into a cylindrical duct. Schematic a in the figure shows a design with four tangential air entry ports feeding into a circular duct, which provide the air that induces rotation in the flow. Not pictured on the diagram

are the axial air inlets, which provide other combustion air. The advantage of this design is its simplicity and the ability to control the swirl continuously from zero to some maximum value dependent on the required airflow, since the swirl is essentially the ratio of the tangential and axial air momentum. With the required combustion air being fixed, the amount of air being supplied from the tangential entry ports can be varied with the balance supplied from the axial entry ports. Therefore, by changing the proportion of air being supplied tangentially, the swirl number can be directly controlled.

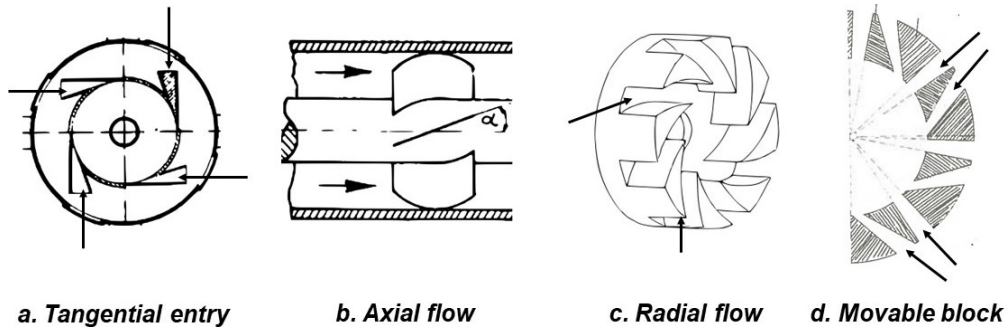

Figure 9: Methods of swirl generation and swirlers. Source: Adapted from [49]

The second method is through the use of axial guide vanes. As seen in schematic b, flow in an annular region is passed through a set of guide vanes that are rotated from the axis. As the flow passes through this region, it is turned in the direction of the vanes, which creates the rotation that leads to swirling flow. As the angle of the vanes measured from the axis α is increased, the swirl is increased since the air is turned even more. However, increasing that angle too greatly can cause large pressure drops since at higher angles the guide vanes simply become blockages. Other factors such as the number of vanes as well as having curved vanes can improve the efficiency by guiding the air through the channels with less resistance. The final method is with the use of radial guide vanes. As the name implies, guide vanes are set perpendicular to the flow and the air must enter through these channels radially before being directed along an annular region axially. The guide vanes are set at an angle to the center, such that the air passing through them is redirected tangentially with respect to the central axis. As in the axial vane swirler, the larger this angle, the more air is directed tangentially, which creates a stronger swirl. This is shown in schematic c, as the air enters the channels indicated by the arrows, and then flows along the axis of the central hole. The central cylinder where the hole is located is not pictured, nor the duct which houses the swirler. Both the axial vane and radial vane types have fixed swirl numbers, as their geometry is fixed and the ratio of air being imparted with tangential motion to axial motion

cannot be changed. Schematic d shows a special subclass of radial vane swirlers, called the movable block swirler, which was developed by the International Flame Research Foundation at its facility in Ijmuiden, the Netherlands. It is comprised of two annular plates with wedge shaped blocks or teeth. The plates are interlocked with the blocks facing each other such that they mesh and create a series of alternating tangential and radial channels. One plate is held fixed to the apparatus, while the other has the ability to rotate. By rotating one plate, the radial channels can be shut and the tangential ones opened further, or vice versa. This gives the swirler the ability to continuously vary the swirl from zero (fully radial channels) to some maximum value (fully tangential channels), unlike the other guide vane swirlers.

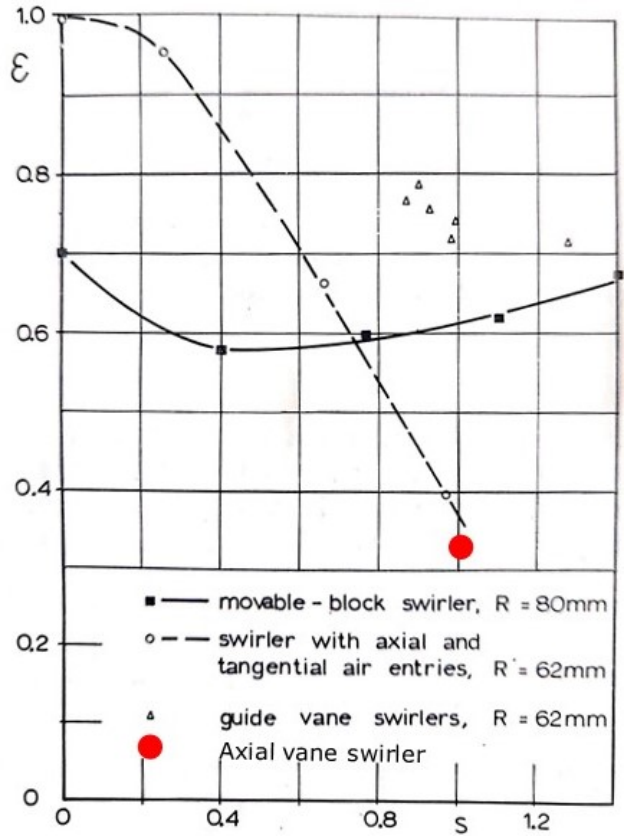

Figure 10: Efficiency of swirl generation as a function of swirl number for different swirl generators. Source: Adapted from [49]

Each type of swirl generator has its advantages and disadvantages. As mentioned, the tangential entry method is fairly simple and often implemented with a single entry into a cylindrical duct and has the benefit of being continuously variable from zero to a maximum value. However, it suffers from a low energetic efficiency of swirl generation as well an overall difficulty in achieving larger

swirl numbers. Axial vane swirlers have the advantage of being compact and easy to fit into a design, however they are difficult to manufacture at small scale because the guide vanes need to be thin. In addition, they also have low swirl efficiency and are better suited to low swirled burners and additive manufacturing applications. Radial vane swirlers, including movable block, are able to create high degrees of swirl with relatively high efficiency and the movable block type allows the continuous adjustment of swirl. However, due to the fact that the air must enter radially, the overall diameter of the burner must increase to accommodate that. Figure 10 shows the efficiency of the different types of swirl generators. The value for axial vane swirlers were added from work done by Mathur and Maccallum [58]. The efficiency shown here is defined as the the ratio of the flux of kinetic energy of the swirling flow through the burner throat to the drop of static pressure energy between the air inlets and the throat of the burner [49]. Clearly radial vane swirlers are superior in their ability to create high swirl efficiently.

2.3 Stratified burner

Achieving complete combustion and reducing the formation of NOx are important aspects of any new burner. To that end, the notion of creating a stratified burner is investigated. In stratified burners, the equivalence ratio, defined as the actual fuel to air ratio as compared to the stoichiometric ratio, is not uniform throughout the burner. The goal is to create different regions where the local equivalence ratio varies to control the combustion process and the combustion products. Generally, the first or inner section is kept fuel rich in order to ensure that combustion can be sustained. Then successive sections are kept fuel lean, i.e. more air than fuel, which allows all the remaining fuel to mix with sufficient oxidizer in order to ensure complete combustion. The advantage of this sequencing is that it maintains the temperature lower than simply having the stoichiometric mixture reacting. This can be seen from Figure 11, where near stoichiometry with a ϕ slightly greater than 1 the temperature is maximum, and then on either side with both fuel rich and fuel lean mixtures the temperature is lower. Having the combustion take place at lower temperatures helps reduce NOx significantly, by stopping its formation from the thermal pathway. The idea is to extend this concept to iron flames to enable complete combustion and minimize NOx formation.

Previous work has shown that increasing the metal concentration past the stoichiometric point towards fuel rich conditions has little effect on the burning velocity [41], as seen in Figure 12. This is because the metal particles are very dense compared to the gaseous oxidizer, and so increasing their

concentration does not significantly displace the air or dilute the oxidizer concentration. Therefore the heat that can be released is only dependent on the oxidizer, and the additional metal particles simply act as a small heat sink by increasing the heat capacity of the mixture. This means that a fuel rich section of the iron burner will likely behave similar to a stoichiometric mixture. The reduced sensitivity of burning velocity on particle concentration also indicates that metal flames can be stabilized more easily with a fuel rich mixture. Having a fuel rich mixture will also help ensure flame stability despite particle concentration fluctuations that are common to solid fuel dispersion systems. As opposed to standard rich-quench-lean burners used in the gas turbine industry, where there is a stepped process with an initial fuel rich combustion, followed by air addition which "quenches" the flame to some extent, lowering its temperature and then allowing fuel lean combustion, the goal with the iron burner is to have one stratified flame to accomplish this. Combined with the knowledge gained from coal burners and swirl stabilization, the general concept for the metal burner is a highly fuel rich central flow of iron and air, which will be surrounded by a swirling flow with an excess amount of air. This will allow a fuel rich inner zone that will mix with the swirling air to stabilize the flame with the outer and downstream regions being slightly fuel lean to ensure enough oxygen is present to allow complete combustion. An added benefit of this design is the potential to reduce the formation of nanometric oxide particles. By keeping the temperatures lower the likelihood of nano-oxide production is lower.

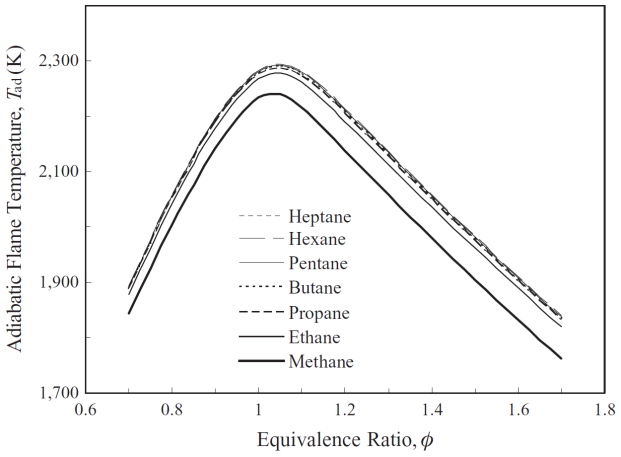

Figure 11: Adiabatic flame temperature as a function of equivalence ratio for various fuels. Source: Reprinted from [59]

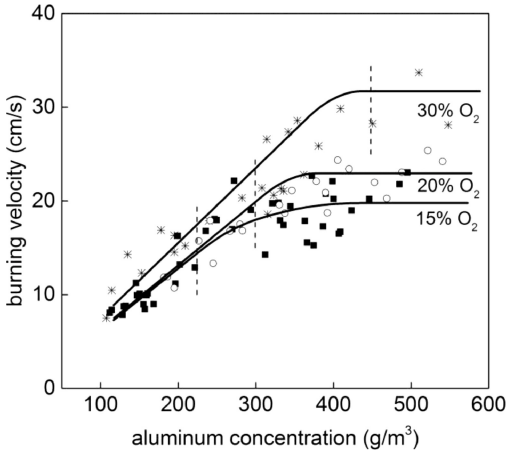

Figure 12: Burning velocity of aluminum flames as a function of concentration. Source: Reprinted from [41]

2.4 Ignition System

In general, combustion systems have integrated ignition systems. For larger systems such as coal or oil burners, this generally takes the form of a pilot flame that is housed within the burner itself and does not require external adjustments to the burner. The idea is to use an easily stabilized high heat source such as a methane flame to ignite a more difficult one such as coal. Once the actual fuel source has been stabilized in a flame, the pilot flame can be extinguished.

To make this burner as safe as possible and also use a design that can be scaled to larger sizes, a methane pilot flame is chosen as the ignition source for the iron powder. In terms of safety, multiple factors need to be considered. The foremost of which is the risk of explosion with premixed flames, because there is the possibility of the flame propagating back down to the fuel lines. This phenomenon is termed flashback and is caused by the burning velocity of the flame being greater than the incoming flow velocity. Several design decisions are taken to mitigate this risk. First of all, the mixing of methane and air will only happen inside the burner itself and not prior. The methane and air will be supplied to the burner into separate chambers and mix downstream in a cylindrical duct to minimize the region of premixing. Secondly, the integrated mixing region will be equipped with a flame arrestor in the form of small ceramic beads, which help in the mixing of fuel and air, but also act as a barrier to stop the flaming traveling in the opposite direction. Lastly, the chambers into which the air and methane are supplied will be equipped with pressure relief valves, such that any excess pressure caused by a flashback event can be safely ejected from the burner.

Another consideration is how to safely ignite the pilot flame. It is not practical, nor feasible, to ignite it manually each time. Therefore a high voltage spark generator is selected as the method of ignition because it is simple, reliable and can be integrated easily into a burner design. Several inexpensive spark generators are available on the market. They essentially consist of wrapped coils acting as a transformer, operate on batteries in the voltage range of 3V-9V and have an arcing distance of roughly 1 cm. It is simple to extend the electrodes and integrate a momentary push button switch to operate the spark generator and ensure a safe working distance from the burner.

The final aspect to consider for the design of the ignition flame is the required heat output in order to size it. The goal of the project is to produce a zero carbon metal flame and so it is important to minimize any other sources that could produce CO_2. For that reason the power of the methane flame will be limited to roughly 10% of the burner power. Having such a low proportion

of the power come from the pilot flame also has the advantage of allowing the burner to be operate as a hybrid methane-iron burner. This is beneficial in case it is difficult to create a self-sustained iron flame, since it would allow a flame to be easily stabilized while still being a predominantly iron flame. With the burner power set to 10 kW, that means a 1 kW methane flame is required. The heating value of methane is well-known so the flow rate of methane and air required to create a stoichiometric mixture is easily calculated.

2.5 Preliminary Design

With the information gained from the previous sections, a preliminary design is established. Based on the discussion of swirlers, the movable block swirler is selected as the best choice. The advantages of high swirl number and good swirl generation efficiency, combined with the ability to have variable swirl is a key factor for an experimental design. In addition, the machinability of the swirler is very important. It is not feasible to machine an axial vane swirler and there is limited welding capability at the McGill Machine shop, which rules out alternative fabrication options. Without welding, the tangential entry swirl generator is also difficult to make and has low performance compared to movable block swirlers, so is not of interest at the moment. The movable block swirler on the other hand can easily be machined on a 3-axis CNC available at McGill and has a relatively simple geometry. The concept of the stratified burner coupled to the difficulty in dispersing powder leads to the decision that the central flow will be a fuel rich mixture of iron and air. The iron powder must be dispersed in a pressurized flow and have as few impediments in its path as possible. Unlike a gas, it is difficult to split up the flow into multiple streams and disperse into complicated geometries, as the powder will simply build up and clog the line or not be dispersed. The surrounding flow will be the air and methane required to create the ignition flame. In this way, the heat of the flame is in close proximity to the iron flow to ignite it. The subsequent flow surrounding the pilot flame is the swirling air that will stabilize the flame and lower the equivalence ratio. It is not feasible to have the iron flow be the swirling flow, since the iron powder will not be able to pass through the swirler effectively. All of these elements can be seen on the general design schematic of the burner shown in Figure 13.

As stated, the methane and air will only mix in the final section of the burner, right before combustion so that there is limited space for the flame to flashback. The tertiary air flow is fed into a plenum where the pressure can equilibrate before passing radially through all the swirler vanes and being redirected in the axial direction. Some distance is given between the swirler and the

burner outlet to allow for the swirling flow pattern to form. The addition of a divergent section at the outlet of the burner called a quarl helps to increase the swirl and the reverse mass flow rate. The burner is connected to a combustion chamber that is a large cylindrical duct. This has several benefits including containing the flame, guiding the exhaust to the particle collection system and ensuring that only the air provided to the burner is available to react with the iron powder.

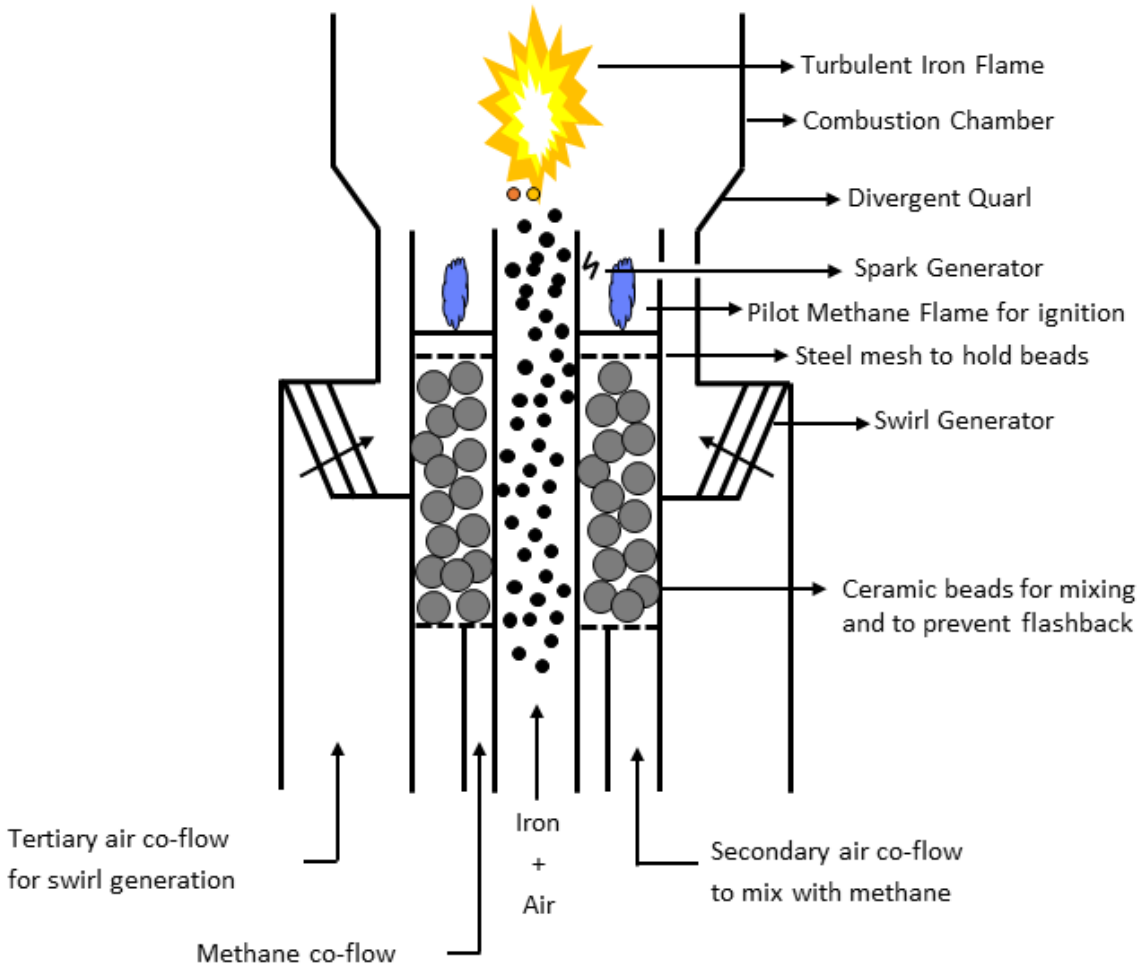

Figure 13: Basic design schematic of turbulent iron burner.

2.6 Detailed Design

With the general design decided, the process of detailed design of the components can begin. The first element to calculate is the iron flow rate since it will govern the other parts. The required iron flow rate to produce a 10 kW flame is calculated using the heat of formation and stoichiometry as follows. It is assumed the reaction taking place is the simplified overall reaction of pure iron and

air forming magnetite

$$3Fe + 2O_2 \rightarrow Fe_3O_4 \tag{2.5}$$

The energy produced per gram of iron is based on the energy release of the reaction, which is determined by the heat of formation of all the elements. The heats of formation of iron and oxygen are zero since they are in their elemental state. The heat of formation of magnetite is $\Delta_f H^\circ(Fe_3O_4) = -1120.9\,kJ/mol$ according to the National Institute of Standards and Technology (NIST) [60]. Therefore, the energy release of this reaction is

$$\Delta H^\circ{}_{(rxn)} = \Delta H^\circ{}_{(P)} - \Delta H^\circ{}_{(R)} \tag{2.6}$$

$$\Delta H^\circ{}_{(rxn)} = \Delta_f H^\circ{}_{Fe_3O_4} - (3\Delta_f H^\circ{}_{Fe} + 2\Delta_f H^\circ{}_{O_2})$$

$$\Delta H^\circ{}_{(rxn)} = -1120.9\,kJ/mol$$

The negative symbol of the heat of reaction indicates that the reaction is exothermic, which means that it releases energy. To convert this value into energy per gram of *fuel* requires the molar mass of iron which is 55.85 g/mol. Recalling that 3 moles of iron are required for this reaction, this yields

$$\Delta E_{Fe} = \frac{1120.9\,kJ}{mol\ Fe_3O_4} \cdot \frac{1\ mol\ Fe_3O_4}{3\ mol\ Fe} \cdot \frac{1\ mol\ Fe}{55.85\ g\ Fe} = 6.69\ kJ/g_{Fe} \tag{2.7}$$

To determine the mass flow rate of iron the required power is simply divided by the energy of the reaction per gram of iron.

$$\dot{m}_{Fe} = \frac{10\,kW}{6.69\,kJ/g} = 1.5\ g/s \tag{2.8}$$

To determine the amount of air required for the burner, the equivalence ratio must be chosen. The equivalence ratio is a measure of the relative amount of fuel to oxidizer, with values greater than 1 indicating more fuel than a perfectly balanced mixture. In general, it has been shown that metal flames can burn stably in fuel rich mixtures with little effect on burning velocity and temperature. However, based on the goal of complete combustion and also common practices in coal combustion, an amount of excess air is selected such that the burner has an overall equivalence ratio of $\phi = 0.9$, which is termed fuel lean. The equivalence ratio is defined as follows:

$$\phi = \frac{\left(\frac{Fuel}{Air}\right)_{actual}}{\left(\frac{Fuel}{Air}\right)_{stoich}} \tag{2.9}$$

With this criteria chosen, the amount of air is calculated by determining the iron stoichiometry as follows. The reaction in question is equation 2.5. Recall that for every mole of O_2 there are 4.76 moles of air since oxygen represents 21% of Earth's atmosphere. Therefore the reaction can be viewed as

$$3Fe + 2\,(4.76\ air) \rightarrow Fe_3O_4 + 7.42N_2 + \text{trace air components} \tag{2.10}$$

Assuming standard conditions for temperature and pressure (273.15 K & 100 kPa), the moles of air in one meter cubed can be calculated according to the ideal gas law.

$$n = \frac{PV}{RT} \tag{2.11}$$

Where n is the number of moles, P the pressure in Pascals, V the volume in meters, R the universal gas constant equal to 8.314 J/mol-K and T the temperature in Kelvin. Using the values mentioned yields 44.03 moles of air per cubic meter. Next, the moles of iron required to keep a stoichiometric ratio with that amount of air is calculated. From equation 2.10, for every three moles of iron there are 9.52 moles of air, therefore this ratio is multiplied by the total moles of air which yields

$$Mol\ Fe\ /m^3\ air = \frac{44.03\ mol\ air}{m^3\ air} \cdot \frac{3\ mol\ Fe}{9.52 mol\ air} = 13.88\ mol\ Fe/m^3\ air \tag{2.12}$$

As before, to convert this to a mass of iron this value is simply multiplied by the molar mass of iron which yields 775 g of iron per cubic meter of air to achieve stoichiometry. However, the desired equivalence ratio is 0.9. To achieve this, more air (or less iron per cubic meter) is needed and that is calculated according to equation 2.9. Using the values of $\phi = 0.9$ and $775\,\mathrm{g/m^3}$ yields $697.5\,\mathrm{g_{Fe}/m^3_{air}}$. With the required iron mass flow rate of 1.5 g/s this means that $2.15 \times 10^{-3}\,\mathrm{m^3/s}$ or 130 L/min of air is required. However, to accomplish the stratified burner concept, the central flow of iron and air must be richer. For this reason, the equivalence ratio of the central flow is chosen to be $\phi = 3$. Doing the same calculation as above, but with this new value yields an air flow rate of or 38.7 L/min. The difference between this value and the total air flow, 91.3 L/min, is the air available for the swirl flow.

Section 2.1.2 discussed swirl generation and the concept of the swirl number. In practice, it

is hard to collect the measurements required to calculate the swirl. Moreover, it is useful to know what the swirl will be during the design process, without having to fabricate the device and test it. For that reason, the geometric swirl number is developed and is calculated using the input velocity distributions in the swirl generator and the geometric parameters of the design, rather than the velocity distribution in the jet. For radial vane swirlers, the angular momentum can be expressed as follows

$$G_\theta = \sigma \frac{\dot{M}^2}{\rho 2\pi B} \tag{2.13}$$

where $\dot{M}$ is the mass flow rate, B is the axial height of the channels and σ is the ratio of the average tangential radial velocity components at the swirler exit inner radius. σ depends only on the geometric dimensions of the guide vanes in the axis perpendicular to the cross section. For a movable block swirler, σ was shown to be well represented by [61]

$$\sigma = \frac{2\pi}{z\xi_m} \sin\alpha \, \frac{\cos\alpha[1 + \tan\alpha \tan(\xi/2)](\xi/\xi_m)}{1 - [1 - \cos\alpha\,(1 + \tan\alpha \tan(\xi/2))]\,(\xi/\xi_m)} \tag{2.14}$$

where ξ is the angle of adjustment of the swirler that varies between zero and a maximum of ξ_m, z is the number of blocks and α the angle of the block and the centerline. These parameters are more clearly seen in Figure 14. It also shows the theoretical curve of equation 2.14 for various flow rates. There is good agreement between the curve and the measured values, and it also shows how the swirl is independent of flow rate. Note that larger values of ξ/ξ_m indicate higher values of swirl since ξ is the amount of opening of the tangential air passages.

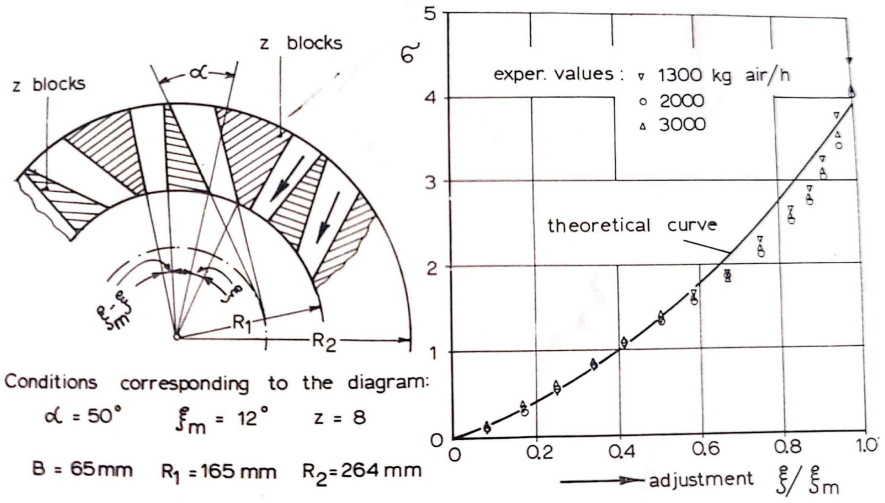

Figure 14: Movable block swirler parameters. Source: Adapted from [49]

For a given value of σ, the swirl number of the flow through a cylindrical or annular duct attached to a movable block swirler depends on the inner and outer radii of the duct, R_i & R_o respectively. This can be combined with equation 2.4 and 2.14 to give

$$S = \frac{G_\theta}{RG_x} = \sigma \frac{R_o}{2B} \left[1 - \left(\frac{R_i}{R_o} \right)^2 \right] \tag{2.15}$$

For this burner, the top plate is the movable one and the lower plate the fixed one. The lower swirl block is fixed to the secondary air pipe with set screws and the connection is kept air tight by a radial o-ring seal. The upper swirl block is secured to the top face of the tertiary air plenum, the outline of which is shown in Figure 15. The top block has slots milled out where bolts are secured, in order to allow for rotation. Again an o'ring is used to seal the top block of the swirler to the tertiary air plenum.

Another factor that improves the strength of the recirculation zone is the addition of a divergent nozzle extension at the outlet of the burner. From experiments [62], the optimum half angle of the divergence of the quarl is 35° and a length of one to two times the nozzle throat diameter.

The combustion chamber also plays an important role in the stabilization of the flame. The combustion chamber ensures that only the air provided to the burner is able to react with the iron, and not ambient air from the surroundings. This avoids excess air entrainment from the surroundings because of the rapid expansion of the jet. In this way, it is possible to control the equivalence ratio and the flame temperature. The combustion chamber also helps guide the particles into cyclone collection system by constraining the flame and leading directly into ducting. One of the goals is to collect all the burnt particles to recycle them, so it is essential that they be properly exhausted from the burner. The difference between the open flame and the flame within the combustion chamber is shown in the testing section. The combustion chamber is chosen such that there is sufficient room for the jet to expand, but not so large that the flow loses its momentum and cannot be guided into the cyclone ducting. In addition, since this is a completely new design and experimental setup, optical access is critical to evaluate, understand and adjust what is going on in the burner. For that reason, a thick-walled fused quartz cylinder is chosen as the combustion chamber. Fused quartz is fully transparent in the visible spectrum and has high temperature resistance with a melting point of 1700 °C. They are also readily available in various sizes from suppliers. The use of a fused quartz tube removes the need for complicated steel pipes with sealed viewing windows, which can be added later on once the design is refined.

Supplying the required air flows and ensuring that they are kept separate throughout the burner is an important task. In order to do this, as well as mount the burner to a frame, all the components are designed to connect to a base plate. The base plate allows the separate flows to be fed easily from the bottom, as well ensuring good air seals between chambers. In addition, it is not desirable to have permanent connections such as welds because of the need for assembly and disassembly. The first connection, that of the central iron air flow pipe, is made by modifying off-the-shelf fittings available from Swagelok. The Swalelok fitting allows for an airtight seal on a rigid tube with the use of two ferrules that are compressed when the nut is tightened. The other side of the fitting is a standard NPT thread. The fitting is modified by drilling a clearance hole through the center to allow the solid pipe to pass completely through the fitting. It is then held in place with the base plate by the NPT threads, which also provide the air seal between the plate and the pipe. The advantage is that the pipe is easily removable from the fitting and that the height of the pipe above the base plate can be altered by moving the location of the ferrules.

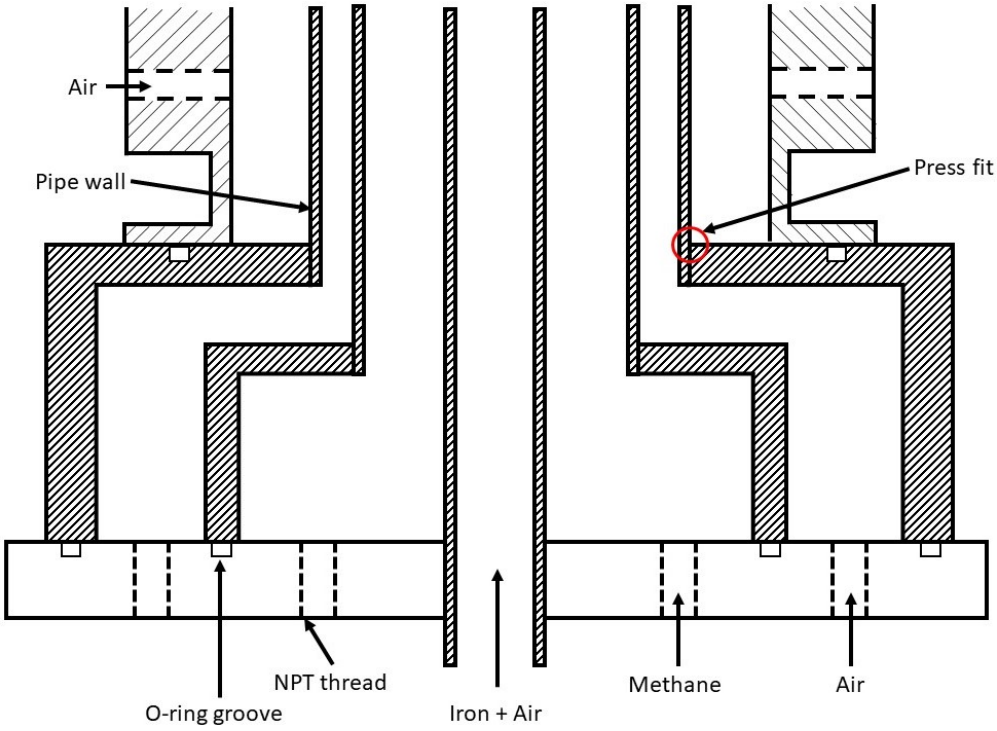

Figure 15: Base plate air and methane connections.

The concentric flows of methane and air are delivered by using chamber assemblies that fit over the respective inner pipes and connect to the base plate. This is shown more clearly in Figure 15. The purpose designed chambers act like plenums, which allow air to be fed in from the base

plate and then distributed into the pipe towards the burner outlet. The pipe is press fit into the chamber to create an airtight seal. The chamber is secured to the base plate with screws and an o-ring provides the air seal. The second chamber fits over the first one and is secured in the same manner, with significant space between the two to allow space for the fittings in the base plate. The tertiary air for the swirl is not provided in the same way because of practical material constraints. The material to make a third chamber large enough to fit over the second one is difficult to procure and unnecessarily expensive. The plenum for the tertiary is fixed on top of the second chamber and is secured with screws. The air is fed from radial air entry ports. Again an o-ring provides the air seal between the two pieces.

2.7 Dispersion System

A reliable dispersion system that can operate for long durations (over 10 minutes) is essential to the operation of the iron powder burner. The current system used by the AFL burners is comprised of a piston-cylinder that is filled with powder and connected to an actuator, which then pushes the powder at a set rate towards an air knife which takes a layer of powder off the top and pushes it into the flow. However, the duration of this dispersion technique is limited by the size of the piston-cylinder because that determines the total quantity of powder available. That design cannot be used for the turbulent iron burner since run times of several minutes are expected.

Making a steady dispersion system for powdered solids that can disperse large quantities of powder for long durations is extremely complicated and could be its own masters project. For that reason, a purpose built dispersion unit was purchased from a German company (Powder and Surface GmbH) that specializes in powder dispersion. The dispersion system operates by using small chambers called dosing cells, that can hold a fixed volume of powder and a series of pneumatic valves to control the flow of powder and air entering and leaving the cells. The concept is shown schematically in Figure 16. The machine is supplied with pressurized air, which runs the pneumatic valves as well as provides the air flow for the powder. There is also a vacuum pump that pulls the powder into the dosing cells. The sequence begins with the red valves shut and the blue ones open, which allows the vacuum pump to pull powder into the cell. Then the blue valves are shut and the red ones open, which lets in pressurized air to carry the powder out of the cell towards the process.

By adjusting the duration of the valves opening/closing as well as the strength of the vacuum, the amount of powder brought into the cell can be varied. The powder feed gas can be adjusted to control the velocity and total air flow of the gas carrying the powder. By using two (or more)

cells, a smooth powder distribution can be achieved, as shown in Figure 17. By placing the two cells 180° out of phase, such that one is pulling in powder while the other is pushing out powder, a steady feed rate can be achieved. Adding more cells can help create a more stable distribution, similar to an engine with more pistons. The dispersion system is equipped with a large drum that is mounted on a motor that allows it to rotate. The size of the drum is variable and can hold several kilograms of iron powder, thus allowing long duration run times. The rotation of the drum ensures that the powder does not get packed over time and can easily be aspirated by the system. The lid of the drum is spring loaded such that it acts as a pressure relief valve in the case of over pressure.

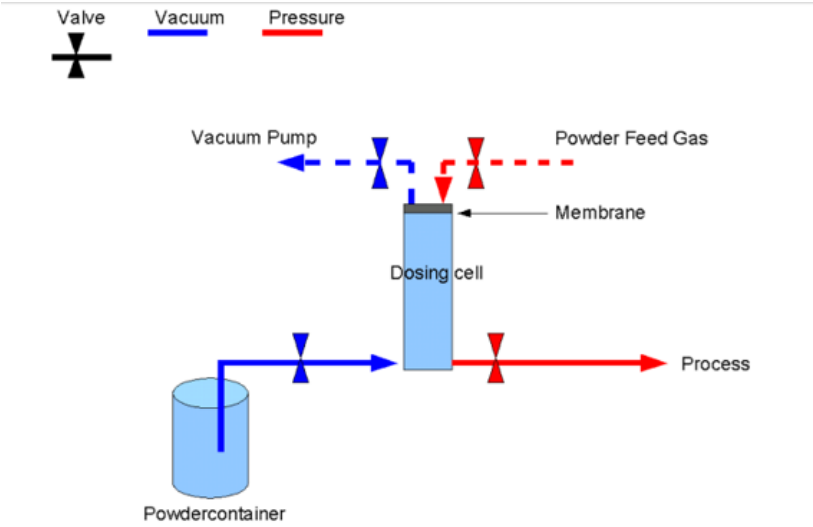

Figure 16: Dispersion system operating principle. Source: Powder and Surface GmbH

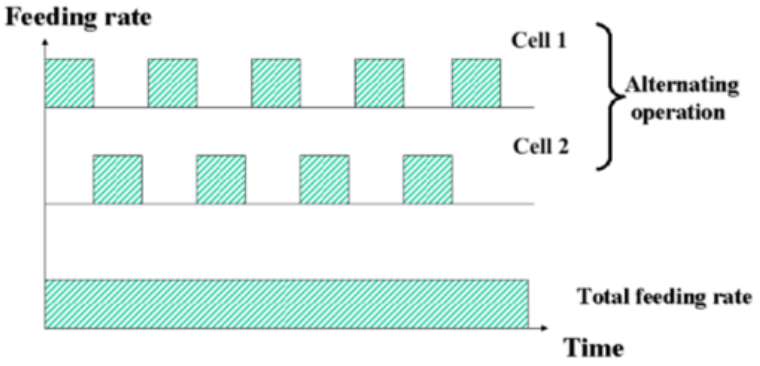

Figure 17: Dispersion system even distribution. Source: Powder and Surface GmbH

2.8 Flow control

The gas flows to the burner are controlled through the use of mass flow controllers (MFCs). The MFCs are from Brooks Instrument and operate based on the principle of hot wire anemometry. They are connected to a computer via the Brooks Smart DDE (Dynamic Data Exchange) software and operated by an in-house LabVIEW program. The mass flow controllers allow a high degree of accuracy and the equivalence ratio for the ignition flame can be selected within the program. In total, a 5 standard liter per minute (SLPM), a 20 SLPM, a 40 SLPM and a 300 SLPM MFC are used to supply the necessary flows.

2.9 Safety Considerations

As with any combustion system, there are many potential risks and it is important to build in safety mechanisms to protect all users. The most important thing is to be able to extinguish the flame in case of emergency. To that end, all gas lines are equipped with solenoid valves before entering the burner so that they can immediately be shut off with the flip of a switch. In general, the protocol for extinguishing gas flames is to cut the supply of fuel and keep the oxidizer flowing. However, since there is powder involved, cutting the fuel means that the carrier flow also stops and there will be powder left in the lines of the burner. To mitigate this problem and add an additional layer of safety, every channel of the burner (primary iron and air, methane, secondary air and tertiary air) is connected to a nitrogen purge line. This line is connected directly to a pressurized nitrogen cylinder and separated from the burner by a solenoid valve, such that activating the valve releases a high flow nitrogen jet throughout the burner. Adding nitrogen to flush the burner instead of air ensures that combustion will be extinguished since it is inert. In addition, as mentioned in section 2.4, the burner is also fitted with pressure relief valves in the base plate in case of pressure build up from the methane flame. Lastly, as with all experimental apparatus, a protective enclosure is built around the burner. The enclosure consists of an aluminum extrusion frame with quarter inch thick clear polycarbonate panel walls and a hinged door also made of clear polycarbonate. The lower section of the enclosure is made of perforated steel sheets to allow air flow into the enclosure and the top is connected to a cyclone for exhausting and filtration. As an extra precaution, additional Type D fire extinguishers specifically for metal fires were purchased and stationed near the burner.

3 Burner Manufacture

3.1 Material Selection

The materials chosen for the burner are selected based on their function, machinability, cost and availability. From literature as well as previous experiments within the AFL, the temperature of iron flames has been measured to be roughly 2300 K [63]. Since the flame is expected to sit at or near the nozzle of the burner, all components in this section must have high heat resistance. In addition, the ignition methane flame will also sit inside the burner nozzle. For this reason, the quarl, central iron air pipe and the secondary air pipe are made of of stainless steel. 304 stainless steel is selected over 316 stainless steel because of its machinability. All the other parts of the burner are made from aluminum because of its machinability and cost. Using aluminum allows for easier and faster machining than steel. Large diameter aluminum bars are readily available from local suppliers and can be purchased at custom lengths.

3.2 Machining

The machining is carried out at the McGill Faculty of Engineering Workshop by professional machinists. The equipment at their disposal includes lathes, manual and semi-CNC mills and CNC machines (3, 4 & 5 axis). As most of the pieces are circular and symmetric around the center axis, the lathe will be the main tool used for machining. With this in mind, the pieces are designed so as to be easily made on a lathe. Only three pieces have complex geometries and small features requiring CNC machining, which is more costly and time consuming. The pieces in question are the two blocks of the swirler, which require precise geometries, small passages and must interlock accurately. The last piece is a centering ring called a spider plug, which helps to keep the central iron and air pipe concentric with its surrounding pipe and also holds down the beads of the ignition flame. As mentioned before, o-ring are used to create airtight seals between the various flow regions. This allows for easy assembly and disassembly of the burner, which is essential as it will need to be cleaned periodically. The o-rings grooves and seals are sized according to design guidelines for SAE AS568 o-rings. The assembly is held together my machine screws that also ensure adequate compression to create a tight seal.

3.3 Pieces & Assembly

To get a better understanding of the geometry and how the parts work some of the machined parts are shown here. In addition, the assembled burner is shown with the main components labelled.

Figure 18 shows the two pieces of the movable block swirler. The lower piece has slots that allow it to rotate with respect to the other piece and a large surface area between the slots and the vanes where it seals against an o-ring. The angles of the vanes can clearly be seen, with one face cut radially inwards while the other is set at a tangential angle. The top block's vanes have the opposite configuration so that they can mesh and create either radial or tangential channels. Recall that the radial channels do not produce any swirling effect whereas the tangential ones do. By adjusting the angle as seen in the left side photos, the amount of swirl can be selected. Also visible upon close inspection is the radial o-ring groove on the inside of the upper swirl block.

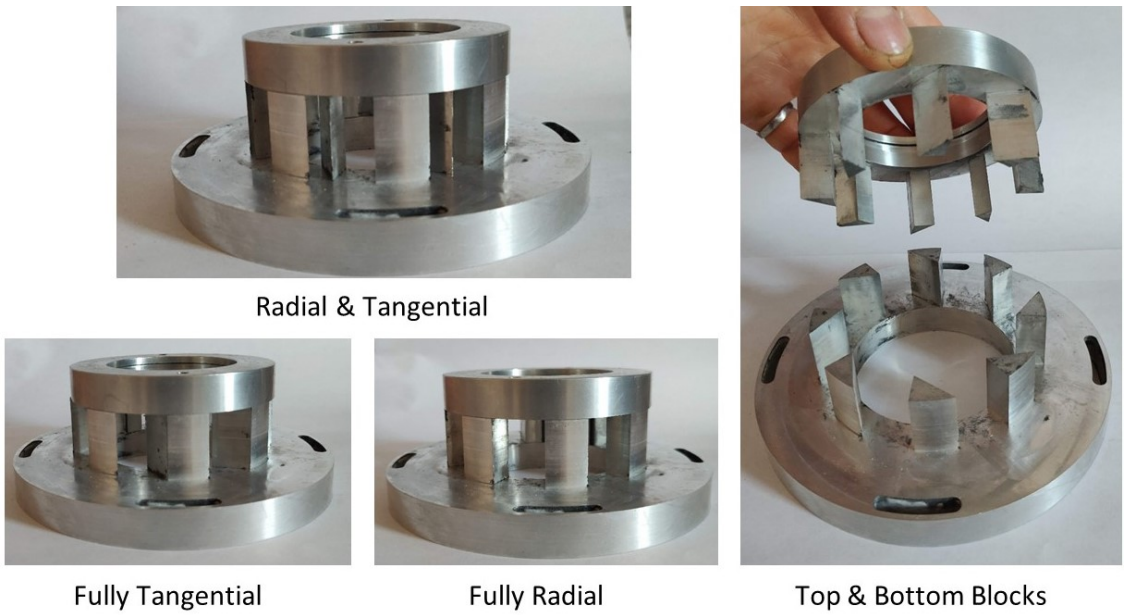

Figure 18: Machined movable block swirler.

Figure 19 shows the assembled burner with different views as well as connected to the whole system. The top view shows the several concentric annular regions and the spider plug which helps to center the central pipe. Its shape is such that it provides minimal resistance to the flow, while still being rigid and providing a surface for the metal screen to be fixed to. Also visible from the top view is the spark igniter. The white tube is a hollow ceramic tube, which houses one of the sparker electrodes to shield it from the flame and to electrically isolate it from the body of the burner. The other electrode is connected directly to the body of the burner, such that the spark is

formed between the end of the ceramic tube and the central pipe, which is directly in the path of the methane and air flow. For safety reasons, the iron air mixture is fed horizontally to the burner through a Tee, with additional carrier air coming from the bottom of the Tee. This is done in case burning powder falls back into the central tube, so that it cannot create a flashback event all the way to the powder dispersion system.

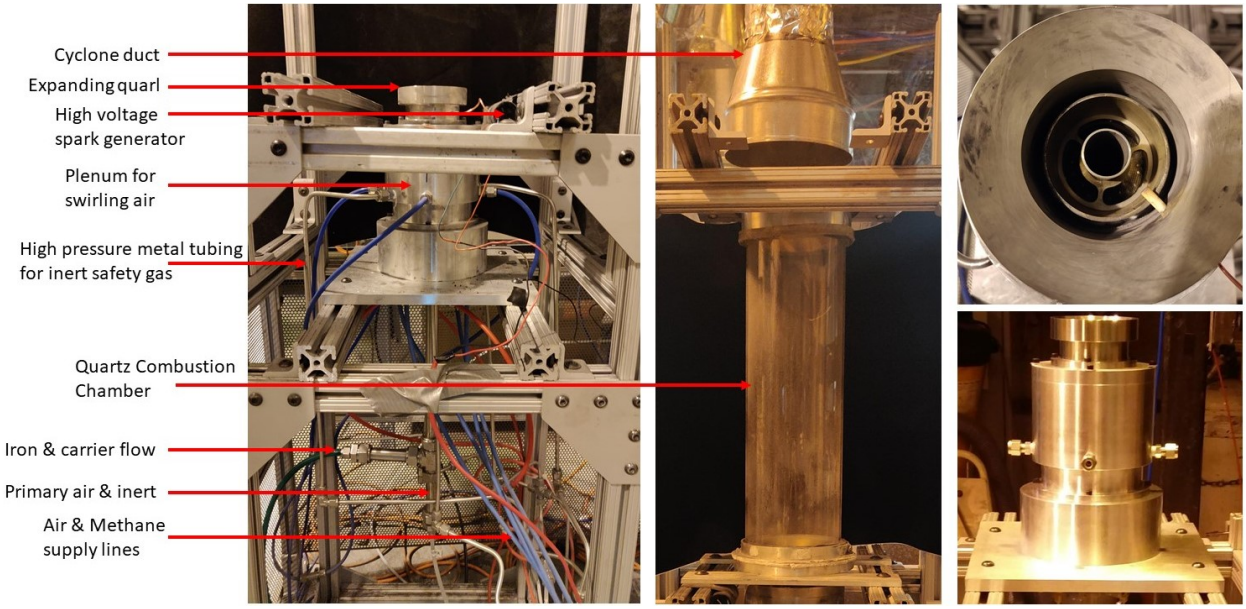

Figure 19: Assembled burner with main components labelled.

4 Burner Testing

The testing of the burner comprises three phases. The first is general systems testing, including the dispersion system, the control of the MFCs and solenoids, the inert gas safety lines, the ignition flame and checking for leaks or other miscellaneous problems. The second phase is cold flow testing, which involves dispersing powder into the burner, observing the swirling flow pattern and ensuring particle collection into the cyclone system. The last phase is testing of the entire system with an ignited iron flame as well as tuning of the burner parameters.

4.1 General System Testing

The burner is a new system with several different sub-systems that must work in unison. For this reason, each part will be tested separately before being combined. The dispersion system with the main components labelled is shown in Figure 20. The dispersion system allows for many parameters to be adjusted, the most important of which are the strength of the vacuum and the pressure of the carrier flow gas. These parameters, especially the vacuum determine how much powder is dispersed. The stronger the vacuum, the more powder is drawn into the dosing cell, thus a higher feed rate. However, the system does not have a weighing mechanism, and therefore does not provide the mass flow rate of powder being dispersed. Therefore, the dispersion system has to be tested to establish the mass flow rate for various vacuum and carrier gas pressure settings. The method used is simple and gives a good indication of the average mass flow rate. A bucket with a tight fitting lid has two holes drilled into it. One accommodates the powder dispersion line and the other has filter placed over it to prevent pressure building up and powder escaping. The bucket is then placed on a scale and weighed before any powder is dispersed. The powder is dispersed for 3 minutes with the chosen settings and the mass of the bucket is monitored. The difference between final and initial mass of the bucket is then used to determine the average mass flow rate of powder dispersed. The process is repeated for each of the settings on the dispersion system. Each time a new set of parameters is chosen, this test is repeated to know what the current mass flow rate is. In addition to this, the evenness of the distribution is assessed qualitatively by dispersing the powder into the ducting of the cyclone collection system and visually monitoring fluctuations in the powder dispersion. This can be seen in Figure 21, where the powder exits the dispersion tube and enters the cyclone, traversing the gap in between. This allows the relative strength of the dispersion to be assessed and any significant fluctuations in the dispersion, which do occur.

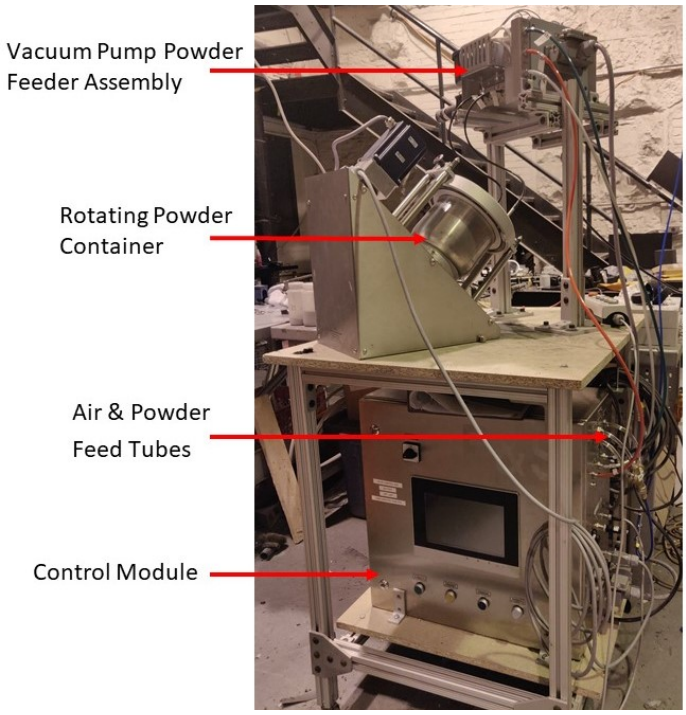

Figure 20: Dispersion system with main components labelled.

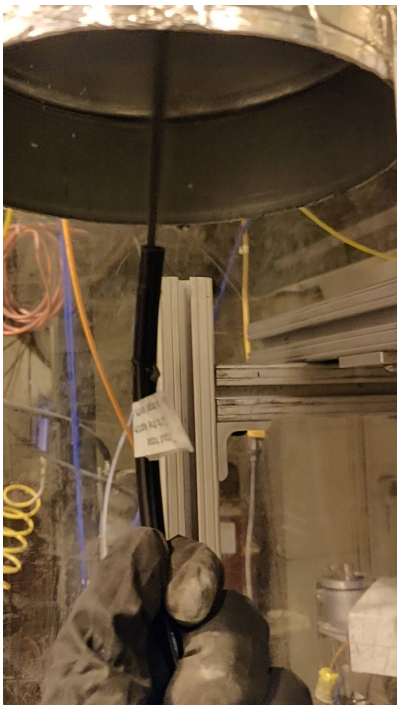

Figure 21: Visual of powder dispersion.

The gas flows to the burner are provided by MFCs, which are placed on a central control panel. From the control panel, flexible tubing is run to the burner enclosure where each line is connected to a solenoid valve before proceeding to the burner. The solenoid valves are normally closed, and wired to switches on the burner control box, which is located next to the operator where the dispersion system control and the laptop are also kept. As stated before, the MFCs are controlled via an in-house LabVIEW program. Each flow, the primary air, methane, secondary air and tertiary air are tested separately and then in unison to see if their respective set points can be achieved with the available air supply. The latter is a concern considering the high airflow and the use of standard 1/4 inch tubing, as well as pressure limitations on the MFCs and air supply. The LabVIEW program also allows two MFCs to be paired and the equivalence ratio between them chosen, so that it is simple to create a stoichiometric methane air mixture for the ignition flame. All MFCs were able to achieve the required flow and the methane ignition flame was successfully stabilized, as seen in Figure 22.

Lastly, the inert line is connected from the burner directly to a pressurized cylinder with high pressure tubing and a solenoid with a maximum pressure of 450 psi. The control process of the flows is shown in Figure 23. The higher pressure set up allows a strong blast of inert gas to

immediately blow through the whole burner. The inert line connects to the central air and iron pipe, the methane pipe and the tertiary swirling air plenum to ensure all oxidizer can be displaced and the flame gets quenched. The inert emergency stop was tested with the ignition flame and successfully blows it out. It was also tested with inert powder (alumina and silicon carbide) in the central pipe to see if it can successfully exhaust it from the burner, which it was able to do.

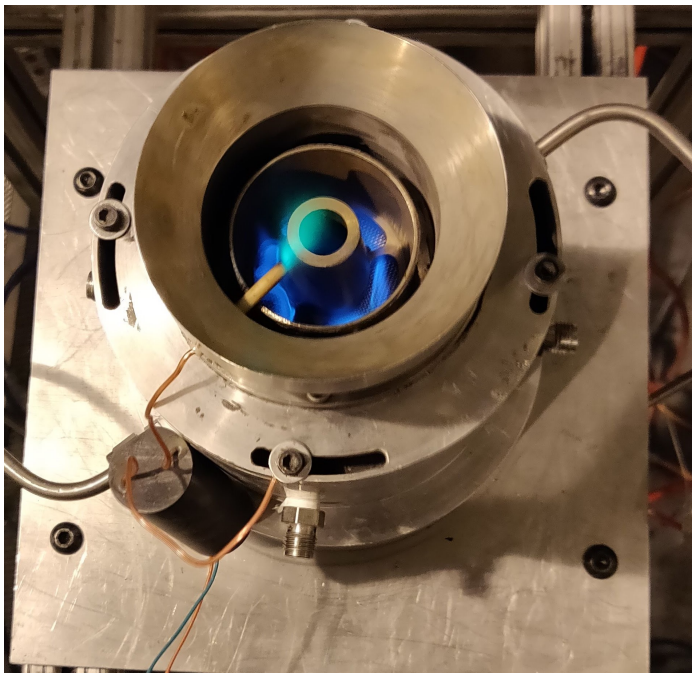

Figure 22: Iron ignition flame.

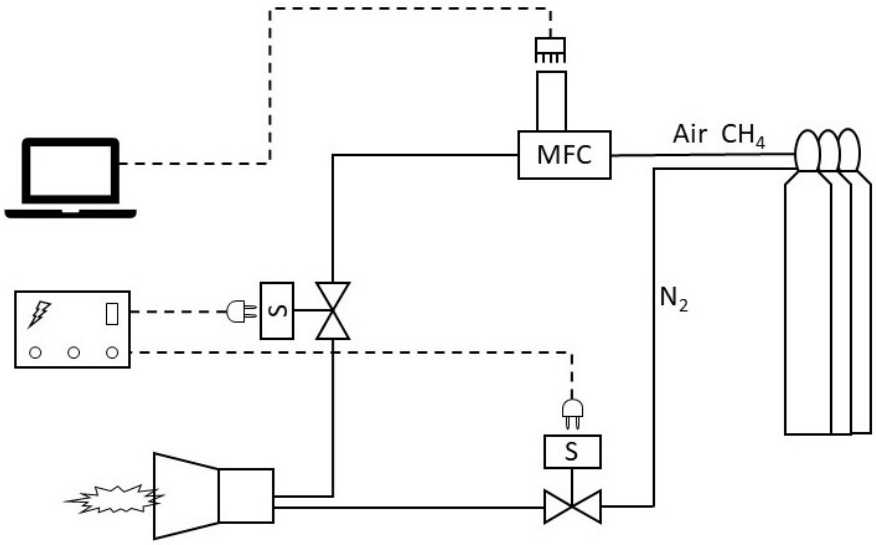

Figure 23: Flow control process diagram

4.2 Cold Flow Testing

Cold flow testing is important to ensure that the movable block swirler is operating as designed and creating a recirculation zone. In addition, it is needed to see if there is enough flow for the particles reach the cyclone ducting and to determine the length of the combustion chamber. Preliminary testing is done with similar sized spherical alumina particles and non-spherical silicon carbide, both of which are less dense than iron. These trials are followed by testing the actual powder used for the experiment. The powder in question is sponge iron with a mean diameter of roughly 20 microns, which is provided by Tata Steel Ltd. A side by side photo of the iron powder dispersion with and without the tertiary swirling flow is shown in Figure 24.

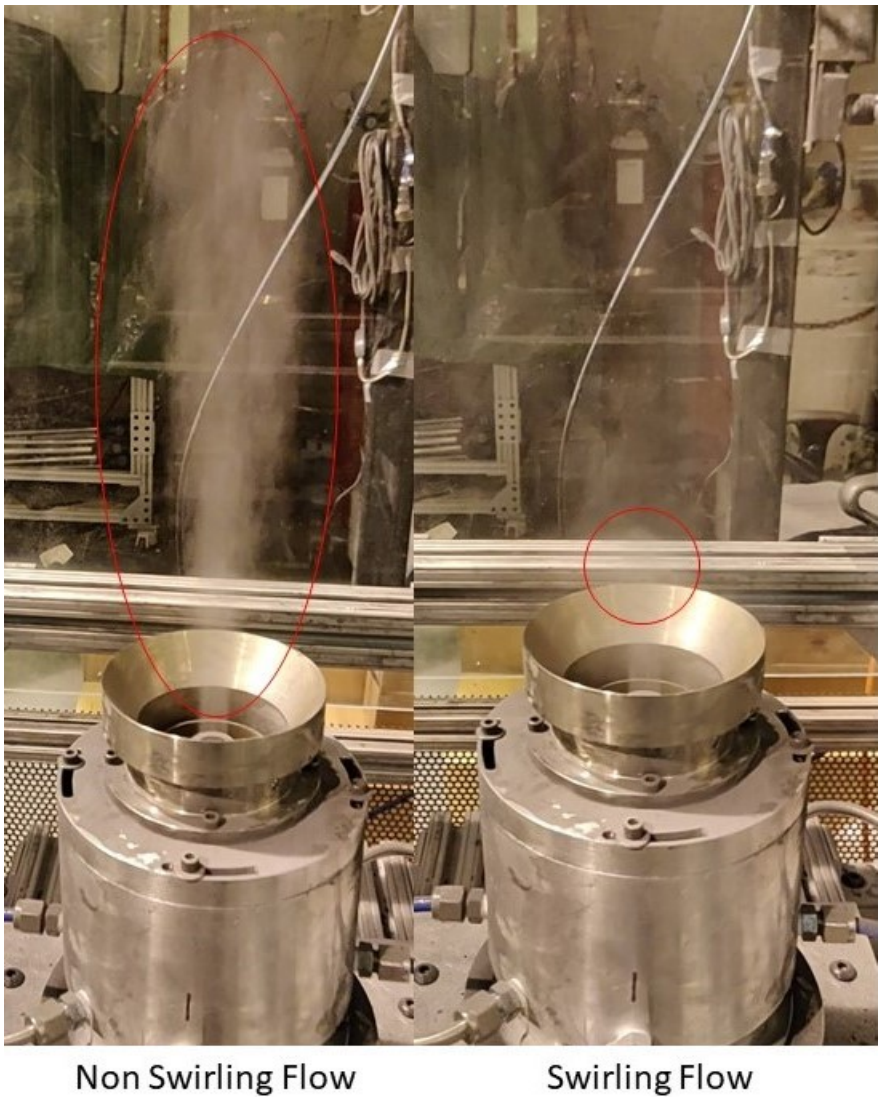

Figure 24: Iron powder flow with and without swirl.

The left pane of the figure shows the powder dispersion without any swirling air. A long vertical expanding jet of powder is clearly seen traveling upwards. The height of the jet is roughly twenty inches. The jet is steady and few particles fall to the side. However this changes once the swirling air is introduced, as seen on the right pane of the figure. There is no longer a vertical jet, and upon close inspection of the highlighted zone in red, a recirculation zone can be seen. The recirculation zone is more clearly seen in videos of this phenomena, but the difference between the two cases is clear. The recirculation zone is established roughly three inches above the nozzle of the burner. The powder remains concentrated in this zone and the particles exit from the sides and travel upwards similar to what was shown earlier in Figure 7. It is important to note that the particles continue their trajectory upwards and do not fall to the sides and back down towards the burner. This is essential to be able to effectively capture all the particles for future recycling. This is a successful first test and demonstrates the ability of the movable block swirler to generate adequate swirl to create vortex breakdown. This is key in the strategy to stabilize the iron flame, since the central recirculation zone creates a low velocity region where mixing can happen and heat from burning particles can be transferred to incoming particles.

4.3 Iron Flame Testing

The final step is hot flow testing: testing the burner system with an active flame. This process is done in two stages, the first with a continuous methane flame to ensure flame stability and observe the flame characteristics and the second with the methane flame turned off after ignition. Some preliminary testing was done without the combustion chamber. As can be seen from Figure 25, the unconstrained iron flame jet is quite tall and expands from the outlet of the burner. The height of the flame is roughly three feet. The addition of the quartz combustion chamber and adjusting the iron flow rate and swirling air resulted in a stabilized self-sustained pure iron flame. This is the first ever such flame and is a major accomplishment and milestone in this project. Pictures of the stabilized flame are shown in Figure 26 and Figure 27. Compared to the open flame, it is shorter and displays less turbulence or vortexes in the upper regions, but significantly increased swirl in the bottom section.

Figure 25: Iron Flame Without Combustion Chamber

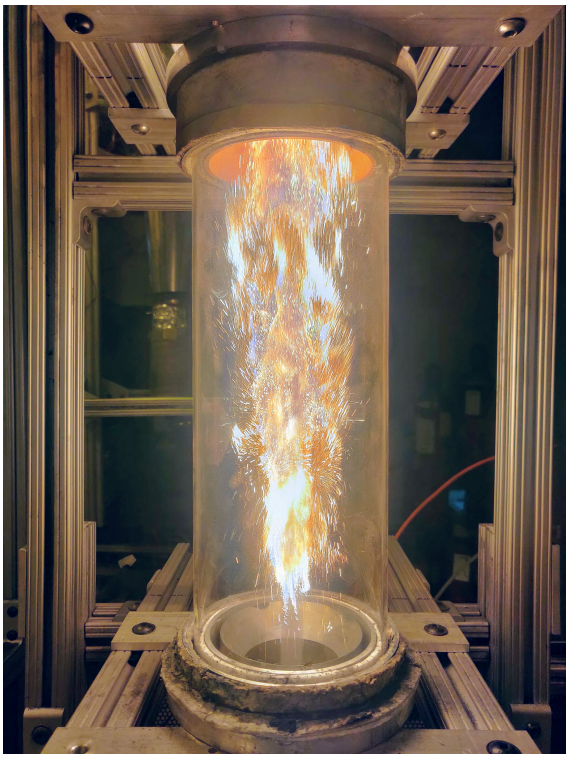

Figure 26: Stabilized Pure Iron Flame

Figure 28 shows the comparison between the iron flame during ignition with the presence of the methane flame and after once the methane flame is extinguished. In the left panel of the figure, the presence of the methane flame can be noted from the fact that the iron burns immediately as it exits from the nozzle. In addition, this region of the flame is darker in color, a mix of orange and red, which is likely due to some of the oxygen reacting with the methane meaning there is not enough to react with all the iron. This is to be expected, since the point of the stratified burner is to have a fuel rich central core, which then mixes with air. However, on the right panel where the methane flame is extinguished, the iron only ignites once it reaches the flame zone. The unburnt powder can clearly be seen coming from the central tube before igniting. It is this clear division between incoming unburnt iron powder and bright burning powder that makes the flame stabilization zone easily identifiable. The flame stabilizes roughly 3 inches above the burner nozzle. As can be recalled from Figure 24, that is where the recirculation zone is formed by the swirling flow. This means that the swirling flow is carrying out its intended purpose of stabilizing the iron flame.

Figure 27: Stabilized Pure Iron Flame Entering Cyclone Ducting

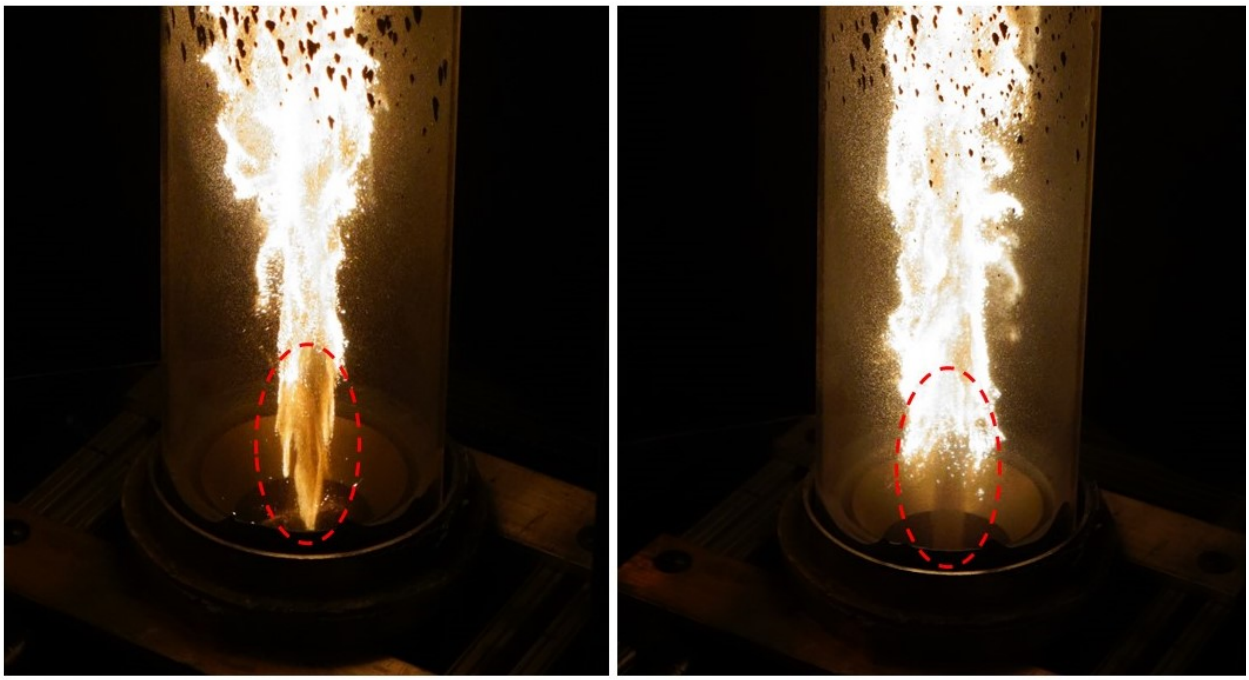

Figure 28: Iron Flame During and After Ignition

4.4 Performance

The pure iron flame was stabilized for over twenty minutes, demonstrating its feasibility and potential as a new energy carrier. The limiting factor in the duration of the flame became the size of the dispersion system, which has a 3 L powder container that requires a minimum amount of fill to operate properly. In general, the flame is able to respond to small disturbances or changes in the flow, with the flame anchoring zone moving up or down roughly one centimeter. However, several factors play a role in the stability of the flame, and the flame has varying levels of sensitivity to each. The most critical factor is the uniformity of the powder dispersion and carrier flow. In the event of large changes in the dispersion, either a rapid momentary drop in powder dispersion density or sudden gust of air, the flame can be blown off. In both cases, the blow off is caused because the flame speed is no longer fast enough to match the incoming flow rate of air. In the event of a blow off, the flame needs to be reignited, which can be complicated by powder blocking the ignition mechanism. In this case, the system needs to be cleaned before the flame can be reignited. Another element that plays a role in the stability of the flame is the quantity of powder dispersed. As discussed, a fuel rich flame will be more stable since it can negate the effects of momentary dips in powder concentration. However, this comes at the cost of excess powder falling

to the walls of the combustion chamber since the carrier and recirculation flow cannot support such a high loading. The powder accumulation does not significantly affect the flame, but can be a factor when considering a long operation of the burner for several hours. This can be mitigated with either a shielding flow to pick up the excess powder and carry it to the outlet, or a mechanism that allows cleaning of the base of the combustion chamber. The excess powder can also lead to ignition of the fresh iron powder at the nozzle, as hot particles fall back towards the inlet. This can lead to clogging if particles ignite and agglomerate on the nozzle, which would cause the flame to extinguish. This is mitigated through the use of a thin edged nozzle at the outlet of the burner.

The length of the combustion chamber is also a key parameter since it needs to be long enough to allow stratified combustion, but not too long such that the burnt particles cannot enter the cyclone. Several different lengths of combustion chambers were tested and the flow into the cyclone accordingly adjusted. The current burner has a small gap between the outlet of the combustion chamber and the inlet of the cyclone ducting, so that there is no suction on the flame caused by the cyclone. The cyclone is fan driven and operates on negative pressure, so that it pulls in particles from the surrounding environment. The velocity of the burning powder is such that all the powder exiting the burner is easily entrained into the cyclone, as can be seen in Figure 27. The inlet of the cyclone duct is wider than the combustion chamber, so that if any powders were to fall to the sides, they would be picked up by cyclone flow.

All components of the burner were able to sustain the heat of long duration flames, indicating the choice of materials was appropriate. The advantage of the flame anchoring several inches above the burner nozzle is that the burner itself is subjected to a lower heat load. The fused quartz combustion chamber provided a clear view of the flame at all times and its smooth surface minimized any particle sintering or sticking. In addition, its optical clarity in the $0.7\,\mu$m to $3.5\,\mu$m part of the infrared spectrum helps it withstand the heat, as it allows much of the thermal radiation to pass through. If the temperature of the particles in the combustion chamber fall between the adiabatic flame temperature (2250 K) and a lower bound at the exit where they are coolest of 1000 K based on their color, between 38% and 83% of the emitted radiance will pass through the quartz chamber. The burner was also able to stabilize flames with two different iron powders, with different mean particle sizes and particle shapes. In addition to the iron powder provided by Tata Steel Ltd. as part of the strategic partnership grant, pure iron powder was purchased from TLS Technik Specialpulver (now Eckart TLS), which is a leading international specialist in the production of high-quality metal powders for industrial 3D printing. The powder from TLS

Technik is produced using Electrode Induction-melting Gas Atomization (EIGA) which yields fine, pure powders, with a spherical shape, free of ceramic impurities and with low oxygen contents [64]. The powder from Tata Steel is produced using a direct reduction process with hydrogen on iron ore, which yields pure sponge iron that has a high internal porosity. This demonstrates the burner's range of particle morphology it can stabilize, as well as a first step towards determining the range of particle sizes it can handle.

The success of the turbulent burner in stabilizing a pure self-sustained iron flame for long durations marks the completion of the first major goal of the masters work. Indeed, the stability of the iron flame allows for the testing of several parameters of interest, such as the particle temperature and heat transfer properties of the flame, which was carried out during the course of this work. In addition, the long duration flame coupled with an efficient particle collection system allows for the analysis of the combustion products. These tests and the conclusions drawn from them make up the subsequent sections of the thesis.

5 Heat Transfer and Combustion Efficiency

5.1 Background

One of the main goals of the turbulent iron burner is to demonstrate that metals can provide power. To accomplish this, heat must be extracted from the flame. However, since it is a two phase flow, the end use device or heat exchanger cannot be placed directly into the flow since the powder will deposit on it and could cause damage. In addition, this would interfere with particle collection and recycling. Therefore, an appropriate understanding of the heat transfer mechanisms at play is required in order to design efficient heat extraction systems. To that end, the three different modes of heat transfer are evaluated; namely conduction, convection and radiation. Since the post reaction zone consists of both hot gases and hot particles, the different heat transfer mechanisms will play varying roles. The burning iron/iron-oxide are solid particles, and thus emit solid body thermal radiation. This is unlike gases, where the only radiation emitted is from soot. Because of the high temperature of the burning particles, 2250 K in theory, radiation will be an important factor since the radiant energy flux scales to the fourth power of temperature, according to the Stefan-Boltzmann equation. With this in mind, it is essential to extract as much energy as possible from the particles before they begin to cool. The actual temperature of the particles in the turbulent iron flame will be assessed, to help determine the heat transfer possibilities. The hot gas on the other hand will be more affected by convection with surfaces. There are two mediums for the air to exchange heat with, the combustion chamber walls and the particles themselves. There is also the possibility to retain the heat in the gas, such that after removing the particles in the cyclone the clean hot gas can directly be used in a power generation process.

Analysis of the products of combustion can give far ranging information from the burner's combustion efficiency to reactions taking place within the flame. The combustion efficiency is an extremely important parameter for any power generation system, since it is essential in sizing the fuel feed rate. Given a desired power output, the actual heat release of the fuel must be known in order provide adequate power. Since iron has several oxides, the actual heat release from the burner depends on which oxide or oxides are formed. The combustion efficiency can be evaluated by the amount of unburnt iron left in the sample. These parameters are measured with several different diagnostic techniques available within the McGill Engineering facilities. The product morphology can also give insight into the combustion process and efficiency, since the iron flame temperature

is above its melting point and thus the particle shape can change. In addition, the size of the particles is an important parameter considering the goal is to capture and recycle the powder. As mentioned earlier in section 2.3, one of the reasons behind the stratified burner concept is to ensure there is no formation of nanometric oxides. Therefore, by measuring the particle size before and after combustion, this burner concept can be evaluated as well as the combustion mode of the iron particles, as described in 1.2.

5.2 Methodology

Temperature Measurements

Due to the nature of two phase flow and the high temperatures, a non-intrusive optical diagnostic method is selected to measure the temperature of the particles in the flame. This is determined by measuring the emission spectra of the turbulent iron flame and polychromatic fitting of the continuum spectra to Planck's law. Measurements are carried out with an Ocean Optics USB4000 Fiber Optic Spectrometer. The absolute spectral response is calibrated with a NIST-traceable Ocean Optics LS-1-CAL tungsten halogen calibration lamp. The wavelength is calibrated with an HG-1 Mercury Argon calibration light source. The peaks measured by the spectrometer are compared to the known values provided on the device, and the average wavelength shift is determined. A 50 μm fiber optic cable is used and the spectrometer captures light in the wavelengths from 300 nm to 1100 nm.

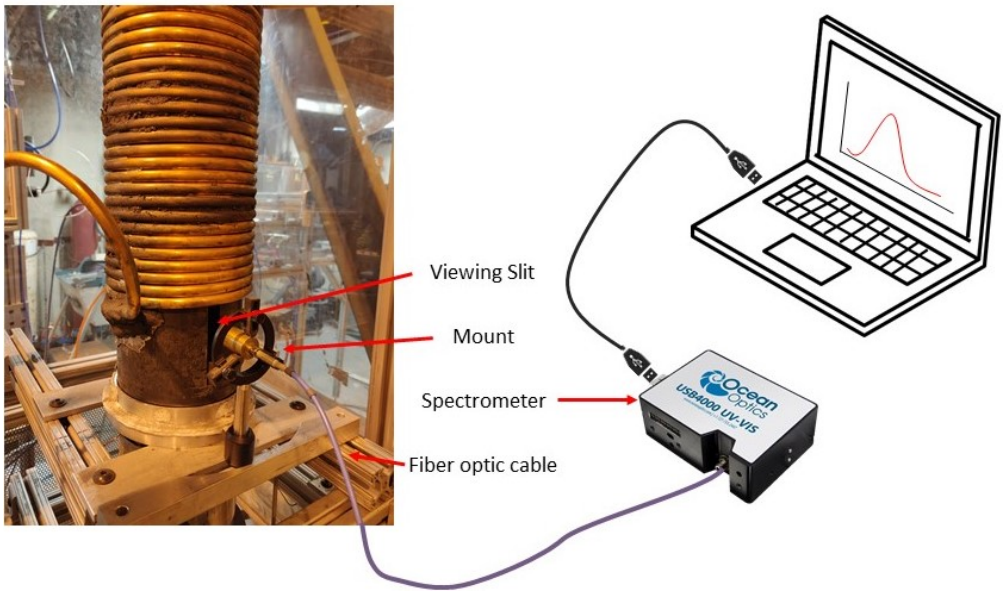

Figure 29: Temperature measurement experimental setup.

The spectrometer is operated through the Ocean View software provided by Ocean Optics, which allows different settings to be adjusted as well as data capture. The end of the fiber optic cable is placed on a support stand at the height of the anchor point of the iron flame, roughly 2 inches from the edge of the combustion chamber. A steel combustion chamber with a half inch wide by 3 inch tall slit milled out of it in the region of the flame anchoring zone is used for measurements. An image of the experimental setup is shown in Figure 29. Once the flame is ignited and stabilized, the Ocean View integration time is adjusted such that the signal from the spectrometer is maximized without being saturated. Spectral data is then collected every 10 seconds over the course the course of 5 minutes.

Polychromatic fitting is applied in the region of 400 nm to 700 nm to the continuum spectra of the flame. The dependence of light intensity $i_{\lambda,T}$ on wavelength and temperature emitted by a condensed phase emitter, such as a solid or liquid, is described by Wien's approximation as follows:

$$ln\left(\frac{i_{\lambda,T}\cdot\lambda^5}{\epsilon(\lambda,T)}\cdot 2\pi\cdot C_1\right)=\frac{C_2}{\lambda T} \tag{5.1}$$

where $\epsilon(\lambda T)$ is the spectral emissivity of the condensed emitter, $C_1 = 0.5954\cdot 10^{-16}\ W-m^2$ and $C_2 = 1.4388\cdot 10^{-2} m-K$. For grey bodies the spectral emissivity is independent of wavelength, therefore the left-hand side of equation 5.1 is a linear function of $1/\lambda$, with the slope proportional to 1/T. In general, most of the spectra from solid bodies is grey in some narrow range of wavelengths as there are no physical reasons to make sudden jumps like in discrete energy atomic or molecular spectra. Thus, iron oxide can be assumed to be a grey body if the spectra fit the Planck distribution.

The spectral data in the range of interest is scaled to an absolute intensity using the tungsten light data along with a calibration curve provided with the LS-1-CAL according to the following formula

$$I_{absolute} = I_{experimental}\ \text{x}\ \frac{I_{blue\ light\ calibration}}{I_{blue\ light\ data}} \tag{5.2}$$

The resulting data is then plotted according to equation 5.1, with $1/\lambda$ as the x-axis and $ln(i\lambda^5)$ as the y-axis, scaled by the appropriate constants. The slope of this curve is proportional to 1/T, therefore the temperature can easily be extracted.

Heat Transfer Model

A simple model of the heat transfer is made using Matlab, to determine the radiation heat transfer properties of the metal flame. The case evaluated is shown in the sketch of Figure 30. The flame is assumed to have stabilized and the downstream region is the section of interest, indicated by the dashed red box in the figure. The particles and air enter this section at 2080 K and 1800 K respectively, based on the temperature measurements and the equivalence ratio. The combustion chamber walls are kept at a constant temperature of 300 K. From there, the model assumes that there is radiative heat transfer between the hot particles and the pipe walls, and convective heat transfer between the air and both the particles and pipe walls. Since the pipe diameter is fairly large and the length relatively short, the convective heat transfer between the walls and the air is likely to be small, especially compared to the convective heat transfer between the particles and air. This can be seen by looking at the Dittus-Boelter equation for turbulent flow, which was chosen because it applies to turbulent flows in smooth pipes and is relatively simple, which allows for a good approximation for a comparison. The Dittus-Boelter equation is given below.

$$Nu_D = 0.023 Re^{0.8} Pr^n \tag{5.3}$$

where Nu_D is the Nusselt number in the duct, Re is the Reynolds number, Pr is the Prandtl number and in this case n=0.3 since the fluid is being cooled. Taking the case of large Reynolds number, say 10 000 and given that the Prandtl number for air is generally on the order of 1 (or slighly less), this yields a Nusselt number of 36. Given that the thermal conductivity of air is under $0.1\,\mathrm{W/m-K}$ in the temperature range of interest and that the pipe diameter is 0.12 m, this gives a heat transfer coefficient of $30\,\mathrm{W/m^2-K}$. In the case of laminar flow, the Nusselt number tends towards a constant value for long pipes with fully developed flow. From Incropera & DeWitt this value is given as 3.66 for convection with uniform temperature in circular ducts [65]. This value of Nusselt number yields a heat transfer coefficient of $3\,\mathrm{W/m^2-K}$. Since the actual flow in the pipe is turbulent but has a low bulk velocity, and therefore a low Reynolds number, the value of the heat transfer coefficient will be somewhere between the two.

On the other hand, the small particles have a large surface area and are expected to mix well with the air. Indeed, for a sphere in a flow, the Nusselt number proposed by Whitaker is

$$Nu = \frac{hD}{k_{fluid}} = 2 + \left[0.4 Re^{1/2} + 0.06 Re^{2/3}\right] Pr^{0.4} (\mu_\infty/\mu_s)^{1/4} \tag{5.4}$$

where h is the convective heat transfer coefficient, D is the particle diameter, k is the thermal conductivity of the fluid, Re is the Reynolds number, Pr is the Prandtl number and μ_s is the dynamic viscosity evaluated at the surface temperature. Taking the limiting case of creeping flow, the Nusselt number is 2. Even in this case we can see that given the small particle diameter, on the order of 20 microns, the convective heat transfer coefficient is quite large. Taking the same value of thermal conductivity as above, this gives a heat transfer coefficient on the order of $10\,000\,\mathrm{W/m^2-K}$. Therefore, convective heat transfer between the air and the pipe walls is likely to be much smaller than that between the air and particles. In addition, the particle temperature is assumed to be uniform since the Biot number is roughly 0.06 using the above values for the heat transfer coefficient and particle diameter and a thermal conductivity of iron oxide of $3.5\,\mathrm{W/m-K}$.

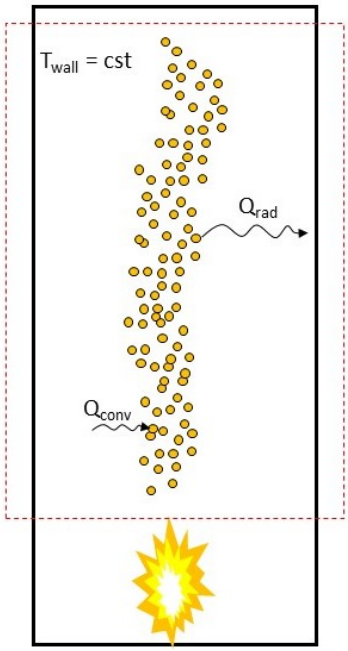

Figure 30: Heat transfer model schematic.

It is assumed that all radiation emitted from the particles is absorbed by the pipe walls. Radiation between the particles and the pipe ends is ignored. This overestimates the heat loss to the pipe walls, but is a good first approximation as the wall view factor is larger than the end caps and any radiation absorbed by the particles will be re-emitted. Using the flow rates, the average particle travel time across the region is determined and the region broken into segments. The radiation from the particles is calculated using the Stefan-Boltzmann equation, assuming that the particles are spherical.

$$Q_{rad} = A\epsilon\sigma(T_{part}^4 - T_{surr}^4) \tag{5.5}$$

where A is the surface area of the particle, ϵ is the emissivity, σ is the Stefan-Boltzmann constant equal to $5.67 \times 10^{-8}\,\mathrm{W/m^2 - K^4}$ and T is the temperature of the particles and surroundings respectively.

The heat lost (or gained) by the air to the particles and the pipe walls by convection is calculated using the following equation:

$$Q_{conv} = h_p A_p(T_{air} - T_p) \tag{5.6}$$

where h is the heat transfer coefficient, A_p is the area of the particles or pipe walls, T_{air} is the air temperature and T_p is the particle or pipe wall temperature, depending on whether the convection between the air and particles or pipe walls is being calculated.

Both equations are solved simultaneously and then the new particle and air temperature are calculated using conservation of energy. The heat lost by the particles during the time step through radiation and gained (or lost) by convection is used to calculate the new particle temperature as follows.

$$\Delta U = Q\Delta t \tag{5.7}$$

$$mc_pT_f = mc_pT_i + (-Q_{loss-rad} + Q_{conv})\Delta t$$

where m is the mass, c_p the specific heat, T_f and T_i are the final and initial temperature respectively and Δt is the time step. The same procedure is carried out for the air using convection lost (or gained) to the particles and the pipe walls. This process is iterated over the length of the combustion chamber.

Heat Extraction

Heat extraction from the flame is assessed with an in-house made heat exchanger. A schematic of the experimental setup is shown in Figure 31. A black steel pipe of the same diameter is used in place of the quartz combustion chamber. A half inch wide by 3 inch tall slit is milled out of the bottom section of the pipe to allow optical access to monitor the flame. Flexible 3/8 inch copper tubing is tightly wrapped around the length of the pipe above the slit. The height covered by

the copper pipe is roughly 13 inches, which corresponds to a surface area of 1300 cm^2 and 50 feet of pipe. The copper tube windings are held together by soldering each layer to each other. The bottom of the tube is the inlet and the top is the outlet for the water that is the working fluid of the heat exchanger. A rotameter with an adjustment knob with a range of 0.2 gpm to 2.0 gpm and graduations of 0.05 gpm is placed upstream of the copper inlet. The rotameter is connected to the tap of the lab sink, which is used as the cold water supply. The outlet of the copper tubing is directed into a large bucket and later on into a steam drain in the lab. Shielded thermocouples are placed directly in the flow of water at the inlet and outlet of the copper tubing. This is done through the use of a Tee with Swagelok fittings that allow a quarter inch thermocouple to fit through and create a watertight seal. In addition, bare thermocouples are secured to the outside of the copper tubing at the inlet and outlet.

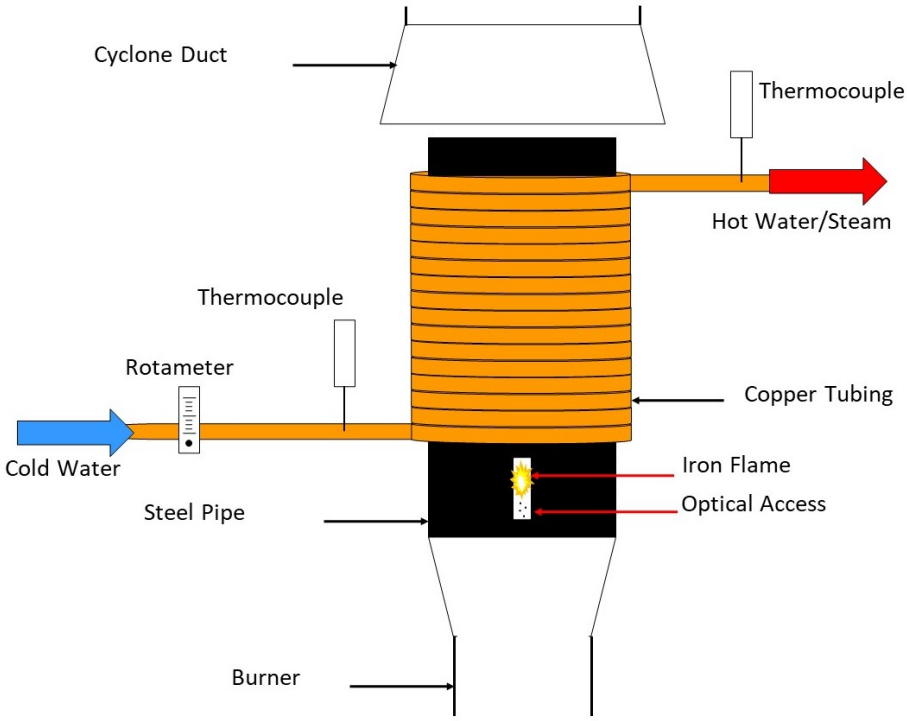

Figure 31: Heat extraction experimental schematic.

The procedure for measuring the heat capture is straightforward. The flame is first ignited and stabilized. Next the water flow rate is set to the specified value with the rotameter and allowed to flow through the tubing. Once the temperature of the water at the outlet remains constant for 3 minutes, the process is assumed to have reached steady state. Inlet and outlet temperatures and flow rate are recorded. The flow rate is then adjusted to the next value and the process is repeated.

The water flow rates are chosen such that the outlet temperature should be well below boiling, based on calculation of the power of the flame and the temperature of the inlet tap water.

The heat capture experimental apparatus is shown in Figure 32. The left pane of the figure shows the length of coils wrapped around the steel combustion chamber and the thermocouples placed into the flow are circled in red. The right pane is a photo taken during an experiment run with an active stabilized iron flame. The copper coils are insulated with a 1.5 inch thick steam-resistant high-temperature fiberglass insulation pipe. The viewing slit can be seen at the bottom of the insulation and allows the flame to be monitored and ensures proper ignition and stabilization. The heat capture from the apparatus is assessed using the first law of thermodynamics applied to the flowing water.

$$\dot{Q} = \dot{m} c_p \Delta T \tag{5.8}$$

where $\dot{Q}$ is the rate of heat flow in W, $\dot{m}$ is the mass flow rate of water in kg/s, c_p is the specific heat capacity of water which is taken as 4180 J/kg-K in the temperature range observed, and ΔT is the difference in temperature between the outlet and inlet of the copper tubing.

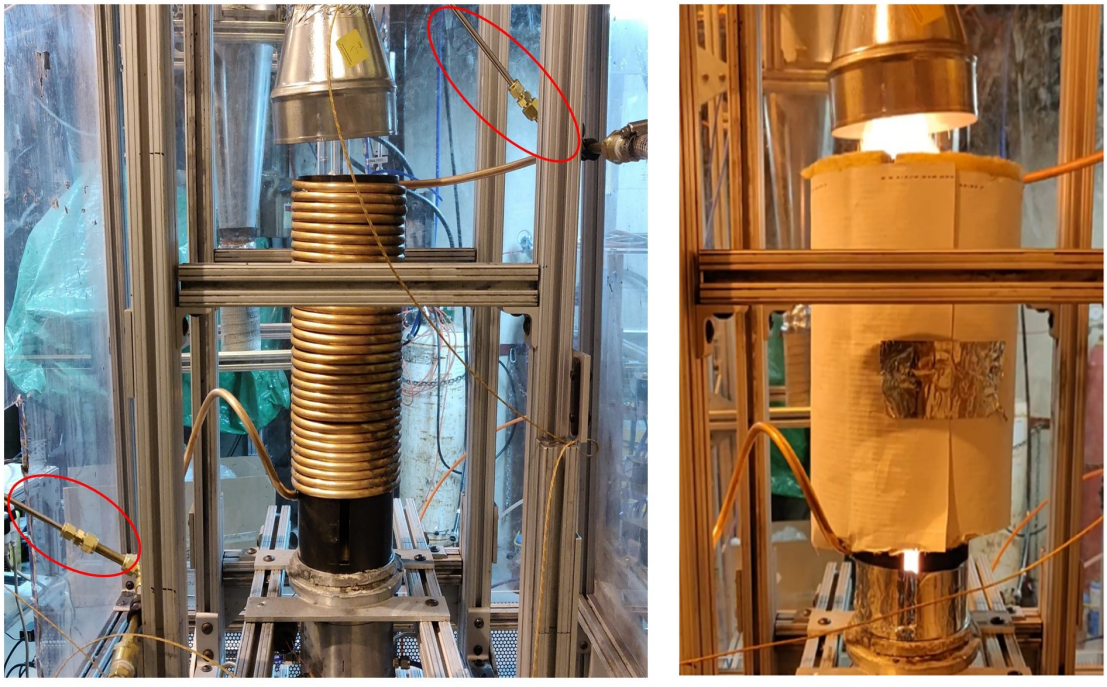

a. Wrapped coil in practice

b. Insulated with active iron flame

Figure 32: Heat extraction experimental setup.

Particle Size

Particle size analysis is carried out on the powder before and after combustion. The work is performed by a technician in the analytical labs of the Department of Materials Engineering. A Horiba LA-920 laser scattering particle size analyzer is used and the powder is dispersed in water. A subset of samples are also tested with a Microtrac Sync particle sizer with dynamic image analysis that was later acquired by the analytical lab. In dynamic image analysis, a camera system detects a stream of moving particles. The particle images are recorded as shadow projections and are analyzed in real time. This particle sizer allows images of the particles to be taken and various form factors can be analyzed such as the sphericity.

Thermogravimetric Analysis

One technique used to assess the combustion efficiency of the burner is thermogravimetric analysis (TGA). A thermogravimetric analyzer is a machine with a high precision scale that allows the mass of a sample to be measured as the temperature is increased. The sample is placed in a heating chamber that is sealed from the environment and can be heated in the presence of oxidizing or inert gas. Carrying out TGA on the powder in the presence of an oxidizing medium will give an indication of how oxidized the powder is based on the mass increase. A fully burnt, i.e. oxidized powder should not increase in mass.

The work is performed by the graduate student on a TA Q500 thermogravimetric analyzer. The analyzer is provided by the McGill Structures and Composite Materials Laboratory in the Department of Mechanical Engineering. Data processing is carried out using the TA Universal software which allows the data to be exported in ascii format for further processing in Matlab. TGA is carried out on both unburnt and burnt powder. Before use, each sample tray is cleaned with alcohol and then heated with a blowtorch until glowing red. The empty tray is then tared on the Q500 scale. The tray is then retrieved and roughly 20 to 30 mg of powder is placed onto it. The sample is then heated at a rate of 50 °C per minute until 800 °C, then held at constant temperature for 30 minutes and finally cooled at a rate of 35 °C per minute to room temperature. The temperature schedule is based on the ignition temperature of iron, as well as preliminary testing of different maximum temperatures and time segments. Extra dry compressed air is used as the oxidizing gas for all samples. After each run, the oxidized samples are stored for further analysis using scanning electron microscopy and X-ray diffraction.

Particle Morphology

Particle imaging is done with a scanning electron microscope (SEM). Imaging is carried out on the powder before and after combustion, as well as before and after thermogravimetric analysis. The work is performed by a technician from the McGill Facility for Electron Microscopy Research, under the supervision of the graduate student. The electron microscope used is the FEI Quanta 450 Environmental Scanning Electron Microscope.

Combustion Products Composition

X-ray Diffraction (XRD) is another technique used to assess the combustion efficiency of the burner. XRD gives the chemical composition and phases of a substance by comparing the interference pattern created by the x-rays diffracted off the atoms to a known database of elements. XRD is used in this analysis to determine the composition of the burnt powder and evaluate the combustion efficiency based on relative proportion of the iron and iron oxide phases. The work is performed by a graduate student from the McCalla Lab of the Department of Chemistry on a molybdenum source x-ray diffractometer.

5.3 Results

Particle Temperature

The results of the particle temperature measurements are shown below. Figure 33 is a representative emission spectra profile of the iron flame with the region of interest circled. Figure 34 shows the scaled and corrected fit of the spectral data to Wien's approximation. Lastly, Figure 35 shows the particle temperature for each measurement. The average measured temperature is 2080 K.

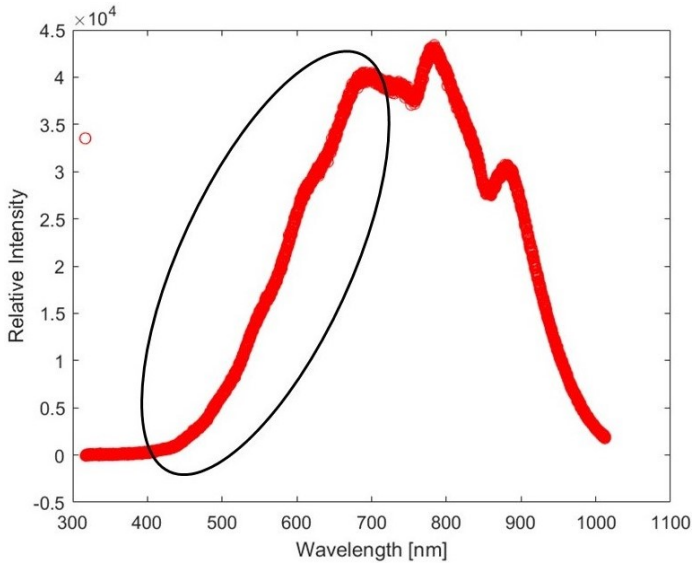

Figure 33: Emission spectra of iron air flame in the range of 300-1000 nm.

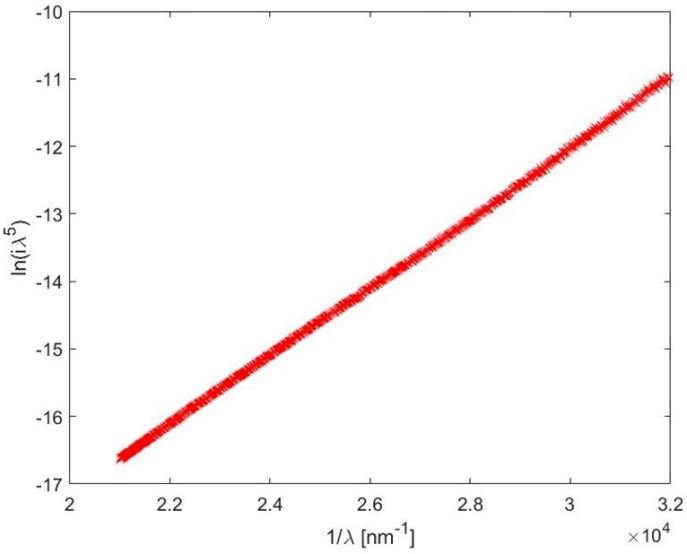

Figure 34: Linear fit of spectral intensity to Planck's Law.

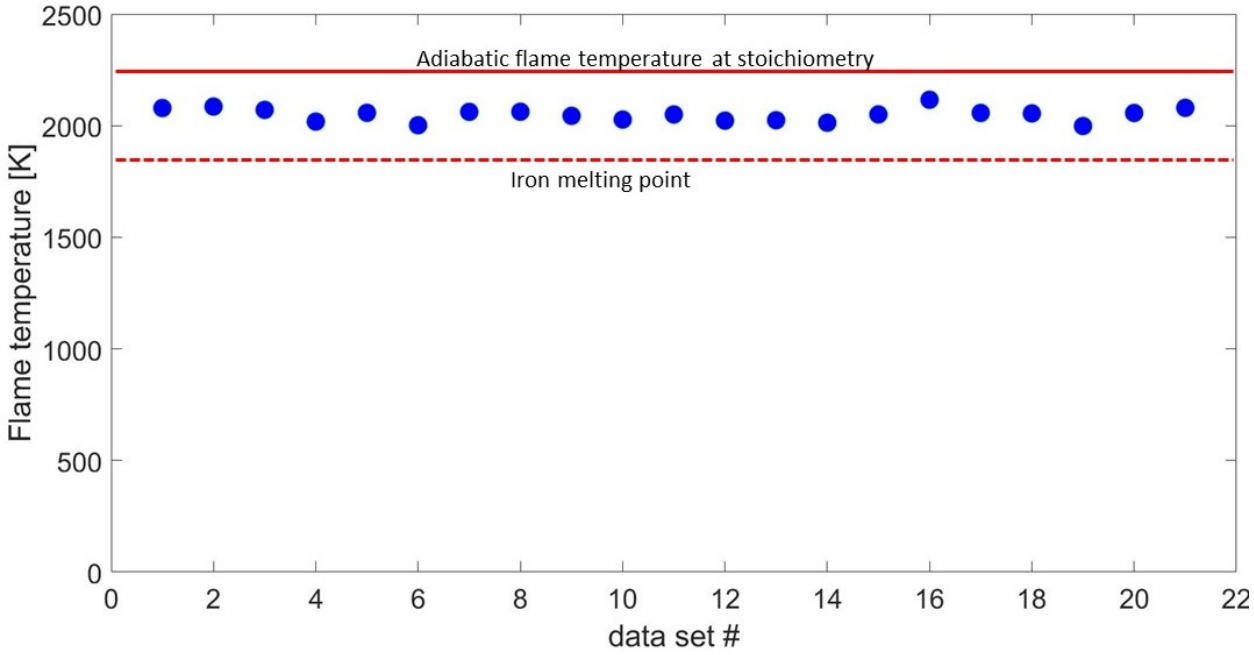

Figure 35: Temperature of iron air flame for each measurement.

Heat Extraction

The results of the heat extraction experiments for eight different flow rates are shown in Figure 36. The average heat extracted from the flame is 3 kW ±0.5 kW.

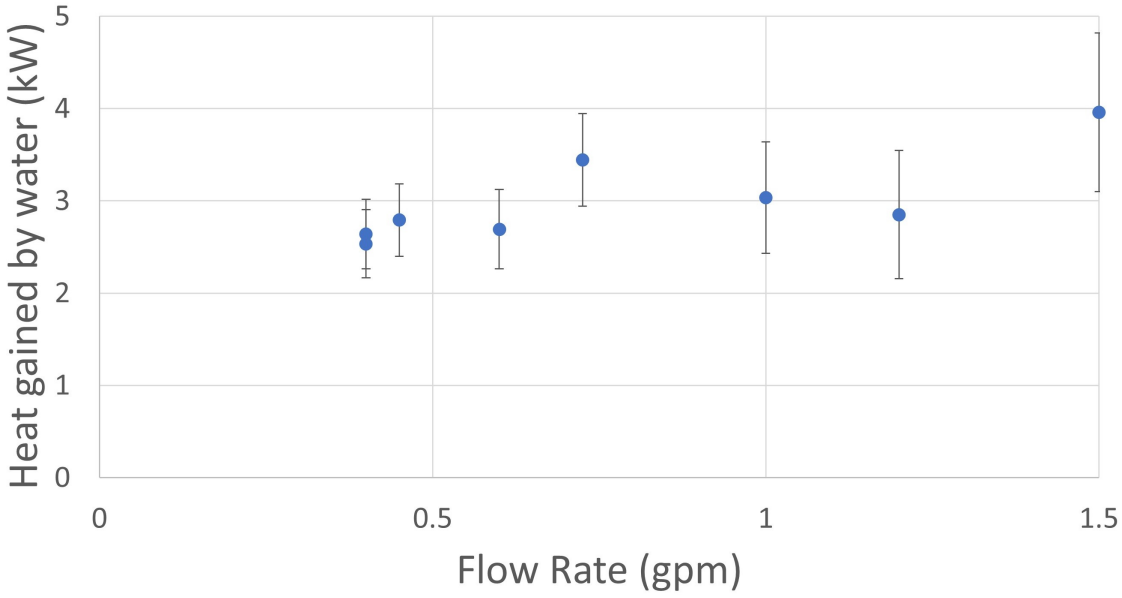

Figure 36: Heat captured by water from iron flame.

Heat Transfer Model

The results of the heat transfer model agree with the measured values from the extraction experiment, however with some differences. A graph of the temperature of the particles and air, the heat lost to the pipe walls from both the particles and the air, as well as the heat transfer from the air to the particles is shown in Figure 37. The heat gained by the tube wall, the sum of the heat lost by the particles through radiation and the air through convection, in a 30 cm section of pipe is roughly 4000 W. This is greater than the average heat gained in the heat extraction experiment, but the model also overestimates the heat extracted based on final particle temperature.

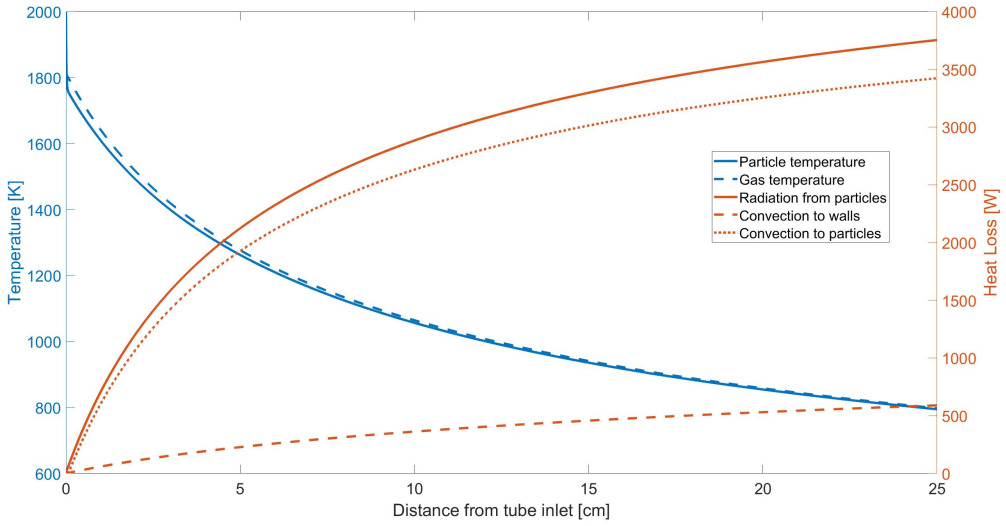

Figure 37: Modelled heat transfer between particles, air and combustion chamber walls.

Particle Size

Particle size analysis was carried out on every batch of new powder and every corresponding batch of burnt powder that is collected from the cyclone. Figure 38 shows the particle size distribution of a powder provided by Tata Steel Ltd. that was studied extensively. This set of powder is used with all the analysis techniques (TGA, SEM, XRD) in order to get an accurate depiction of the combustion process. As can be seen from the graph, the unburnt powder has a tighter distribution, but also a smaller mean particle size than the burnt powder. The top corner of the figure shows the key particle size metrics of the unburnt and burnt powders. The D10, D50 and D90 represent the size below which 10%, 50% and 90% of the particles fall. For the unburnt powder, the mode, mean and median fall within a tight band. However, for the burnt powder the mean is higher

than the mode and median because of the outlier particles. Comparing these values clearly shows the increase in particle size between burnt and unburnt powder. Figure 39 shows the particle size distribution of another powder purchased from TLS Technik Spezialpulver, that is sold as spherical powder with a sub 25 micron particle size. The same phenomena is seen as with the Tata powder: a tighter distribution for the unburnt powder and an increase in the mean particle size after combustion. For this powder the top corner of the figure displays the mean value measured using three different techniques, all showing the increase in particle size.

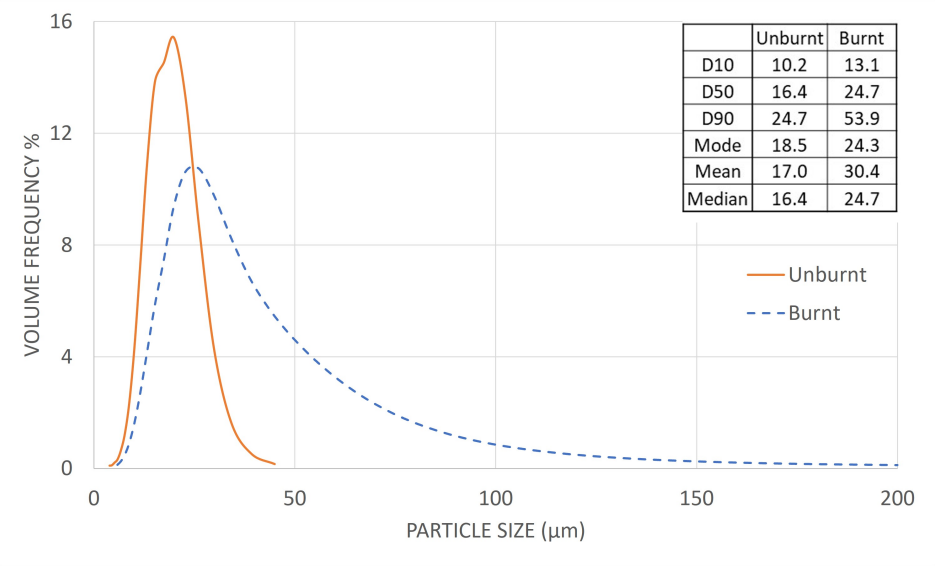

	Unburnt	Burnt
D10	10.2	13.1
D50	16.4	24.7
D90	24.7	53.9
Mode	18.5	24.3
Mean	17.0	30.4
Median	16.4	24.7

Figure 38: Particle size distribution of unburnt and burnt powder from Tata Steel Ltd.

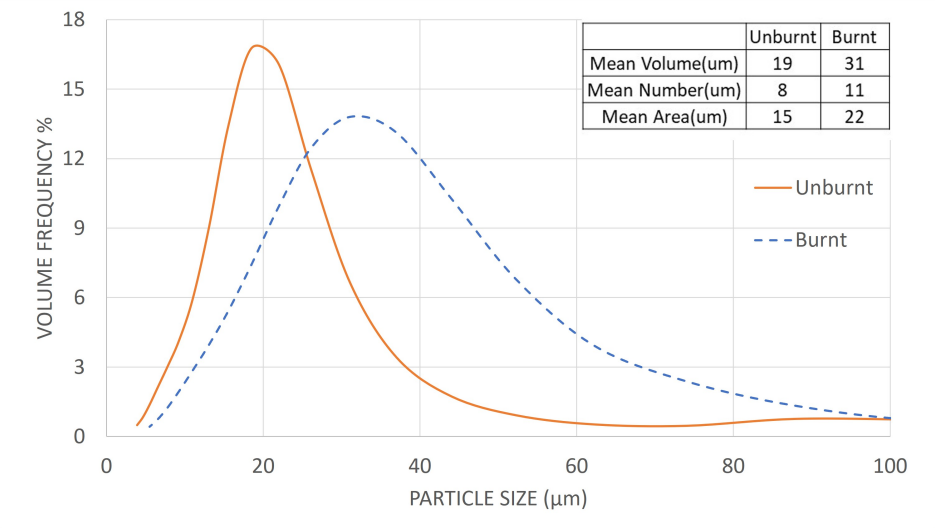

	Unburnt	Burnt
Mean Volume(um)	19	31
Mean Number(um)	8	11
Mean Area(um)	15	22

Figure 39: Particle size distribution of unburnt and burnt powder from TLS Technik Spezialpulver (Now Eckart TLS).

Figure 40 shows the visual results of the dynamic image analysis. As mentioned, the technique enables the recording of shadow projections of the particles and analysis in real time, which yields many different shape characteristics. The majority of the particles shown appear to be very circular, while a handful are oddly shaped. These results will be understood more clearly after the particle imaging with scanning electron microscopy. Figure 41 shows three parameters that are used to evaluate how round the particles are. The first is simply the aspect ratio of the particle, which is generally measured using the largest and smallest Feret diameter (also called caliper diameter), but can also be largest diameter and the shortest orthogonal diameter. The closer the aspect is to 1, the closer it is to a circle. The second parameter is the circularity, which is the ratio of the projected area to the square of the projected perimeter. Again, the closer the value is to 1, the more circular the object, whereas a shape like a starfish will have a very low value. The last parameter is the sphericity, which is a measure of how close a shape is to a sphere. It is defined as the ratio of the surface area of a sphere with the same volume as the given particle to the surface area of the particle. Figure 42 shows the results of the shape factor analysis from the dynamic image data. The table on the bottom right of the figure gives the average values for the shape factors.

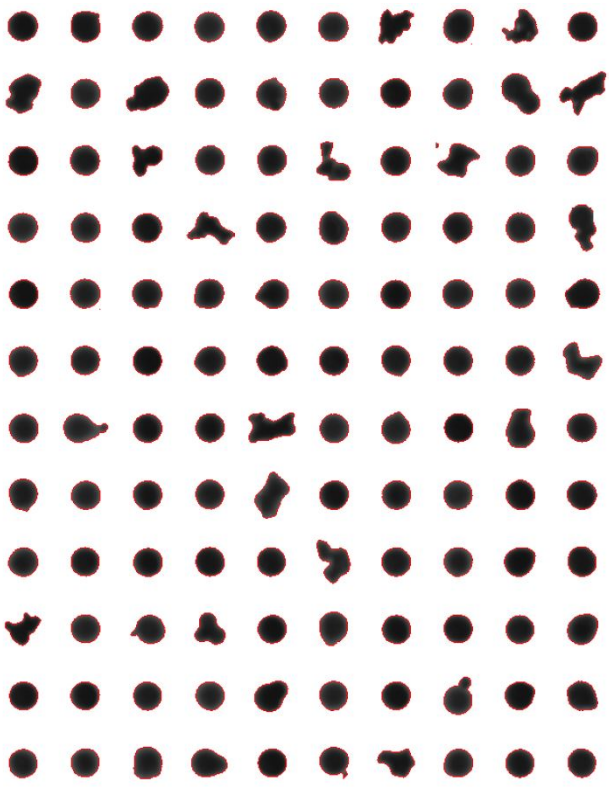

Figure 40: Dynamic imaging of particle shadows.

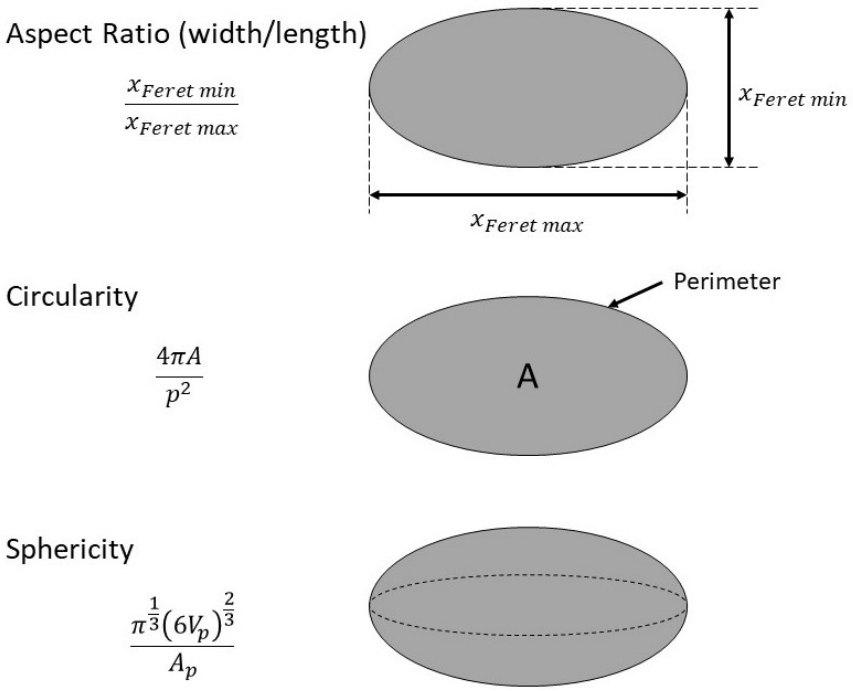

Figure 41: Parameters to evaluate the shape of particles.

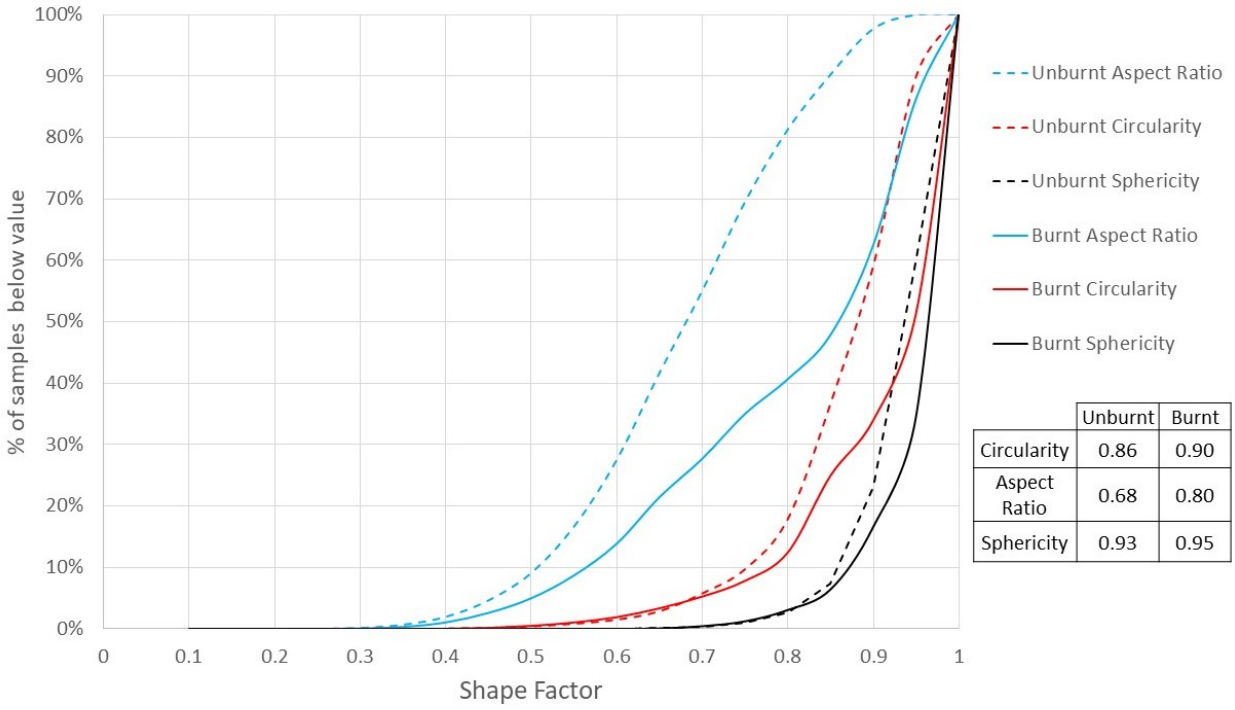

	Unburnt	Burnt
Circularity	0.86	0.90
Aspect Ratio	0.68	0.80
Sphericity	0.93	0.95

Figure 42: Comparison of shape factors for unburnt and burnt powder.

Thermogravimetric Analysis

Thermogravimetric analysis was carried out on several different burnt and unburnt powders. The results of the TGA are the mass of the sample as a function of time and temperature. These results are plotted in Figure 43. The red dashed curve represents the temperature schedule as described in the methodology of section 5.2. The yellow curve and black dotted curve represent the mass increase of the unburnt powders over time. The three lower curves (red, green & blue) are the mass increase of the burnt powder collected from the cyclone. There is a large increase in mass for the unburnt powder, and a very small one for the burnt powders as expected. The ratio of the final to initial mass of the unburnt powders is 1.42. For the burnt powders the ratio is 1.04 on average.

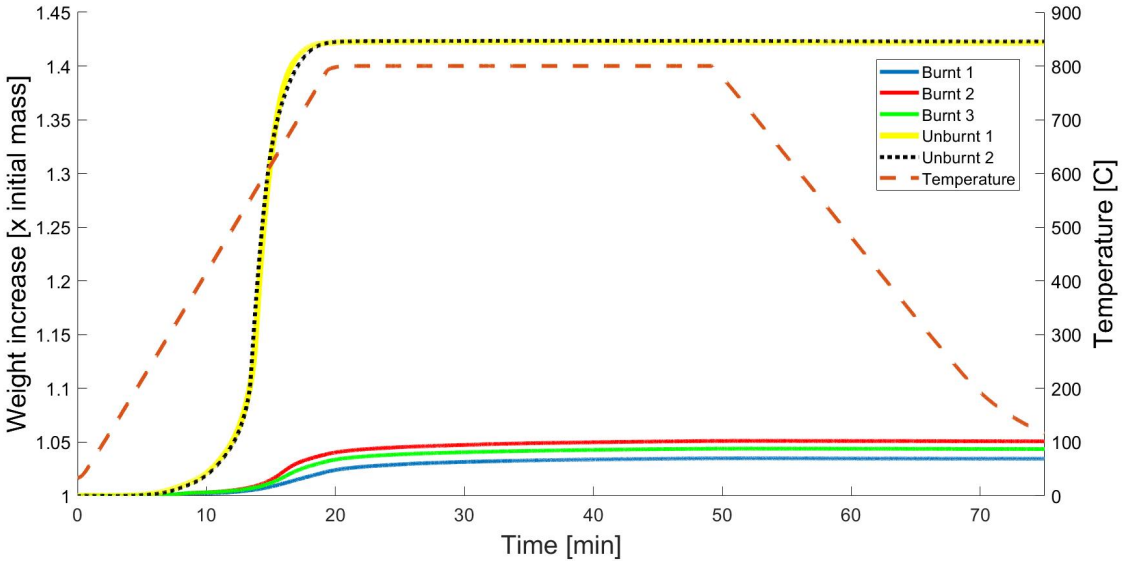

Figure 43: Weight increase of unburnt and burnt powders as a function of time and temperature.

Particle Morphology Imaging

Particle imaging using scanning electron microscopy was carried out on unburnt powder and burnt powder, as well as those powders after having undergone oxidation with thermogravimetric analysis. Photos of the different powders are shown in Figures 44 through 52. As can be seen in Figure 44 and Figure 45, the unburnt particles have irregular shapes and internal structures that resembles an agglomeration of odd shapes. This is typical of sponge iron. Figures 46, 47 and 48 show the particles after combustion. The difference between the two cases is striking. In the latter case the particles are nearly all spherical. Some irregular shaped particles similar to the unburnt ones remain, however the majority are spherical with a smooth outer surface. Figure 48 displays the

size of some of the particles, showing that there is a range of sizes, all of which are on the order of the unburnt distribution. Figures 49 and 50 show the unburnt powder after undergoing slow oxidation during TGA. Despite oxidizing completely, based on the mass increase from the TGA analysis, the shape of the particles do not change appreciably. Upon closer inspection of the higher magnification, a highly porous surface can be seen on the particles, unlike the smooth surface of the burnt particles. This is to be expected with a slow oxidation process, where oxygen can diffuse through the particle over time. Figure 51 and Figure 52 show the burnt particles after undergoing oxidation in the TGA. The particles remain spherical and many of the smaller particles are stuck on the surface of the larger ones. This is an artifact of the TGA process, as all samples were stuck together after removal from the TGA and were mechanically broken apart before SEM. However, as evidenced on the higher magnification photo, the surface is no longer smooth. The slow oxidation caused a layer of oxides to form and paths for oxygen to diffuse through the surface of the particles.

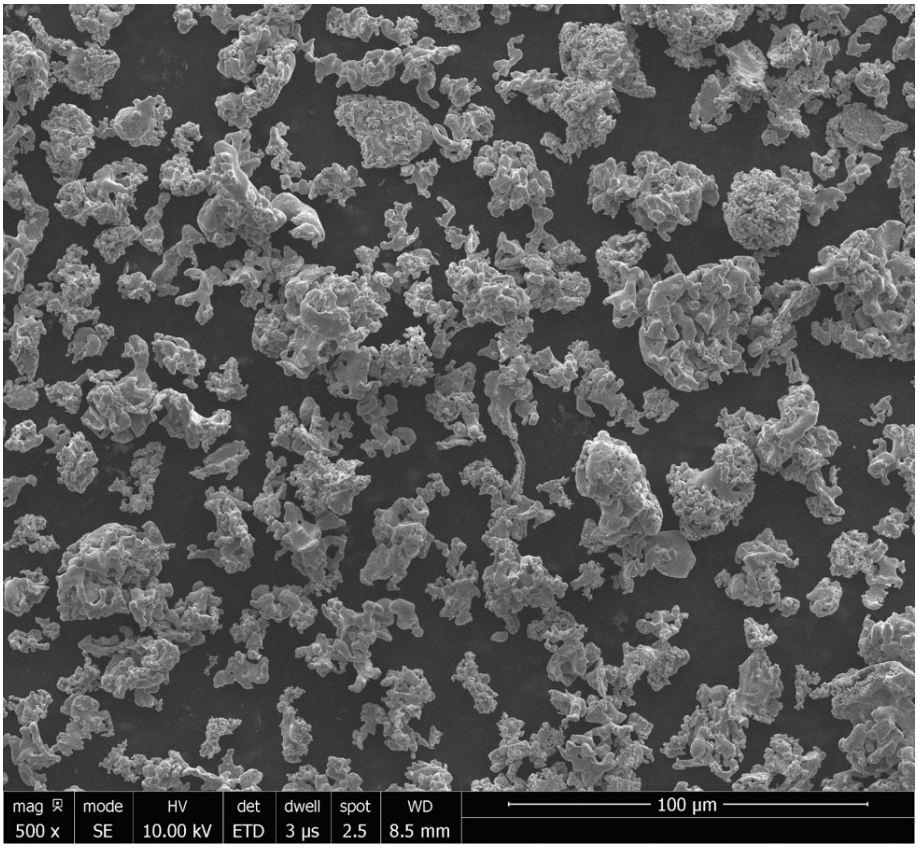

Figure 44: Unburnt particles.

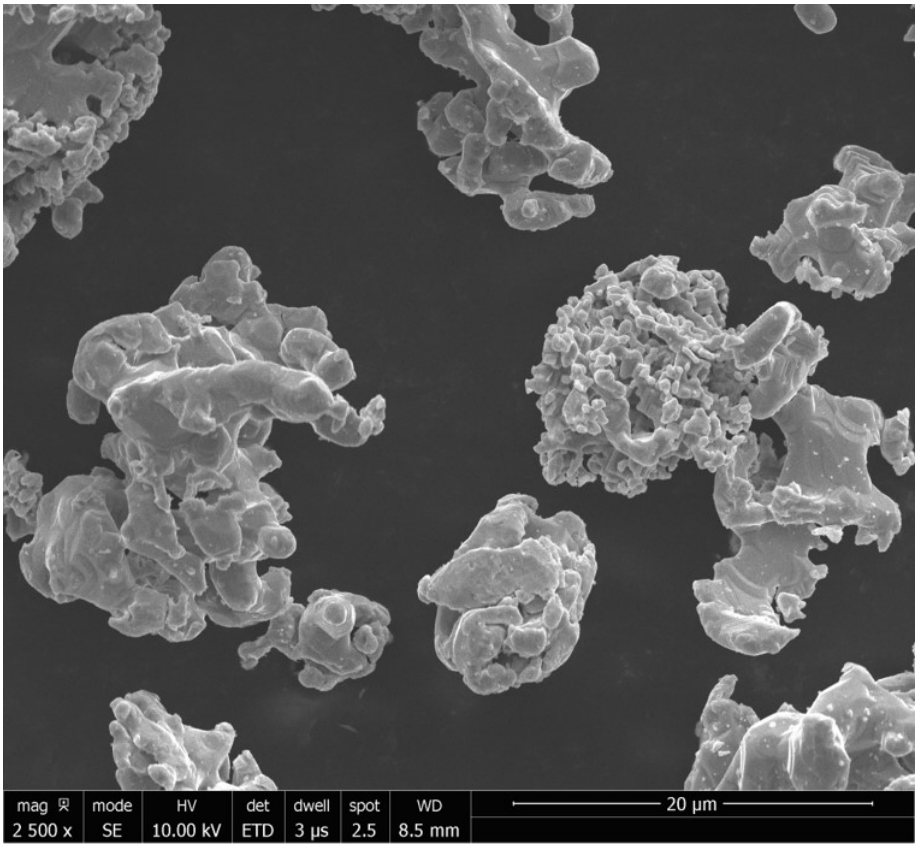

Figure 45: Unburnt particles - higher magnification.

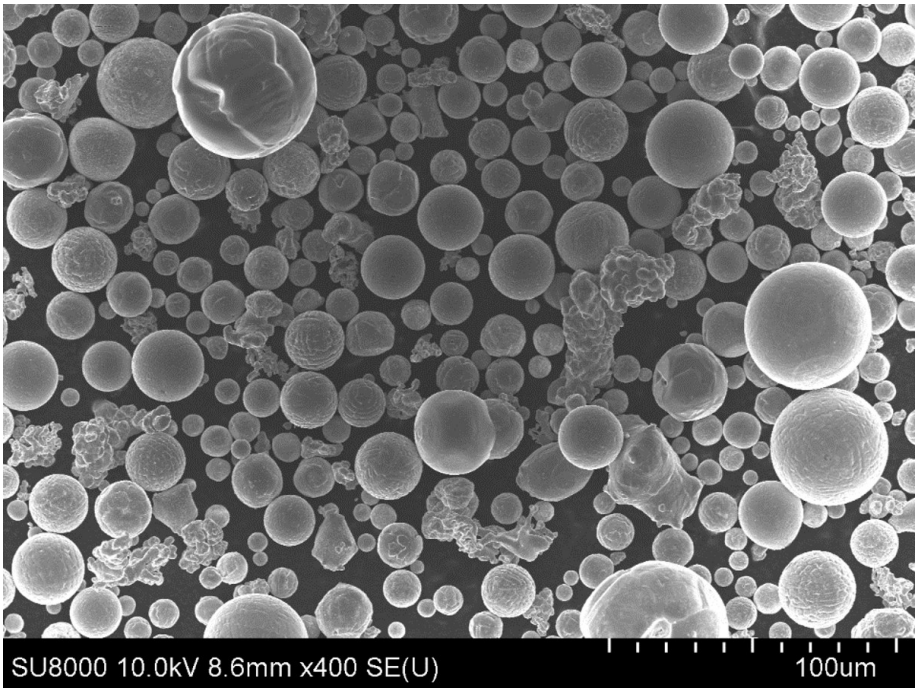

Figure 46: Burnt particles.

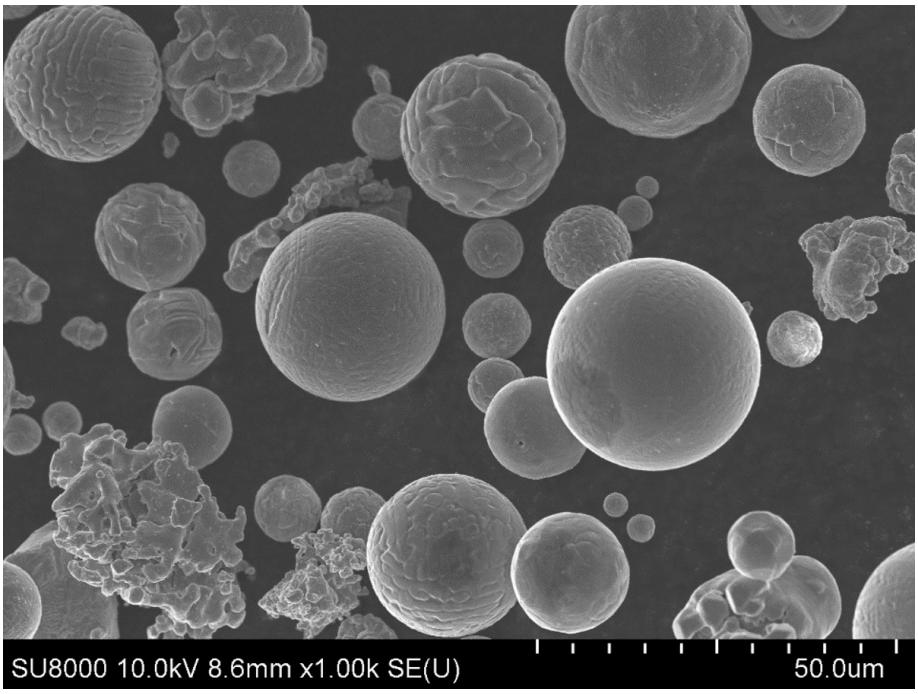

Figure 47: Burnt particles - higher magnification.

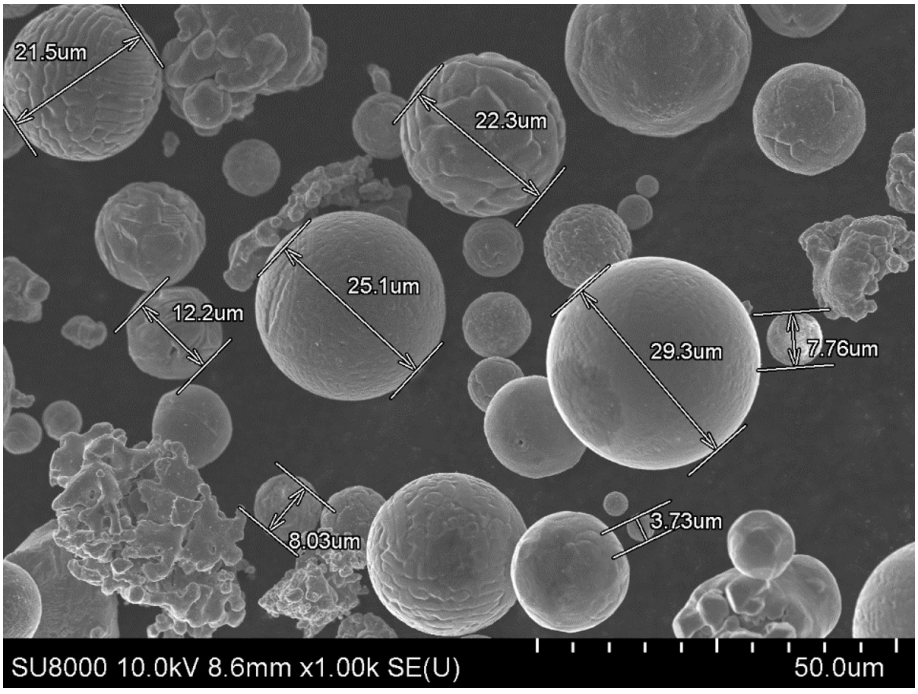

Figure 48: Burnt particles - higher magnification with dimensions.

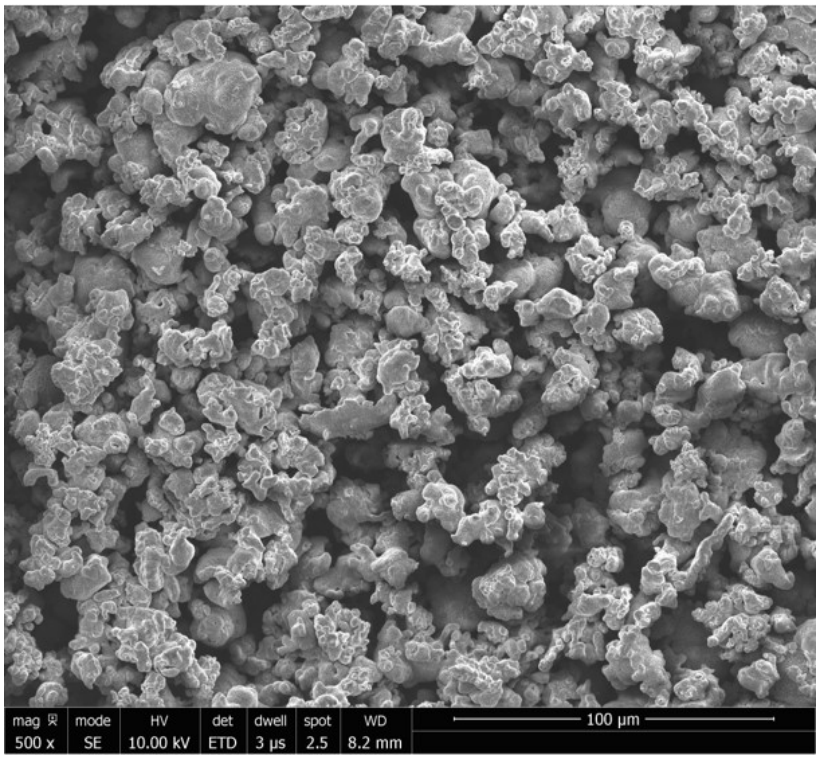

Figure 49: Unburnt particles post oxidation in TGA.

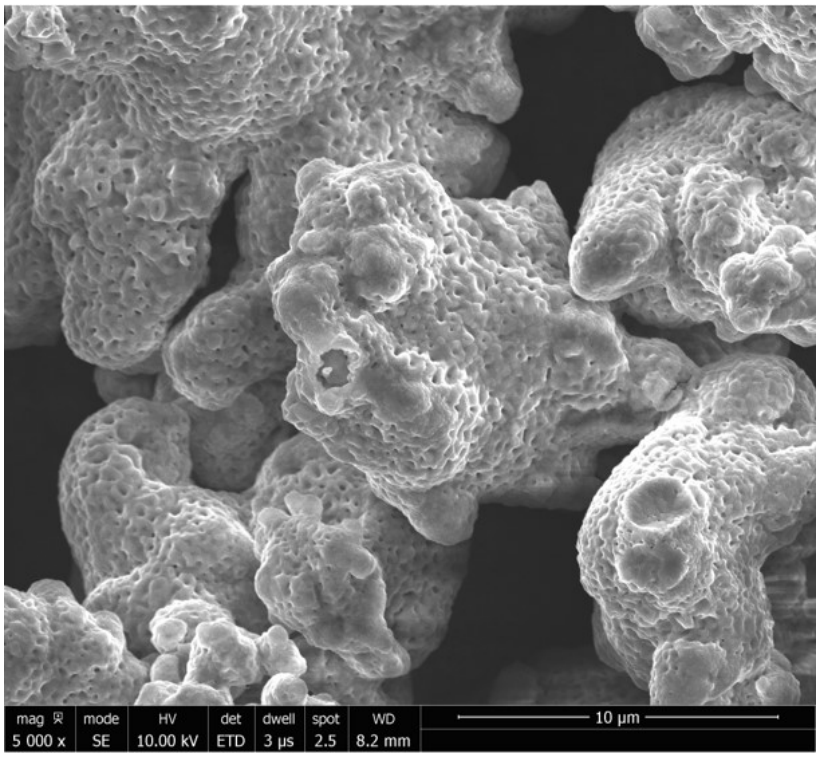

Figure 50: Unburnt particles post oxidation in TGA - higher magnification.

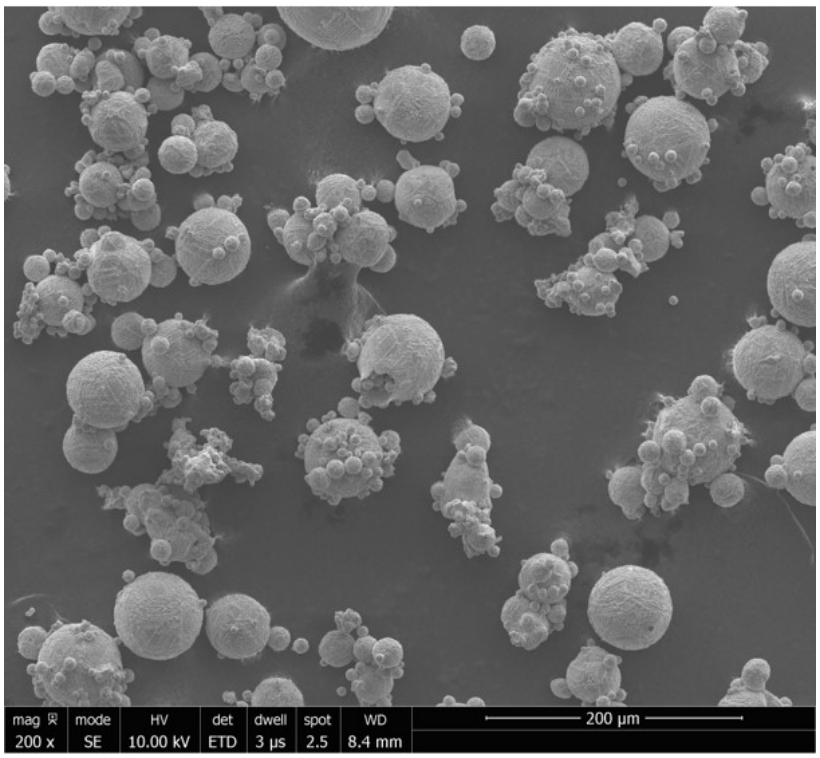

Figure 51: Burnt particles post oxidation in TGA.

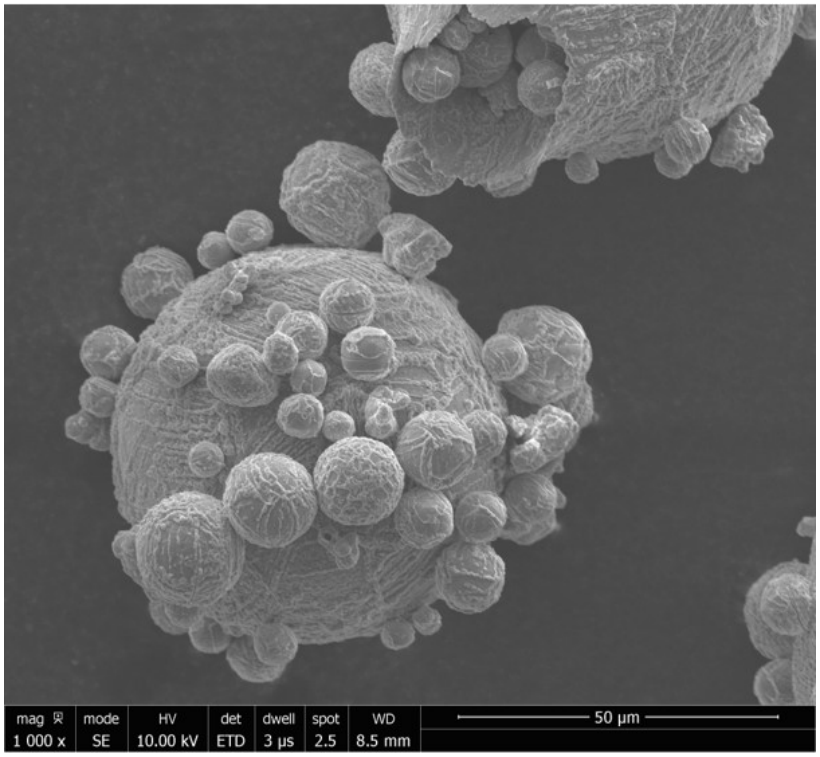

Figure 52: Burnt particles post oxidation in TGA - higher magnification.

Combustion Products Composition

The results of the x-ray diffraction analysis for the unburnt and burnt powders, both before and after TGA are shown in Figure 53. The XRD compares the scattering of the powders to known scatterings of reference materials, as seen in the figure. The peaks can then be matched to determine the composition of the sample. This is very clearly seen by looking at the Fe reference compared to the unburnt iron sample. Analysis performed on this data allowed quantitative information to determined, as shown in the table of Table 1. The accuracy of the XRD analysis is estimated to be within 1% of the given values.

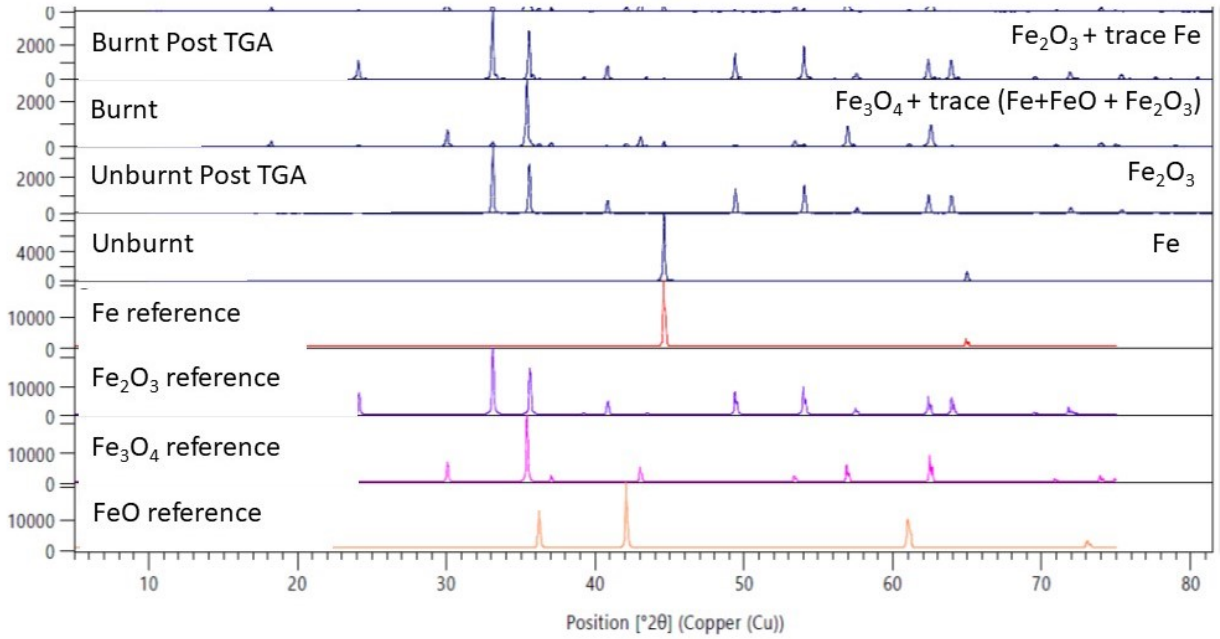

Figure 53: X-ray diffraction peaks of powder samples.

Table 1: Composition of burnt and unburnt powders before and after TGA

Sample	Fe %	FeO %	Fe_3O_4 %	Fe_2O_3 %
Unburnt	100	0.0	0.0	0.0
Unburnt Post TGA	0.0	0.0	0.0	100
Burnt	2.7	9.5	77.1	10.7
Burnt Post TGA	0.2	0.1	0.0	99.7

5.4 Discussion

Combustion efficiency

The oxidation of iron with air is a complex process that depends on the temperature, oxygen concentration and partial pressures of the gases. Iron has several oxides and they are able to coexist in layers. The Gibb's energy indicates which oxides will form at different temperatures and pressures. This can be calculated for each oxidation reaction at the specified temperature. Alternatively, the same information can quickly be gained from observing the iron-oxygen phase diagram and then mapping it to the oxide scales as shown in Figure 54. The outer shell is composed of Fe_2O_3 (hematite) since it is formed at higher oxygen concentrations and is the highest oxide (most stable state). The next layer is Fe_3O_4 (magnetite) and finally FeO (wüstite), which forms on the iron core boundary. Oxygen can diffuse through each layer all the way to the core allowing oxidation to proceed, as discussed in section 1.2. However, the rate of diffusion of oxygen can be slower than the rate of iron diffusion, since the Fe cations are more mobile through lattice diffusion. Lattice diffusion is the movement of atoms within the crystalline lattice structure either by interstitial or substitutional mechanisms. This means that the oxidation reactions can also be driven by iron cations moving through the oxide layers to react with the oxygen present.

A simple process that can give a qualitative estimate of the combustion efficiency is the assessment of the geometric properties of the unburnt and burnt powders. This of course is only valid in the case of sponge iron (or another irregular shaped powder such as water atomized iron) where the initial powder is non-spherical. As seen in Figure 46, the burnt powder is mainly comprised of spherical particles. The smooth spherical shape of the particles after burning is due to the particles melting during combustion and then solidifying into a sphere as they cool. The melting temperature of iron is 1538 °C and as shown in Figure 35, the measured temperature of the particles in the flame is roughly 1800 °C. Therefore, by examining the circularity, aspect ratio and sphericity, the completeness of combustion between powder samples can be assessed. The results of that analysis are shown in Figure 42. For all parameters, the burnt powder has values closer to unity, indicating a more round spherical shape. The graph displays the percentage of particles below a certain value of shape factor for each of the three shape factors and for both the burnt and unburnt powders. As can be seen, all the curves for the burnt powder (solid lines) are shifted to the right compared to the unburnt powder (dashed lines). This indicates of course that the average is higher. However, it also provides more insight on the general shape of the particles. Establishing a threshold value

of 0.9, which indicates very round or spherical, it can be seen that over 65% of unburnt particles do not meet this criteria, while only 35% of burnt particles fall below this threshold in terms of circularity. This indicates the majority of the unburnt particles are irregularly shaped. There is also a noted difference between the aspect ratio of the burnt and unburnt particles. As expected the unburnt powders have a lower aspect ratio because of their oblong shape. This difference is less apparent in the sphericity, likely because smaller particles agglomerate into oblong shapes.

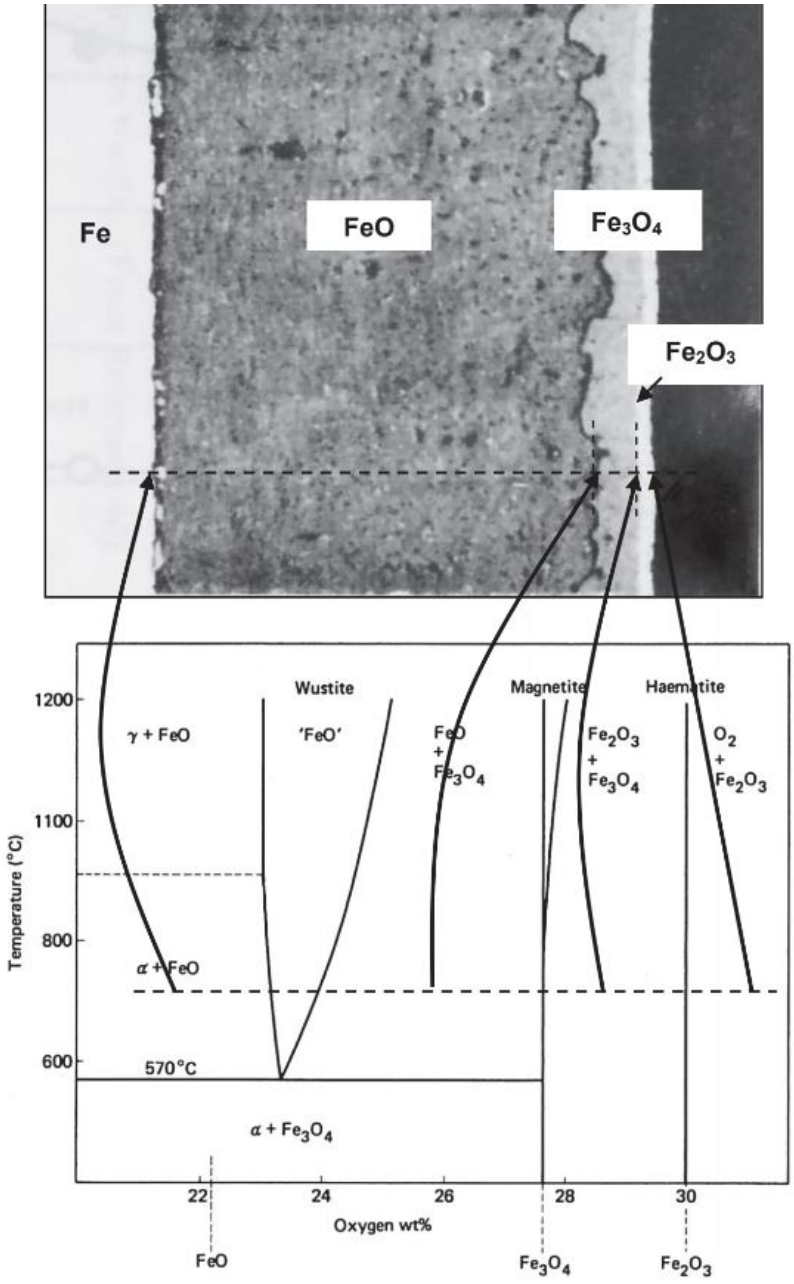

Figure 54: Iron oxidation process. Source: Reprinted from [66]

More detailed quantitative analysis of the combustion efficiency is obtained using thermogravimetric analysis and X-ray diffraction. Based on the results of the TGA shown in Figure 43, where the average weight increase for the unburnt powders is 42%, the likely oxidation reaction of unburnt powder is the formation of Fe_2O_3. However, for the burnt powders, where the weight increase is 4% there are two possibilities. The first hypothesis is that the weight increase is due to some amount of unburnt powder left in the sample. In this case, the combustion efficiency can be calculated using the following simple relation. Knowing that an unburnt powder yields a mass increase of 42%, then the fraction of unburnt iron that yields a mass increase of 4% is

$$\frac{100\%\ iron}{42\%\ mass\ increase} = \frac{x\ iron}{4\%\ mass\ increase} \tag{5.9}$$

this yields 9.5% unburnt iron, which means a 90.5 % combustion efficiency.

The second hypothesis is that the mass increase is not due to unburnt iron remaining in the sample, but actually the oxidation of Fe_3O_4 to Fe_2O_3, which is thermodynamically favored at these temperatures (800 °C) with a Gibb's free energy of $\Delta G^0 = -98\,478.9$ J/mol and which benefits from faster kinetic rates at higher temperatures. This reaction has also been demonstrated in chemical looping combustion experiments [67], where iron oxide is cycled back and forth between Fe_3O_4 and Fe_2O_3 in a TGA with CO as the reducer and air as the oxidizer at 800 °C. Figure 55 shows the potential oxidation reactions for magnetite and hematite, as well as the associated mass increase, which is 3.45% for Fe_3O_4 to Fe_2O_3. This is nearly the same increase seen in the TGA results, meaning that the second hypothesis is likely valid. However, it is also more than likely that the reality is somewhere between the two, with a small amount of unburnt iron remaining in the sample, and the majority being Fe_3O_4, which then gets oxidized to Fe_2O_3.

This conclusion is further investigated with XRD analysis to get the exact phase composition of the powders, the results of which are shown in Table 1. As expected, the unburnt powder is pure iron and when oxidized in the TGA becomes pure hematite, since the reaction of iron and air to hematite is thermodynamically favored at equilibrium even though the kinetic rate of formation of hematite is slower than that of magnetite [68]. The composition of the burnt powder is mostly comprised of magnetite and only a small fraction, 2.7 %, of the sample is pure iron. This data corroborates the second hypothesis discussed above, which is that when oxidizing the burnt powder in the TGA there is a clear chemical transformation and uptake of additional oxygen to form magnetite from hematite.

The important point for the combustion efficiency is that the burnt powder only has 2.7% of pure iron remaining. However, there are three possibilities that can explain the pure iron remaining in the sample. The first possibility is simply that there is a small amount unreacted iron remaining in the core of some or all the samples. The second possibility is that there are some completely unburnt particles remaining in the sample, such as the irregular shaped ones, and the rest are completely oxidized. The final possibility is that the particles completely reacted, but formed pure FeO, which is unstable below 570 °C. As the particles cool back down to room temperature, the FeO decomposes into $\alpha - Fe$ and Fe_3O_4 as seen in Figure 54. To determine which hypothesis is accurate would require SEM imaging of particles that have been cut in half. This would show if there is an unreacted small core of iron, indicating incomplete combustion, or if there is the presence of Fe scattered throughout the particle which would indicate it is formed during decomposition of FeO. It would also show whether the irregular shaped particles are uniform iron or contain various phases indicating combustion.

The combustion efficiency is defined as the ratio of the burnt or oxidized powder to the initial unburnt powder. Therefore the combustion efficiency here can be determined by back calculating the initial amount of iron that corresponds to the burnt sample, since the mass of the burnt sample is greater than the initial dispersion. A simple way to do this is to assume a 100 g sample of burnt powder, with the composition determined by XRD according to Table 1. The initial mass of iron corresponding to this composition can then be calculated as follows

$$m_{Fe from Fe_3O_4} = 100g \cdot 77.1\%\ Fe_3O_4 \cdot \frac{1 mol Fe_3O_4}{231.55g} \cdot \frac{3 mol Fe}{1 mol Fe_3O_4} \cdot \frac{55.85g\ Fe}{mol Fe} = 55.79\ g \quad (5.10)$$

This calculation is repeated for each of the phases yielding, 2.7 g from Fe, 7.38 g from FeO and 7.48 g from Fe_2O_3. The combustion efficiency is then calculated using the total mass

$$\text{combustion efficiency} = (1 - \frac{m_{unburnt}}{m_{initial}}) \cdot 100\% \quad (5.11)$$

$$= (1 - \frac{2.7g}{73.35g}) \cdot 100\% = 96.32\%$$

The combustion efficiency of over 96 % is extremely high, especially considering it is the first burner of this type. However, the presence of all the different phases indicates that the reaction

has not gone completely to the lowest state and thus not released the maximum amount of energy.

There are several theories about the oxidation of iron that draw on knowledge from metallurgical engineering, iron and oxygen solubility and diffusion rates and the iron-oxygen phase diagram. Work by Steinberg et al. [34] suggests a structure composed a solid core, followed by a molten iron layer and finally a liquid iron oxide layer with dissolved oxygen that is the interface with the surrounding oxidizing gas. Calculating the Gibb's energy at these elevated temperatures indicates that both FeO and Fe_3O_4 could form. As the particles cool, the FeO decomposes into Fe and Fe_3O_4 as mentioned, which would explain why the majority of the burnt sample is Fe_3O_4. One explanation for why there is little Fe_2O_3 is its slow kinetic rate of formation. The formation of Fe_2O_3 is significantly slower than the formation of FeO and Fe_3O_4 over the temperature range where is Fe_2O_3 is stable. This can be seen from the scale growth rates measured by Paidassi [68]. On the other hand, the exsolution of oxygen from a liquid solution being cooled down to a thermodynamic state with a lower solubility of oxygen can be much faster than the oxidation towards Fe_2O_3. This is seen in the outgassing of oxygen and formation of Fe_3O_4 upon cooling rather than forming Fe_2O_3 [35]. This is consistent with the theory that in the flame zone the main product formed is FeO. Downstream post combustion, as more air is added and the flow is cooled, the subsequent oxides begin to form. However, since it has been shown that FeO is unstable below 570 °C, its presence in the burnt sample indicates rapid cooling took place, which essentially froze the FeO in place. The presence of all the phases means the internal structure of the burnt particles likely resembles that of Figure 54, with a small core of pure iron, followed by a small layer of FeO, a large layer of Fe_3O_4 and lastly a thin shell of Fe_2O_3. However, as explained, SEM imaging of the interior of the particles is required to confirm this theory.

Molar Mass	Reaction	Final mass/initial mass
Fe: 55.85 g/mol	$2Fe + 1.5O_2 \rightarrow Fe_2O_3$	$\frac{Fe_2O_3}{2Fe} = \frac{159.7}{111.7} = 1.43$
Fe_2O_3: 159.7 g/mol	$3Fe + 2O_2 \rightarrow Fe_3O_4$	$\frac{Fe_3O_4}{3Fe} = \frac{231.55}{167.55} = 1.38$
Fe_3O_4: 231.55 g/mol	$Fe_3O_4 + 0.25O_2 \rightarrow 1.5Fe_2O_3$	$\frac{1.5 * Fe_2O_3}{Fe_3O_4} = \frac{239.55}{231.55} = 1.0345$

Figure 55: Possible iron oxidation reactions.

Particle Size and Combustion Mode

As discussed in section 1.2, only iron is expected to burn in the heterogeneous combustion mode that produces solid micron sized oxides as a porous shell around the original particles at stoichiometric conditions with air as the oxidizing medium. The results of the particle size analysis, shown in Figure 38 and Figure 39, demonstrate that the iron is indeed burning in that mode. As can be seen in the graphs, the unburnt powder has a tighter distribution, but also a smaller mean particle size than the burnt powder. Both the mean particle size and the entire particle size distribution are shifted to the right. This is the case for both the irregular shaped sponge iron and the spherical atomized powder, meaning that the increase in size is not simply due to a shape change. The long tails of the burnt powder size distribution are likely caused by particles agglomerating to create larger particles.

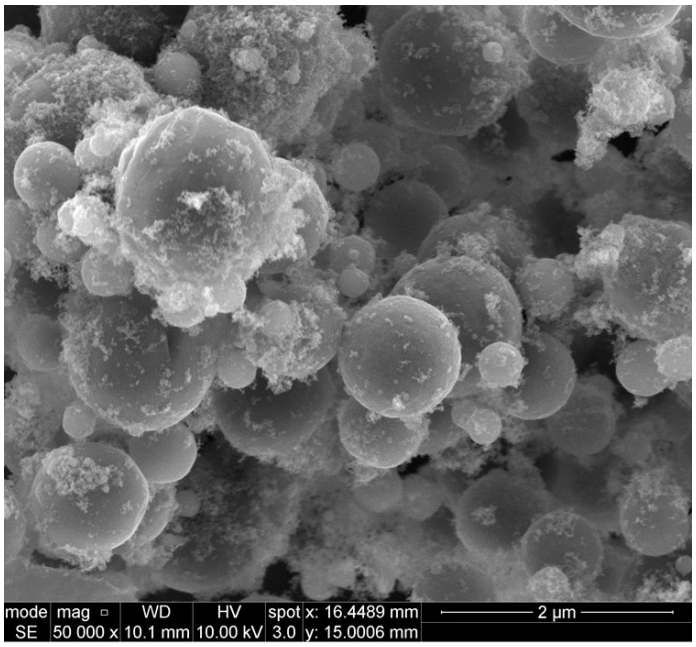

Figure 56: SEM image of nanometric oxide formed in a counter-flow iron burner. Source: Unpublished work performed in [43]

The SEM images also show that there is no presence of the formation of nanometric oxides, which is one of the goals of the turbulent burner. Nanometric oxides resemble fluff surrounding larger particles, as shown in Figure 56, which is an SEM image of burnt iron powder produced using a counter-flow iron burner as part of unpublished work in [43]. Of course since the nanometric oxides are smaller than the cutoff diameter of the cyclone collection system and the downstream HEPA filter, their presence cannot be completely ruled out. However, as seen in the previous figure, they

are generally found coating larger particles and there is no evidence of this in the burner. The fact that the burner produces larger particles is extremely important for the recycling aspect of the metal fuel concept, since it makes it easier and less costly to collect the burnt particles.

Further evidence that the flame is burning heterogeneously in the diffusion limited regime comes from the temperature measurements of the particles in the flame. As mentioned before, the measured temperature of the burning particles is 2080 K, which is close to the theoretical adiabatic flame temperature of 2250 K. This indicates that the particles have undergone ignition and are burning at their flame temperature, as the gas temperature is expected to be lower because of the additional air.

Particle Burning Temperature

The measurements taken with the spectrometer provide the temperature of the burning iron particles and not the overall temperature of the flame (gas temperature). Since the spectrometer measures the light intensity with wavelength, it only captures information from the light emitting particles and not the gas. In addition, the equations used to determine the temperature are only valid for solid body emitters. It is very difficult to measure the gas temperature separately from the particle temperature in the flame zone. Intrusive methods such as the use of thermocouples can affect the stability of the flame and also can get coated in burning particles, which will not give meaningful results. Non-intrusive measurement techniques of gas temperature for solid fuel flames have not been found in literature. However, the particle burning temperature is useful information for future design of burners and heat extraction. As shown in Figure 35, the average temperature of the particles in the flame is 2080 K. The experimental uncertainty with the polychromatic fitting method is estimated to be 2% [69]. The temperature of the gas in the iron flame is expected to be lower than that of the particles because of the excess air added to the flame. At stoichiometry, the gas temperature can at most be the same temperature as the particles. This particle temperature is similar to the adiabatic flame temperature of natural gas which is 2233 K and that of pulverized coal which is 1973 K. In terms of future design and retrofitting, this means that current burner systems for power generation are well suited to the temperatures of iron flames. No new or more expensive materials need to be incorporated into designs to withstand the temperature of iron flames. Secondly, the particle temperature plays an important role in the radiative heat transfer of the flame. Since the burning particles are solid bodies, they emit radiation according to Planck's law, which scales to the fourth power of temperature. Therefore the hotter they are

the more radiative heat they will emit. Accurate knowledge of the particle temperature allows for designs that maximize the heat extraction through radiation. This can be followed by convective heat transfer downstream of the flame from the hot gas, similar to coal combustors which begin heating water/steam downstream of the flame and then the main heating (and superheating) of the steam occurs in the combustion chamber in the vicinity of the flame through radiation.

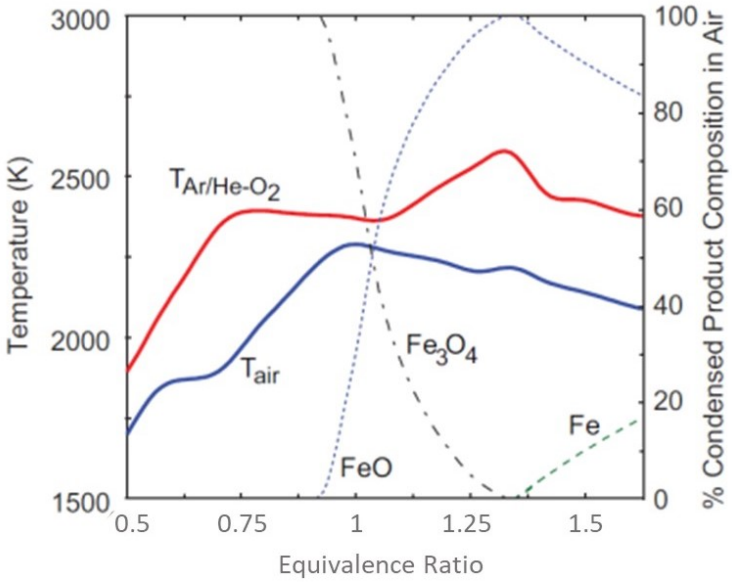

Figure 57: Adiabatic flame temperature of iron flame as a function of equivalence ratio. Source: Adapted from [63]

As discussed in section 2.3, a stratified burner design was used in part to minimize NO_x production. The thermal NO_x pathway is the only major source of NO_x production in iron flames, and this only occurs at temperatures above 1800 K. By keeping the total equivalence ratio low, but having a fuel rich inner zone, it is possible to have a stable flame and a lower flame temperature than that of the burning particles. The blue curve of Figure 57 shows the theoretical adiabatic flame temperature of an iron flame in air as a function of equivalence ratio. The adiabatic flame temperature is the temperature of the products of a combustion reaction if no heat is lost to the surroundings. From this graph, the predicted flame temperature of the current burner is approximately 1800 K. This means that the burner should not produce appreciable amounts of NO_x. Indeed preliminary testing using a CLD 600 NO_x analyzer from California Analytical Instruments did not measure any significant amounts of NO_x either near the flame or downstream. Further analysis of NO_x formation using more accurate non-intrusive measurement techniques was beyond the scope of the project and is left as future work to be carried out on the burner.

Heat Extraction

The heat extraction experiment demonstrates the feasibility of turbulent flames for power generation and industrial heat. As shown in Figure 36, on average 3 kW ±0.5 kW of heat was extracted from the flame. This is a significant amount considering the total thermal power of the flame is roughly 10 kW and that the heat exchanger was only placed on a 30 cm section of combustion chamber. Moreover, it shows the importance of radiative heat transfer in iron flames. Radiative heat transfer is expected to be the dominant form of heat transfer since the burning particles are solids, similar to pulverised coal combustion. This is bolstered by the results of the simple heat transfer model shown in Figure 37, which predicts roughly 4 kW of heat loss from the flame. The difference between the experimental results and the model could be due to several factors. First of all there are many assumptions that can lead to higher heat loss in the model such as the constant wall temperature of 300 K, assuming an optically thin flame, the emissivity of iron/iron oxide can vary greatly especially solid or molten state and the calculated initial air temperature. Secondly, the experimental setup is far from ideal and does not capture the maximum amount of heat possible. Looking at the last data point of Figure 36 with the highest water flow rate, meaning the lowest wall temperature, the measured heat capture was 4 kW which is much closer to the model. However, this data point also has the largest experimental error associated with it. The error in the measurements comes from the accuracy limits of the water flow meter and the thermocouple reading device. In addition, the burning time of particles of this size (mean diameter of roughly 20 μm), is estimated to be around 10 ms using the d^2 law [31]. Using the bulk particle velocity the distance covered by a burning particle is on the order of 3 cm, meaning the particles would burn out well before the end of the combustion chamber. However, this is clearly not the case as bright particles are seen at the exit of the combustion chamber. Based on color the particles are at least 900 °C. The model predicts an outlet particle temperature of roughly 500 °C, overestimating the heat extracted from the particles over this distance. Therefore either the burning time is much longer expected, or some particles are only ignited downstream of the flame anchoring zone, or lastly that the particles are being continually reheated by the surrounding hot gas. The latter is what is predicted by the heat transfer model since the heat lost to the pipe walls by convection is much smaller than that lost to the particles. On the other hand, the heat lost to pipe walls by radiation from the particles accounts for the bulk of the heat loss. Thus model predicts that the dominant mode of heat transfer to the walls is radiation from the particles, and then subsequent

he ating of the particles through convection by the hot gas since the particles are very small.

Many improvements can be made to the current system to improve the heat capture abilities such as using conductive heat paste between the copper coils and the steel combustion chamber. Another simple change is flowing the water from the top of the combustion chamber towards the bottom so that the hottest part, the flame zone, is heating the water at the end thereby having the greatest temperature differential throughout the process. Lastly, the length of the pipe can also be increased to provide a larger surface area for heat transfer, up to the limit of the stable length of the flame. Further testing to isolate the effect of radiative heat transfer from convective heat transfer should be carried out, such as using a reflective material like polished stainless steel on the interior of the combustion chamber. This would minimize the heat lost through radiation to the pipe walls, as it would reflect the radiation back towards the particles and eventually out of the combustion chamber.

These results provide a first step towards the design of effective heat extraction systems that are adapted to the two phase nature of the flow. Capturing heat from the flame without interacting with the hot particles is extremely important, since direct contact with the particles will significantly reduce the efficiency and working life of any device. These results can also help the design of the combustion chambers themselves, since controlling the temperature in this region is important.

6 Conclusion

A novel turbulent iron burner was designed, built and tested that successfully achieved its primary goal of creating the first ever self-sustained turbulent pure iron flame. The burner operated at the lab scale with a thermal power of roughly 10 kW and the flame was stabilized for over 20 minutes, being limited mainly by the size of the dispersion system. The design was based on knowledge gained from previous work on metal combustion as well as from scientific work done for the coal combustion industry, and implemented new methods to metal combustion. The ability to stabilize pure iron flames in air for long durations is the first step in demonstrating the feasibility of iron as a new carbon free energy carrier.

The stability of the iron flame and the effectiveness of the cyclonic collection system allowed many measurements to be taken. Heat extraction experiments demonstrated the potential of iron flames to create power through boilers or heat engines, or supply heat for industrial processes such as hot air generators. The combustion efficiency was determined to be a minimum of 96% using information from thermogravimetric analysis and X-ray diffraction. Magnetite is the main product formed from the combustion process, with small amounts of wüstite and hematite present as well. The presence of wüstite in the products implies rapid cooling post combustion since it is unstable at temperatures below 570 °C. Evidence from the particle burning temperature and the particle size distribution before and after combustion indicate that the iron particles burn in a diffusion limited heterogeneous combustion mode that produces micron size oxide products as theorized in previous works. Lastly, preliminary testing for NO_x did not measure appreciable levels and a theoretical flame temperature of 1800 K, indicates the concept of the stratified burner can play an important role in mitigating the formation of NO_x while still achieving a stable flame.

References

[1] Shell. "Enter World Energy Model a View To 2100". In: *Shell International BV* (2019), p. 17. URL: https://www.shell.com/energy-and-innovation/the-energy-future/scenarios/shell-scenarios-energy-models/world-energy-model.html.

[2] National Energy Board. *Canada's energy future 2018: An Energy Supply and Demand Projections to 2040*. Tech. rep. 2018, pp. 1–112. URL: https://www.cer-rec.gc.ca/en/data-analysis/canada-energy-future/2018/index.html.

[3] James Murray and David King. "Peak Oil has passed". In: *Nature* 481 (2012), pp. 433–435.

[4] G. Maggio and G. Cacciola. "When will oil, natural gas, and coal peak?" In: *Fuel* 98 (2012), pp. 111–123.

[5] Carlos de Castro, Luis Javier Miguel, and Margarita Mediavilla. "The role of non conventional oil in the attenuation of peak oil". In: *Energy Policy* 37.5 (2009), pp. 1825–1833.

[6] James Hansen et al. "Climate sensitivity, sea level and atmospheric carbon dioxide". In: *Philisophical Transactions of the Royal Society A* 371 (2013).

[7] Taylor M. Hoegh-Guldberg O., Jacob D. *Chapter 3: Impacts of 1.5°C global warming on natural and human systems. In: Global Warming of 1.5 °C. An IPCC special report on the impacts of global warming of 1.5 °C above preindustrial levels and related global greenhouse gas emission pathways [...]* Tech. rep. 2018, pp. 175–311.

[8] J. Rogelj et al. "Mitigation Pathways Compatible with 1.5°C in the Context of Sustainable Development." In: *IPCC special report Global Warming of 1.5 ^{o}C* (2018), 82pp. URL: https://www.ipcc.ch/site/assets/uploads/sites/2/2019/02/SR15_Chapter2_Low_Res.pdf.

[9] John A. Turner. "A realizable renewable energy future". In: *Science* 285.5428 (1999), pp. 687–689.

[10] Mark A. Delucchi and Jacobson Mark A. "A path to sustainable energy by 2030". In: *Scientific American* 301.5 (2009), pp. 58–65.

[11] Vasilis Fthenakis, James E. Mason, and Ken Zweibel. "The technical, geographical, and economic feasibility for solar energy to supply the energy needs of the US". In: *Energy Policy* 37.2 (2009), pp. 387–399.

[12] J M Bergthorson et al. "Direct combustion of recyclable metal fuels for zero-carbon heat and power". In: *Applied Energy* 160 (2015), pp. 368–382.

[13] Government of Canada. *Iron Ore Facts*. 2021. URL: https://www.nrcan.gc.ca/our-natural-resources/minerals-mining/minerals-metals-facts/iron-ore-facts/20517#shr-pg0 (visited on 06/08/2020).

[14] R. K. Eckhoff. "Prevention and mitigation of dust explosions in the process industries: A survey of recent research and development". In: *Journal of Loss Prevention in the Process Industries* 9.1 SPEC. ISS. (1996), pp. 3–20.

[15] Rolf K Eckhoff. *Dust Explosions in the Process Industries (3rd Edition)*. Elsevier, 2003.

[16] W. T. OLSON and P. C. SETZE. "Some combustion problems of high-energy for aircraft". In: *Symposium (International) on Combustion* 7.1 (1958), pp. 883–893.

[17] Kenneth K Kuo. *Fundamentals of solid solid propellant combustion*. 1984.

[18] David Albertovich. Frank-Kamenetskii. *Diffusion and Heat Exchange in Chemical Kinetics*. English. Princeton, N.J., 2016.

[19] Howard D Ross. *Microgravity combustion : fire in free fall*. English. San Diego: Academic Press, 2001, p. 575.

[20] E N Rumanov and B I Khaikin. *Critical autoignition conditions for a system of particles*. Tech. rep. i. 1969, pp. 129–136.

[21] Michael Soo et al. "Combustion of particles, agglomerates, and suspensions – A basic thermophysical analysis". In: *Combustion and Flame* 192 (2018), pp. 384–400.

[22] Irvin Glassman, Richard Yetter, and Nick Glumac. *Combustion*. English. Fifth edit. Amsterdam: Academic Press, 2014, p. 773.

[23] Prabir Basu, Cen Kefa, and Louis Jestin. *Boilers and Burners*. Springer, 2000, p. 563.

[24] Irvin Glassman. *Metal Combustion Processes*. Tech. rep. 1959.

[25] E. L. Dreizin. "Phase changes in metal combustion". In: *Progress in Energy and Combustion Science* 26.1 (2000), pp. 57–78.

[26] R. Friedman and A. Maček. "Combustion studies of single aluminum particles". In: *Symposium (International) on Combustion*. Vol. 9. 1. Elsevier, 1963, pp. 703–712.

[27] Edward L. Dreizin. "On the mechanism of asymmetric aluminum particle combustion". In: *Combustion and Flame* 117.4 (1999), pp. 841–850.

[28] R Friedman and A Macek. "Ignition and Combustion of Aluminium Particles in Hot Ambient Gases". In: *Combustion and Flame* 6 (1962), pp. 9–19.

[29] Yuriy L Shoshin and Igor S Altman. "Integral Radiation Energy Loss During Single Mg Particle Combustion". In: *Combustion Science and Technology* 174.8 (2002), pp. 209–219.

[30] Kerri Lee Chintersingh, Mirko Schoenitz, and Edward L. Dreizin. "Combustion of boron and boron–iron composite particles in different oxidizers". In: *Combustion and Flame* 192 (2018), pp. 44–58.

[31] Alex Wright, Samuel Goroshin, and Andrew Higgins. "Combustion Time and Ignition Temperature of Iron Particles in Different Oxidizing Environments". In: *25th ICDERS* (2015), pp. 1–6.

[32] Daniel Spreitzer and Johannes Schenk. "Reduction of Iron Oxides with Hydrogen—A Review". In: *Steel Research International* 90.10 (2019).

[33] E. L. Dreizin, A. V. Suslov, and M. A. Trunov. "General Trends in Metal Particles Heterogeneous Combustion". In: *Combustion Science and Technology* 90.1-4 (1993), pp. 79–99.

[34] Theodore A. Steinberg et al. "The combustion of iron in high-pressure oxygen". In: *Combustion and Flame* 89.2 (1992), pp. 221–228.

[35] Maryse Muller, Hazem El-Rabii, and Rémy Fabbro. "Liquid phase combustion of iron in an oxygen atmosphere". In: *Journal of Materials Science* 50.9 (2015), pp. 3337–3350.

[36] S. Goroshin, I. Fomenko, and J. H S Lee. "Burning velocities in fuel-rich aluminum dust clouds". In: *Symposium (International) on Combustion* 26.2 (1996), pp. 1961–1967.

[37] S. Goroshin, M. Bidabadi, and J. H.S. Lee. "Quenching distance of laminar flame in aluminum dust clouds". In: *Combustion and Flame* 105.1-2 (1996), pp. 147–160.

[38] François David Tang et al. "Flame propagation and quenching in iron dust clouds". In: *Proceedings of the Combustion Institute* 32 II (2009), pp. 1905–1912.

[39] Philippe Julien et al. "Effect of scale on freely propagating flames in aluminum dust clouds". In: *Journal of Loss Prevention in the Process Industries* 36 (2015), pp. 230–236.

[40] Jin hua Sun, Ritsu Dobashi, and Toshisuke Hirano. "Temperature profile across the combustion zone propagating through an iron particle cloud". In: *Journal of Loss Prevention in the Process Industries* 14.6 (2001), pp. 463–467.

[41] Philippe Julien et al. "Freely-propagating flames in aluminum dust clouds". In: *Combustion and Flame* 162 (2015), pp. 4241–4253.

[42] Philippe Julien et al. "Flame speed measurements in aluminum suspensions using a counterflow burner". In: *Proceedings of the Combustion Institute* 36.2 (2017), pp. 2291–2298.

[43] Michelle McRae et al. "Stabilized, flat iron flames on a hot counterflow burner". In: *Proceedings of the Combustion Institute* 37.3 (2019), pp. 3185–3191.

[44] H. Spliethoff. *Power Generation from Solid Fuels*. Springer-Verglag, 2010, p. 672.

[45] A. Stambuleanu. *Combustion Processes in Industry*. Kent, England: ABACUS Press, 1976, p. 567.

[46] John B Kitto. "Developments in Pulverized Coal-Fired Boiler Technology". In: *Missouri Valley Electric Association Engineering Conference* (1996).

[47] Hao Zhou et al. "Influence of the gas particle flow characteristics of a low-NOx swirl burner on the formation of high temperature corrosion". In: *FUEL* 134 (2014), pp. 595–602.

[48] Chaoyang Zhou et al. "Mechanism analysis on the pulverized coal combustion fl ame stability and NOx emission in a swirl burner with deep air staging". In: *Journal of the Energy Institute* January (2018), pp. 1–13.

[49] J.M. Beér and N A Chigier. *Combustion Aerodynamics*. Applied Science Publishers Ltd, 1972, p. 264.

[50] N Syred and J M Beer. "Combustion in Swirling Flows : A Review". In: *Combustion and Flame* 23 (1974), pp. 143–201.

[51] B Repic et al. "Experimental determination of the swirl burner laboratory models hydraulic resistance". In: *Procedia Engineering* 42.August (2012), pp. 672–682.

[52] Muhammad Roslan Rahim, Mohammad Nazri, and Mohd Jaafar. "Effect of Flame Angle Using Various Swirler Angle in Combustion Performance". In: *Jurnal Teknologi* (2015).

[53] M N Mohd Jaafar et al. "Combustor aerodynamic using radial swirler". In: *International Journal of Physical Sciences* 6.13 (2011), pp. 3091–3098.

[54] N G Orfanoudakis et al. "Design , evaluation measurements and modelling of a small swirl stabilised laboratory burner". In: *IFRF Combustion Journal* (2005).

[55] R. Muthu Dinesh Kumar and R. Anand. "Production of biofuel from biomass downdraft gasification and its applications". In: *Advanced Biofuels: Applications, Technologies and Environmental Sustainability*. 2019.

[56] C. A. Martin. "Aspects of the design of swirlers as used in fuel injectors for gas turbine combustors." In: *American Society of Mechanical Engineers (Paper)*. 1987.

[57] R K Cheng and D. Littlejohn. *Natural Draft Low Swirl Burner*. 2014.

[58] ML Mathur and NRL Maccallum. "Swirling Air Jets Issuing from Vane Swirlers". In: *Journal Of The Institute Of Fuel* 40.316 (1967), pp. 214–225.

[59] C. K. Law. *Combustion Physics*. Cambridge University Press, 2006, p. 722.

[60] M. W. Jr. Chase. *NIST-JANAF Themochemical Tables, Fourth Edition*. American Institute of Physics, 1998.

[61] W. Leuckel. *Swirl intensities, swirl types and energy losses of different generating devices*. Tech. rep. Ijmuiden, Holland: International Flame Research Foundation, 1968.

[62] J. Chedaille, W. Leuckel, and A. K. Chesters. "No Title". In: *Journal Of The Institute Of Fuel* 39.311 (1966), pp. 506–21.

[63] Franois David Tang, Samuel Goroshin, and Andrew J. Higgins. "Modes of particle combustion in iron dust flames". In: *Proceedings of the Combustion Institute* 33.2 (2011), pp. 1975–1982.

[64] ECKART TLS GmbH. *The process*. URL: `https://www.tls-technik.de/en/the-process.html` (visited on 06/10/2021).

[65] David P Incropera, Frank P. DeWitt. *Fundamentals of Heat and Mass Transfer*. 5th. Hoboken: Wiley, 2002, p. 1008.

[66] David J Young. *High Temperature Oxidation and Corrosion of Materials*. Second. Elsevier, 2016, p. 720.

[67] Esmail R. Monazam, Ronald W. Breault, and Ranjani Siriwardane. "Kinetics of magnetite (Fe3O4) oxidation to hematite (Fe2O3) in air for chemical looping combustion". In: *Industrial and Engineering Chemistry Research* (2014).

[68] J. Païdassi. "The kinetics of the air oxidation of iron in the range 700-1250°C". In: *Acta Metallurgica* 6.3 (1958), pp. 184–194.

[69] Samuel Goroshin et al. "Emission spectroscopy of flame fronts in aluminum suspensions". In: *Proceedings of the Combustion Institute* 31 II.2007 (2007), pp. 2011–2019.